Thermal boundary resistance in YBCO THz microbolometers at room temperature

Thesis for Erasmus Mundus Master of Science in Nanoscience and Nanotechnology

PIERRE HERMAN

Department of Microtechnology and Nanoscience
Terahertz and Millimeter Wave Laboratory
Chalmers University of Technology
Gothenburg, Sweden 2014

Thesis for the degree of

Erasmus Mundus Master of Science in Nanoscience and Nanotechnology

Thermal boundary resistance in YBCO THz microbolometers at room temperature

PIERRE HERMAN

Promoter & Supervisor: Prof. Sergey Cherednichenko, Chalmers
Co-promoter : Prof. Bob Peurs, K.U. Leuven

Terahertz and Millimeter Wave Laboratory
Department of Microtechnology and Nanoscience
CHALMERS UNIVERSITY OF TECHNOLOGY
Gothenburg, Sweden 2014

Thermal boundary resistance in YBCO THz microbolometers at room temperature
PIERRE HERMAN

Department of Microtechnology and Nanoscience
Chalmers University of Technology
SE- 412 96 Gothenburg, Sweden
Telephone: +46 (0)31-772 10 00
Website: www.chalmers.se

Chalmers Reproservice
Gothenburg, Sweden 2014

Abstract

Terahertz waves are utilized for a wide range of applications, from security, medical imaging to gas spectroscopy, etc. Previous investigations in the Teraherzt and Millimeter wave group at Chalmers, has shown that antenna-integrated $YBa_2Cu_3O_7$ (YBCO) bolometer could serve as a potential detector for this range of the electromagnetic spectrum.

The detector is composed of a 70 nm thick YBCO film with micron sized dimension and is deposited on a crystalline Al_2O_3 (sapphire) substrate. Phonons, the quasi-particles associated with the lattice vibrations, transport the heat from the film to the substrate, but are scattered in this process. This scattering is macroscopically represented by the thermal resistance. The thermal resistance is responsible for the response and speed of these bolometers.Two parameters are varied that we believe could affect this thermal resistance. The first parameter is the thickness of the CeO_2 buffer layer. This layer is situated between a YBCO layer and a sapphire substrate. Its purpose is to provide a good lattice match and chemical isolation of the YBCO layer with respect to the substrate. The range studied is 10 - 50 nm. The second parameter is the deposition temperature during the deposition of the film using pulsed laser deposition, this parameter is known to affect the YBCO film quality, however no study has investigated its influence on the thermal properties of the detector. The range studied is $780°C - 855°C$.

The thermal resistance is experimentally studied by fabricating the bolometers with above mentioned parameters and measuring them using DC (IV, Resistance-Power) and RF techniques (voltage response versus modulation frequency). Results are analyzed and compared to reported measurements as well as with the Two Temperature model.

Considerable variability is present for all devices, even when fabrication parameters are kept constant. The performance was not improved by either the buffer thickness or the temperature deposition in the studied range. The effective thermal resistance extracted from the DC measurements is found to be situated between $0.1.10^{-3}cm^2K/W - 1.0.10^{-3}cm^2K/W$ (excluding outliers). These values are not in accordance with the RF-measurements. The study suggests that additional knowledge on the phenomena involved in the heat transport is required.

Acknowledgements

First of all I would like to thank my supervisor and promotor Prof. Sergey Cherednichenko for giving me the opportunity to work in this interesting field to which I was completely unfamiliar with. I thank him also for always being open for discussions and helping me not to get lost in the lab between the cables and those boxes they call microwave sources. I am grateful for his immense patience, especially during the last months. I am also very thankful to Stella Bevilacqua for helping me all along the way as well, especially regarding fabrication. Also Evgenii Novoselov for helping me in the cleanroom when everything was new. I would like to thank John Hallonen for the helping me with the mask alligner when it was acting strangely.

Next I would like to thank my friends Professor Vessen and Hosein, for helping me correcting some parts of the work, Prof. Dag Winkler for the 'coffees after lunch', Mohammed for helping me create some of the figures, and Henrik for fixing all my computer problems.

I would also like to thank Professor Bob Peurs for taking up the role of co-promoter. I am thankful to Guido Groeseneken, for allowing me to join the program last minute.

I would like to thank Jan Denef, my neighbour back in Belgium, for all his help during these years of learning. Lastly my family and grandparents, but they know.

Pierre,
Göteborg,
August 2014

Contents

1

Introduction

The Terahertz range is the last part of the electromagnetic spectrum that remains largely unexplored. It spans from 0.1 to 10 THz, in terms of frequency or equivalently from 0.03-3 mm in terms of wavelength. It is referred to the 'terahertz gap', because of the lack of sources and detectors in this frequency range. The light in this frequency range starts to find a lot of interesting applications in very distinct domains of science and technology. On one hand, because of its long wavelength compared to the visible and infrared, it is semitransparent for many materials, for instance to clothes, plastics, and some packaging materials, and at the same time triggers these materials to leave a spectral 'fingerprint' [1]. On the other hand the wavelengths are still short enough that diffraction can be coped with and hence still allow for imaging. This combination enables security applications like detection of concealed weapons [2], industrial quality control, as well as biomedical imaging where the non-ionizing low energy content of the rays ,unlike X-rays, are not damaging the patient. For the same reasons we are able to discover hidden paintings without harming the art work [3]. Space applications benefit as well since the universe is bathed in terahertz energy, half of the total luminosity and 98% of all photons fall into this range, remaining *one of the last unexplored frontiers of space astronomy* [4]. Gases in the earths atmosphere have spectral lines in the THz as well, studying these can reveal information on climate change [5]. Next generation telecommunication systems will require even higher bandwidths to satisfy the demand, this will be inherently achieved by moving from the microwave to the THz range [6]. Apart from the already mentioned technological hurdle, a major problem is that most of the radiation in the THz range is absorbed by water molecules contained in the air, however applications like WIFI for short-range indoor communication are still possible [7] [8], for long distance communications there are some specific frequency windows that can still be used that are more free of absorption [9], also the water content decreases with altitude, so that aircraft to satellite or satellite to satellite communication is feasible. The same problem restricts 'radio'telescopes to high altitudes or space.

To enlarge and improve the scope of applications of the THz range, sources and detectors must be improved and made more available. Ideally we would like to have detectors which are operational over the whole THz range, are very sensitive, are very fast, and operate at room temperature. Uncooled technology has the advantage of being much more compact, lighter, and cheaper than their cryogenic counterparts.

This thesis focuses on YBCO-room temperature micro-bolometers, one of the possible detectors that could serve to detect THz radiation. The bolometer is a thermal detector and consists of a thin film absorber that is in direct contact with a substrate. Incoming radiation heats the film. The phonons, the quasi-particles associated with the lattice vibrations, transport the heat from the film to the substrate and are scattered at the interface between the film and substrate. This scattering is macroscopically represented by the thermal boundary resistance and is responsible for the response and speed of the detector. Tuning of the thermal boundary resistance to adjust the performance of the detector has not yet been investigated.

Two parameters are investigated in this work that should have a major influence on this thermal boundary resistance. YBCO material has a very complex crystallographic structure and is grown using Pulsed Laser Deposition; one important parameter that is known to determine the quality of the film and the interface of the film with the material on which it is grown, is the temperature at which the material is deposited. Secondly, since the specific crystalline structure of YBCO does not match the one of the substrate used, a buffer layer is deposited on the substrate prior to the YBCO. The thickness of this layer is suspected to affect the crystalline growth of the film.

This thesis investigates how two parameters, the buffer layer thickness and temperature deposition, affects the operation of room-temperature planar YBCO micro bolometers. There is a strong focus on experimental work involving both fabrication and characterization of the bolometers. It is organized as follows: Chapter 1 (current chapter), gives the motivation of developing terahertz detectors and points out what this work investigates specifically. Chapter 2 gives a theoretical background on how a bolometer works, both as direct and heterodyne detector, it introduces the two temperature model to explain in more detail the frequency behavior of the bolometer, the same chapter also describes a technique to couple THz radiation into the device and discusses the relevant material parameters. Next follows a chapter dedicated to the fabrication process (Chapter 3). Chapter 4 explains the measurement setups used to extract the relevant device characteristics, specifically the thermal boundary resistance is experimentally investigated both by DC (IV, Resistance-Power) and RF techniques (IF-power vs IF-frequency). Chapter 5 shows, discusses and summarizes the data obtained. Finally, chapter 6 presents some concluding remarks and possible future work.

2

Theoretical background

We will first introduce the working principle of the bolometer. In a following section we show the actual implementation and point out what parameters to tune in order to obtain fast and responsive detectors.In order to extract information on the speed, we apply signals with varying frequencies. Limitation in the measurement setup forces us to employ the detector both in the heterodyne and direct, hence a section is dedicated to the principle of operation of both these techniques. The radiation is coupled in the bolometer using an antenna and lens, and this is discussed in a next section. After measuring the devices, we found out that the bolometer responds in a more complex way to frequencies than what the first introduced model predicts, a more elaborated model found in literature, commonly referred to as the two temperature model, is therefore introduced in a separate section. Next, a section on the choice of materials is provided. Lastly a brief comparison with other detectors is made.

2.1 Working Principle of the bolometer

The bolometer is a thermal detector for electromagnetic radiation. Its name was given by its inventor astronomer Samuel Langley in 1881, $\beta o\lambda\eta$ (beam, ray) $\mu\varepsilon\tau\rho o\nu$ (meter, measure), it enabled him to study solar irradiance far into its infrared region and to measure the intensity of solar radiation at various wavelengths[10] [11].

The bolometer consists of an absorber of radiation, a thermometer and a thermal link to a reservoir maintained at a fixed temperature. There exists two categories of bolometers, *monolithic* bolometers, the case in this work, where the absorber and the thermometer are one single entity and *composite* bolometers where the two are distinct elements (as on the figure 2.1).

We suppose an initial state in which the bolometer is at equilibrium with its environment so the temperature T_B is the same as that of the reservoir. This reservoir is supposed to be ideal, i.e. its temperature remains fixed at T_s. At a certain time a power

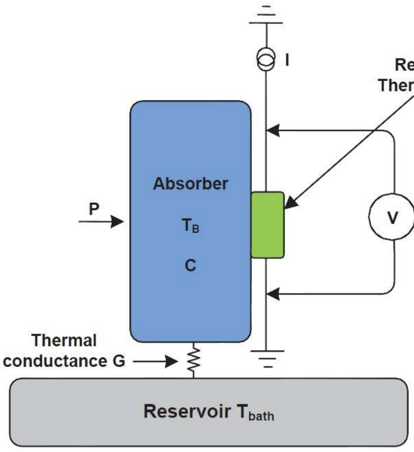

Figure 2.1: A bolometer consists of several elements. An absorber material that converts the power into heat, giving rise a relative increase in its temperature. This absorber is characterized by a heat capacity C and a thermal conduction G to a constant temperature reservoir. A thermometer the actual sensor, measures the temperature change in the absorber. It does this by passing a current I through a material in contact with the absorber affecting its resistance upon heating, and observing the voltage drop across it. Picture taken from [12].

of constant amplitude is applied. This power P is converted into heat and leads to a temperature increase in the bolometer with respect to the reservoir at fixed temperature T_s. How efficiently the heat is being removed is characterized by the thermal conductance G. If power is kept constant, the absorber will reach a new equilibrium temperature T_0. Mathematically the temperature T_B in the bolometer is described by a first order differential equation:

$$C\frac{dT}{dt} = P - G(T - T_s).$$

, where C is the thermal capacity of the absorber. Assuming that power is applied to the bolometer at t_0, and $T(t < t_0) = T_s$, a solution is:

$$T_B(t) = (T_s - (\frac{P}{G} + T_s))e^{-\frac{G}{C}t} + (\frac{P}{G} + T_s). \tag{2.1}$$

Hence:

$$T_0 = T_s + \frac{P}{G}. \tag{2.2}$$

Similarly, once this equilibrium at T_0 is reached and the incoming power is turned off, by solving this time $C\frac{dT}{dt} = G(T - T_s)$, we obtain

$$T_B(t) = T_s + (T_0 - T_s)e^{-\frac{G}{C}t} \tag{2.3}$$

Summarized, the equilibrium temperature of the heated bolometer T_0 is determined by G and the dynamics are characterized by an exponential decay (or growth) factor:

$$\tau = C/G \tag{2.4}$$

This analysis of the temperature is necessary because it is the temperature which will cause a change of resistivity in the material. The change in resistance will induce a change in voltage this is what will be measured. A lower value of G will cause a higher temperature change (as heat is less effectively removed) and hence the more sensitive the sensor is since this leads to a higher voltage readout for a given amount of incoming power.

The time constant is an important parameter to consider as well, if the bolometer needs to follow signals that vary over time. The bolometer needs a time around $\tau = C/G$, to reach (close enough to) a new equilibrium stage. Hence it is intuitive to say that for the bolometer to be able to follow[1] the variations in incoming power, these variations must be slower than $\tau = C/G$. In other words the angular frequency of the signal should be lower then $(\frac{C}{G})^{-1}$.

---

[1] by 'following' is understood that the bolometer has the temperature as in the situation where the instantaneous incoming power would already have been present for an infinite amount of time.

2.2 Operation modes

To detect a signal, a bolometer can operate in two different modes as a direct detector or as a mixer. The choice of technique to detect THz signals depends on the requirements on responsivity, noise, frequency, bandwidth and phase selectivity [13], a proper justification falls outside the scope of this thesis. Both techniques are explained however since a constraint in the measurement setup forces us to use both (see sections 4.2.2 4.2.1). In this thesis the techniques are used to obtain information on how the intrinsic voltage response of the detector behaves as a function of frequency.

2.2.1 Operation as a direct detector

The most simple way is to detect the radiation directly. The detector absorbs the radiated signal and its response follows the signal amplitude. The readout of the electric signal occurs in a next stage, giving a DC voltage proportional to the radiation amplitude. In order to determine the spectral distribution of the detected signal within the frequency band of the detector, in direct detection, it is necessary to include a tunable filter in the signal path. In the measurement setup this is not required since the signal applied consists of a single and known frequency $P_0(t)e^{j\omega_c t}$. Since this single frequency, ω_c lies in the THz range, the bolometer detects the amplitude of the signal but is not able to follow the dynamics of this signal (1 THz= 1 ps), hence the power gives a constant offset according to equation 2.2 , i.e. the same response as a DC signal having power P_0. The bolometer can however detect variations in the amplitude P_0 if they are slower than the time constant $\tau = C/G$ (typically for the detectors used here, below 100 MHz).

To quantify the voltage response to such variations and to proof above statement, the approach in [14] is used. For incoming radiation $P(t) = P_0 + \Delta P e^{j\omega t}$, where ω is the modulation frequency, the temperature in the bolometer varies according to $T_B(t) = T_0 + \Delta T e^{j\omega t}$. For a constant current biased bolometer, contributing to joule heating, the heat balance equation together with a first order Taylor expansion on the resistance yields:

$$P_0 + \Delta P e^{j\omega t} + I^2 R(T_0) + I^2 \frac{dR}{dT} \Delta T e^{j\omega t} = G(T_0 + \Delta T e^{j\omega t} - T_s) + j\omega C \Delta T e^{j\omega t}$$

Separating the time varying and steady state parts:

$$\begin{aligned} &P_0 + I^2 R(T_0) = G(T_0 - T_s), \\ &\frac{\Delta P}{\Delta T} = G + j\omega C - I^2 \frac{dR}{dT}, \end{aligned} \tag{2.5}$$

this allows to quantify the amplitude of the voltage of the read-out at the same frequency $V = V + \Delta V e^{j\omega t}$, since $\Delta V = I \Delta R = I \frac{dR}{dT} \Delta T$. Defining the voltage responsivity as the change in voltage drop (in volts) per watt of absorbed signal power [14] , this gives the expression:

$$R_v(\omega) \equiv \frac{\Delta V}{\Delta P} = \frac{I \frac{dR}{dT}}{G - I^2(\frac{dR}{dT}) + j\omega C} = \frac{IR\alpha}{G_{eff}(1 + j\omega\tau_{eff})} [V/W] \tag{2.6}$$

, where $\tau \equiv \frac{C}{G}$, $G_{eff} \equiv G - I^2 \frac{dR}{dT}$ and $\tau_{eff} \equiv \frac{C}{G_{eff}}$, and the temperature coefficient of resistance (TCR), $\alpha = \frac{1}{R}\frac{dR}{dT}$. The current applied has an influence on the response of the bolometer, this effect is known as electrothermal feedback. Apart from semiconductors where the $dR/dT < 0$, incident radiation increases the resistance increasing -for current biased bolometers- the DC bias power dissipation. This leads to an additional increase in the temperature, so an increased response that compensates somewhat for the heat loss through the thermal conductance G. Increasing the bias current is beneficial for the responsivity and reduces the time constant. However there is a risk of thermal runaway for values of $I^2 \frac{dR}{dT}$ close to G (an empirical limit in [15] is set to the current such that $I^2 \frac{dR}{dT} < 0.3G$). In this work we are interested in the intrinsic characteristic of the detector and hence will keep the current low, such that $G_{eff} \simeq G$ and $\tau_{eff} \simeq \tau$ and high enough to be able to detect a signal above the noise:

$$R_v(\omega) \simeq \frac{IR\alpha}{G} \frac{1}{1 + j\omega\tau} \tag{2.7}$$

2.2.2 Bolometric mixing

The other mode of detection is the mixer mode. The signal of interest situated at high frequency (above the the time constant of the detector), designated as the 'RF signal'[2]. This signal is superimposed (i.e. 'mixed') with a strong signal, called Local Oscillator (LO) signal, of fixed and known frequency close to that frequency before it hits the device. The superposition leads to the appearance of a signal at the difference of frequencies of both signals $\mid \omega_{RF} - \omega_{LO} \mid$. This frequency is typically lower than the frequency constant, so the bolometer responds thermally. As a result, the current biased bolometer produces an output voltage at $\mid \omega_{RF} - \omega_{LO} \mid$ proportional to the electric field of the original RF signal. The biggest advantage with this detection scheme is that a narrow band RF signal will have all spectral information preserved after down-conversion where low noise electronics can be used to amplify it, offering high spectral resolution [13]. This property defines the bolometer in the mixer mode as a super heterodyne receiver. However the reason to use this method in this thesis is based on equipment limitation, the (more simple) direct detection does not allow high enough amplitude modulation (the source generator limits modulation to 100 kHz) to measure the characteristic time constant (above 1 MHz typically).

Derivation below is based on [13] and [16]. In this section the RF-signal is assumed to be a signal of single frequency, its electric field given by: $E_{RF}cos(\omega_{RF}t)$. The LO field is added prior to the bolometric detection. These two fields result in dissipated power over an average resistance value R_0 of the bolometer:

---

[2] for historical reason it is done this way although it does not lie into the radio frequency range but in the terahertz

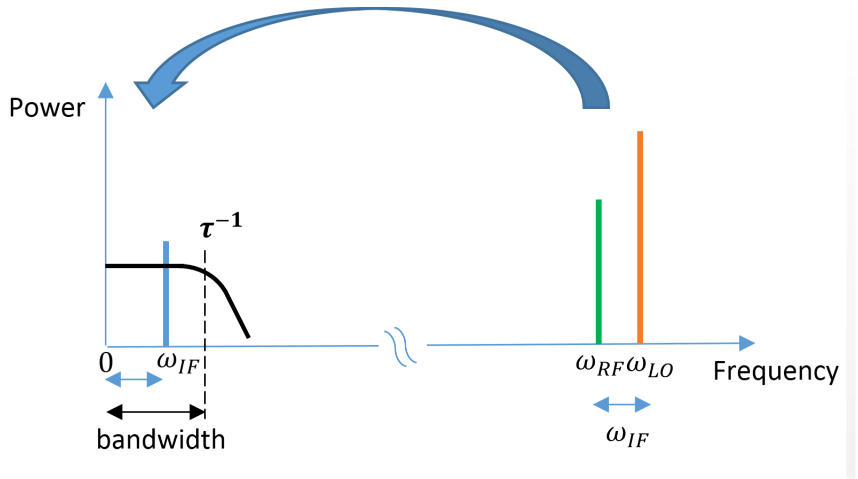

Figure 2.2: Principle of heterodyne detection. Adding an externally controlled signal, LO, allows for downconversion of the signal into the bandwidth of the bolometer. From an experimental perspective, increasing the local oscillator frequency will finally lead to a loss of downconverted signal, allowing to extract the time constant of the bolometer.

$$\begin{aligned} P &= 1/R_0 \left(E_{RF}\cos(\omega_{RF}t) + E_{LO}\cos(\omega_{LO}t)\right)^2 \\ &= 1/R_0 \left(E_{RF}^2\cos(\omega_{RF}t)^2 + 2E_{RF}\cos(\omega_{RF}t) * E_{RF}cos(\omega_{LO}t) + E_{LO}^2\cos(\omega_{LO}t)^2\right) \end{aligned} \tag{2.8}$$

Defining and using trigonometric rules we obtain :

$$\begin{aligned} P = 1/R_0 \Big(& \underline{0{,}5E_{RF}^2} + \underline{0.5E_{LO}^2} + \\ & 0.5E_{RF}^2\cos(2*\omega_{RF}t) + 0.5E_{LO}^2 cos(2*\omega_{LO}t) + E_{LO}E_{RF}\cos((\omega_{RF}+\omega_{LO})t) \\ & + \mathbf{E_{LO}E_{RF}cos((\boldsymbol{\omega}_{RF}-\boldsymbol{\omega}_{LO})t)}\Big) \end{aligned} \tag{2.9}$$

The first two terms (underlined) are constant in time, hence they will give rise to a constant temperature offset inside the bolometer. The bolometer is not able to translate in temperature fluctuations the signals whose frequencies are higher than its characteristic frequency constant τ^{-1}. In typical applications this is always the case for the frequencies $\omega_{RF} + \omega_{LO}$, $2 * \omega_{RF}$ and $2 * \omega_{LO}$. Only the power component at $\omega_{RF} - \omega_{LO}$ is usually low enough (i.e., lower than τ^{-1}) for the system to heat up and cool down, oscillating around the mean temperature imposed by the static dissipation. Summarized, the applied power will lead to static and dynamic dissipation:

$$P_{dissipated} = P_{LO} + P_{RF} + 2\sqrt{P_{LO}P_{RF}}\cos(\omega_{IF}t) \tag{2.10}$$

$$\omega_{IF} \equiv \mid \omega_{RF} - \omega_{LO} \mid$$

,where ω_{IF} is defined as the *intermediate frequency* , $\omega_{RF} - \omega_{LO}$, and $P_{RF} = 1/R(0.5(E_{RF}^2)$,$P_{LO} = 1/R(0.5(E_{LO}^2)$. The bolometric responsivity derived in previous section directly relates the power dissipation at a given frequency to the voltage fluctuations giving us:

$$V(\omega_{IF},t) = R_v(\omega_{IF})2\sqrt{P_{LO}P_{RF}}\cos(\omega_{IF}t) \tag{2.11}$$

From above formula it is clear that the bolometer has achieved the down-conversion of the RF signal (with a modified amplitude). Also notable is that increasing the local oscillator power will lead to better detectability. [3]

We can also see that the mixer bandwidth, defined as the IF-frequency where the signal starts to roll off, is determined by the characteristic time constant as well (here using a basic model):

$$V(\omega_{IF},t) = \frac{R_v(\omega_{IF}=0)}{\sqrt{1+\omega_{IF}^2\tau^2}}\sqrt{P_{LO}P_{RF}}\cos(\omega_{IF}t) \tag{2.12}$$

This voltage variations are read out on a matched load, the power dissipated in this load is defined as the intermediate frequency power P_{IF} and is hence equal to

$$P_{IF}(\omega) = \left\langle V_{IF}^2(\omega,t)\right\rangle /4R_L.$$

---

[3] There is also a limitation to how much power we can inject into the bolometer, since this power is converted into heat and might lead to thermal breakdown. Not only LO power but DC biasing as well should be carefully considered. Another remark is that typically in applications the LO power is at least a factor of 1000 larger than the RF power, allowing the bolometer to down convert not just a monochromatic signal as was assumed here but a complete band. Indeed, two different frequencies in the RF signal, lets call them RF_1 and RF_2 will unavoidably intermix and create an undesired down conversion, but with a strength according to equation (2.11) proportional to $\sqrt{P_{RF_1}P_{RF_1}}$ which is negligible compared to $\sqrt{P_{RF_1}P_{LO}}$ and $\sqrt{P_{RF_2}P_{LO}}$.

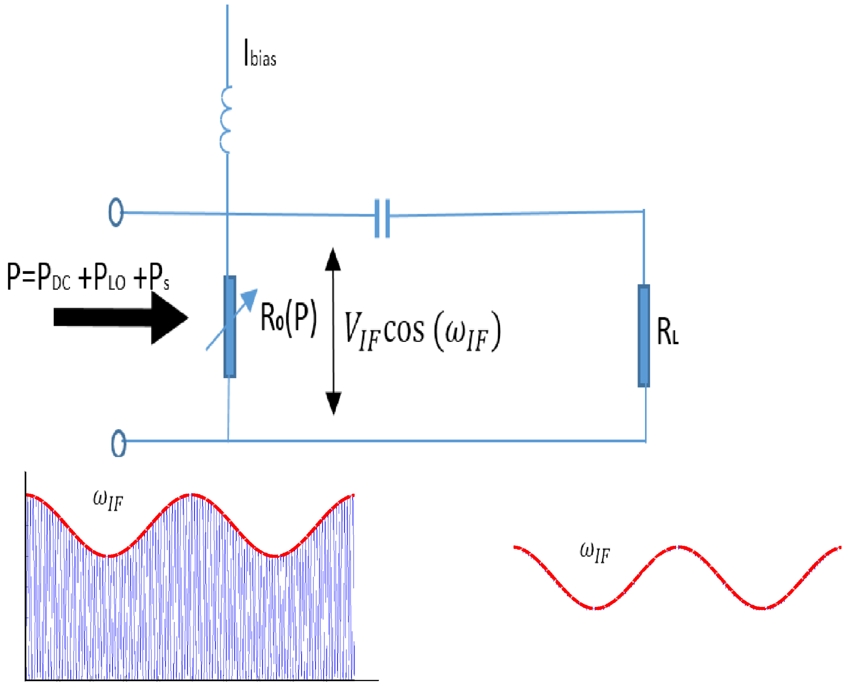

Figure 2.3: The equivalent circuit used for heterodyne detection. The graph on the left show the incident power on the bolometer, which a combination of the LO and the signal of interest, where the envelope frequency is given by the difference of those two frequencies. The bolometer extracts the envelope (graph on the right) by the simple fact that it is thermally fast enough to detect the the envelope but too slow to respond directly to either LO or RF frequencies. Note that the DC current used to bias the device is separated from the IF circuit readout by using an inductance and a capacitance (with appropriate values).

2.3 The actual bolometer

Until now we made abstraction from the actual device. The bolometer consists of a micron sized YBCO strip that is situated on top of the substrate. There are many pads through which heat from the film is evacuated, but the principal heat removal occurs through the substrate. [4] For these micro-bolometers, where the bolometer is in contact with the substrate through an area $A = LW$, G is given by

$$G \simeq G_{substrate} = \frac{A}{R_{bd}} \tag{2.13}$$

,where the factor R_{bd} is defined as the thermal boundary resistance. C is given by:

---

[4] Heat diffusion into the antenna contact pads is found to be negligible contribution to the thermal conductance, for a $1\mu m * 1\mu m$, $G = \kappa_p * d/\pi^2 = 0.07\mu W/K$ [17], more than a factor 10 lower than the lowest measured thermal conductance on the YBCO devices.

$$C = cdA \tag{2.14}$$

,where d is the thickness and c the specific heat capacity of the absorber material. Hence the time constant is given by:

$$\tau = C/G = cdR_{bd} \tag{2.15}$$

To achieve maximal responsivity, it is clear that the current should be increased as much as possible, however in order to avoid the electrothermal feedback to cause thermal runaway, the term $i^2\alpha R$ should be far enough from the value of G. Following the approach in [15], the maximum applied current is chosen to be:

$$i_{max} = \left(\frac{0.3G}{\alpha R}\right)^{0.5}$$

, hence injecting this together with the approximation for thermal conductance (equation (2.13)) in equation (2.7), the maximum DC responsivity in terms of the bolometer parameters is given by:

$$R_{Vmax} = \frac{0.6R_{bd}\alpha\rho}{W^2d} \tag{2.16}$$

These formulas allow to choose the proper dimension.

- The thickness is chosen as small as possible since both the responsivity and speed are increased as seen from above formulas. However a thinner film is subject to more defects and results in a degraded temperature coefficient of resistance, as pointed out in [18] as long as $\frac{\alpha}{d}$ remains constant (or increases) and reproducibility is maintained, there is a benefit. During the experiments the YBCO thickness fixed to $70nm$ based on research done for cryogenics operation, experimentally investigating the influence of film thickness on the overall performance has not yet been done at room temperature.

- The smaller the area the lower the thermal conductance to the substrate, the devices have a higher relative increase in temperature, leading to higher response. The speed stays the same since the thermal isolation is compensated by an equal decrease of the thermal capacitance (see equations (2.13) and (2.15)). Currently, in parallel to this work, research in the group is being done to scale down the devices even further, to go from micro towards nano-bolometers.

- Antennas are used to couple the radiation into the bolometer (section 2.5). In order to minimize coupling losses, the DC-resistance of the film, $R = \rho\frac{L}{Wd}$, should match the antenna impedance equal to 88.4Ω (equation (2.26)). Considering the thickness fixed at $70nm$ and the resistivity of a typical YBCO microfilm at room-temperature being equal to $1000\mu\Omega cm$, this leads to the constraint: $L/W \simeq 0.62$.

In this project, micro bolometers were made with a thickness of $70nm$ and lengths fixed to 1 and $1,5\mu m$, and widths of 1,1.5,2,3 and $4\mu m$ where optical lithography limits the smallest achievable lateral dimensions.[5] Although most these dimensions do not respect the ratio $L/W \simeq 0.62$, but remains close to this[6], close enough so that the optical coupling was sufficient. The absolute responsivity was evaluated by DC-measurements, the RF-radiation was only employed to characterize how the responsivity evolves as a function of the modulation frequency, hence the question of impedance matching is not crucial. We varied the geometry in order to verify that the responsivity still scaled inversely to the area as reported in [18], to confirm once again that heat transport mainly occurs through the substrate (see equation 2.13).

The thermal boundary resistance has influence on the bolometer performance (as seen in equations (2.13) and (2.15)). This is the interest of this thesis. Unfortunately, in contrast to area reduction, modifying the thermal boundary resistance increases the responsivity at the expense of the speed or vice versa. Nevertheless depending on applications, one of the two might be more essential, it is hence still relevant to be able to tune this parameter.

---

[5] Smaller patterns are possible using electron beam lithography.

[6] For comparison in [19] the mismatch in simulation using similar devices the coupling efficiency is between 68% and 98%, while for a device with resistance of $27k\Omega$ the coupling efficiency is as low as 0.9%

2.4 Detailed dynamics: the two temperature model

Previous discussions assimilated the bolometer to a *single* heater connected via a thermal link to a heat bath. It showed that incoming power heated up the device and this resulted, because of the device isolation, in a temperature change and hence a resistance change leading to a voltage response. This isolation together with the thermal heat capacity determines the dynamics, that is, how the amplitude of the temperature/voltage oscillations evolves as the the frequency of the applied power varies. This single heat reservoir model is however not sufficient to explain to the full extend the frequency response we have measured. A more extended model that comes closer to what is observed is the two-temperature model in which YBCO film is composed of two subsystems, the electron and the phonon reservoir each with its own temperature, different from the temperature of the substrate.

The model relies on the assumption that the electrons and the phonons effective temperature are established uniformly and instantly throughout the whole micro bridge. To be more precise, the intrinsic thermalization times between particles of the same type should be short compared to energy exchange times between the subsystems [20]. In this case a linearized heat balance equations for both subsystems can be written:

$$\frac{dC_eT_e(t)}{dt} = \beta P(t) - G_{ep}\left(T_e\left(t\right) - T_p\left(t\right)\right) - G_{ea}\left(T_e(t) - T_a\right), \tag{2.17a}$$

$$\frac{dC_pT_p(t)}{dt} = (1-\beta)P(t) - G_{pe}\left(T_p(t) - T_e(t)\right) - G_{pa}\left(T_p(t) - T_a\right) - G_{esc}\left(T_p(t) - T_s\right) \tag{2.17b}$$

, where C_e,T_e, C_p,T_p, is the heat capacity and temperature of the electron subsystem, the heat capacity and temperature of the phonon subsystem. T_s,T_a and temperature of the substrate and antenna-pads respectively, those are at the same temperature but are named differently in order to distinguish the cooling process. G_{ep},G_{ea}, represents the electron to phonon cooling efficiency, the electron to antenna cooling efficiency respectively, G_{pe},G_{pa},G_{esc} the phonon to electron cooling efficiency, the phonon to antenna cooling efficiency, the phonon cooling efficiency to the substrate. Transport of heat to the substrate by means of electrons is not possible since the substrate is nonconducting. A fraction β of the total incident power per unit volume $P(t)$ is absorbed by the electron system, the rest is absorbed by the phonon-subsystem. To simplify, the totality of power is assumed to be absorbed by the electron system, $\beta = 1$.

The thermal capacities are considered independent of temperature. Relaxation time constants are introduced by analogy with equation (2.4): $\tau_{ep} \equiv \frac{C_e}{G_{ep}}$, $\tau_{pe} \equiv \frac{C_p}{G_{pe}}$ $\tau_{esc} \equiv \frac{C_p}{G_{esc}}$. Heat flux leaving the electron bath into the phonon bath is equal to the heat flux received by the phonon bath from the electron bath, $G_{ep}(T_e - T_p) = -G_{pe}(T_p - T_e)$. We can note that the thermal boundary resistance is given by $R_{bd} = \frac{\tau_{esc}}{c_p d}$. We can neglect diffusion into the contact pads for electrons since the diffusion length of electrons is estimated to be $l_e = 45nm$, much smaller than the length of the bolometer.[7] Diffusion of phonons into the contact pads for gives a characteristic time constant of $\tau_{diff} = 25ns$ for a $1\mu m$ bridge length L.[8] Considering the average measured value for the thermal boundary resistance of $0.5.10^{-3}cm^2K/W$, a 70 nm YBCO thickness, and the thermal capacity $c_p = 2.44JK^{-1}cm^{-3}$, the escape time of phonons to the film is $\tau_{esc} = 8ns$. Hence the phonon diffusion can not be neglected, however it is still done to simplify the expressions during the mathematical development, it is easily seen that it can be introduced by replacing τ_{esc}^{-1} by $\tau_{effective}^{-1} = \tau_{esc}^{-1} + \tau_{diff}^{-1}$ in the final expression.

Defining c_e and c_p as the specific heat capacities and V as the volume of the bolometer, and knowing that the specific heats have a negligible temperature dependence for the small signal analysis, the equations become:

$$c_e \frac{dT_e(t)}{dt} = \frac{P(t)}{V} - \frac{c_e}{\tau_{ep}}(T_e(t) - T_p(t)) \tag{2.18a}$$

$$c_p \frac{dT_p(t)}{dt} = \frac{c_e}{\tau_{ep}}(T_p(t) - T_e(t)) - \frac{c_p}{\tau_{esc}}(T_p(t) - T_s) \tag{2.18b}$$

If the incoming signal is an amplitude modulated signal at frequency ω , $P(t) = P_0 + \Delta P e^{j\omega t}$, a possible solution to the pair of above equations is one where the temperatures of the subsystems oscillate at the same frequency, $T_e(t) = T_{e0} + \Delta T_e e^{j\omega t}$, $T_p(t) = T_{p0} + \Delta T_p e^{j\omega t}$. It is solved by separating the time varying part from the time independent part. The temperature of the substrate is assumed to remain fixed in time. [9] For the time-varying signals, this yields:

$$j\omega c_e \Delta T_e = \frac{\Delta P}{V} - \frac{c_e}{\tau_{ep}}(\Delta T_e - \Delta T_p), \tag{2.19a}$$

$$j\omega c_p \Delta T_p = \frac{c_e}{\tau_{ep}}(\Delta T_e - \Delta T_p) - \frac{c_p}{\tau_{esc}}(\Delta T_p - T_s). \tag{2.19b}$$

Rewriting equation (2.19b):

$$\Delta T_p = \frac{\frac{c_e}{\tau_{ep}}\Delta T_e}{j\omega c_p + \frac{c_e}{\tau_{ep}} + \frac{c_p}{\tau_{esc}}} \tag{2.20}$$

---

[7] $l_e \simeq \pi\sqrt{D_e t_{ep}}$, where $D_e = \frac{\kappa_e}{c_e}$ is the electron thermal diffusivity, κ_e the electron thermal conductivity in the a-b plane (lateral plane of the YBCO film), c_e the electron specific heat capacity [17]. At room temperature: $\kappa_e = 0.01Wcm^{-1}K^{-1}$ [21], $c_e = 0.072JK^{-1}cm^{-3}$, [22], $\tau_{ep} = 10ps$ estimated from the RF measurements.

[8] $\tau_{diff} = L^2/(\pi^2 D_p)$, where $D_p = \kappa_p/c_p$ is the phonon thermal diffusivity, κ_p the phonon thermal conductivity in the a-b plane, c_p the phonon specific heat capacity [17]. At room temperature: $\kappa_p = 0.1Wcm^{-1}K^{-1}$ [23], $c_p = 2.44JK^{-1}cm^{-3}$. The latter was obtained using the Debye model (explained e.g. in [24]) with a Debye temperature of 400 K from [25], this value is in accordance with c_p reported in [26], for the unit conversion YBCO density of $1.635kg/cm^3$ was used [27].

[9] This assumes an infinite thermal conductivity, i.e. works as a perfect heat sink, this will be showed later on. Also, we will make use the principle of superposition to introduce phonon diffusion inside the substrate without having to modify the final equation (2.23) calculated.

, this is now injected in equation (2.19a), and the norm of ΔT_e is calculated. The solution is found in [28]:

$$\Delta T_e = \Delta P \frac{\tau_{ep} + (c_e/c_p)\tau_{esc}}{c_e V} \sqrt{\frac{1 + (\omega\tau_\phi)^2}{\left(1 + (\omega\tau_1)^2\right)\left(1 + (\omega\tau_2)^2\right)}} \tag{2.21}$$

,with

$$\begin{aligned} {\tau_{1,2}}^{-1} &= \frac{1}{2\tau}\left(1 \pm \left(1 - 4\frac{\tau^2}{\tau_{ep}\tau_{esc}}\right)^{1/2}\right), \\ \tau^{-1} &= {\tau_{esc}}^{-1} + {\tau_{ep}}^{-1} + {\tau_p}^{-1}, \\ {\tau_\phi}^{-1} &= {\tau_{esc}}^{-1} + {\tau_p}^{-1}, \\ \tau_p &= \tau_{ep} c_p / c_e. \end{aligned} \tag{2.22}$$

For YBCO at room temperature, c_p/c_e is estimated to be 34. The values of τ_{ep} for YBCO at room temperature is not available in literature, however a value can be extrapolated after measurement and using the model, this gives a value of typically 10 ps. The same reasoning is applied to the escape time where a typical value for a 70 nm YBCO thickness is 10 ns.

This allows to simplify the expressions in equations (2.22), as pointed out in [17]:

$$\tau_1 \simeq \tau_{ep}, \tau_2 \simeq \tau_{es}, \tau_\phi \simeq \tau_p,$$

so that equation (2.21) becomes, using also the fact that by identification[10] $\tau_p = \tau_{pe}$:

$$\Delta T_e = \Delta P \frac{\tau_{ep} + (c_e/c_p)\tau_{esc}}{c_e V} \sqrt{\frac{1 + (\omega\tau_{pe})^2}{\left(1 + (\omega\tau_{ep})^2\right)\left(1 + (\omega\tau_{esc})^2\right)}}. \tag{2.23}$$

The temperature change of the electron system is determines the resistance change measured, $\Delta R = \frac{dR}{dT}\Delta T_e$. For a current biased bolometer, a change in voltage occurs according to:

$$\Delta V = I \left.\frac{dR}{dT}\right|_{T_{e0}} \Delta T_e \tag{2.24}$$

The voltage responsivity is obtained by combining equations (2.23) and (2.24):

$$R_V \equiv \frac{\Delta V}{\Delta P} = I \frac{dR}{dT} \frac{\tau_{ep} + (c_e/c_p)\tau_{esc}}{c_e V} \sqrt{\frac{1 + (\omega\tau_{pe})^2}{\left(1 + (\omega\tau_{ep})^2\right)\left(1 + (\omega\tau_{esc})^2\right)}}. \tag{2.25}$$

---

[10] And additionally to this the fact that $\tau_{pe} = \tau_{ep} c_p / c_e$ which is obtained by knowing $G_{ep}(T_e - T_p) = -G_{pe}(T_p - T_e)$ and the definition of the time constants.

At low modulation frequency the stationary conditions for all processes are fulfilled, i.e. single heat bath approach is valid (equation (2.25) simplifies to equation (2.7)), the response is independent of the incoming photon frequency. At some point the heat can not be evacuated fast enough between the film and the substrate, this is created by the thermal boundary resistance which literally acts as the bottleneck, it hinders the phonons of the substrate to be able to participate in the cooling, the temperature oscillations become smaller resulting in a decrease in the voltage response. Increasing the frequency even further a second plateau is observed, associated with the electron and phonon subsystems, phonons in the film act as a heat sink for the electrons,[11] at some point even the phonons in the films can not remove the heat fast enough, the point at which this occurs is dictated by the electron-phonon interaction time, and the response starts to drop again.

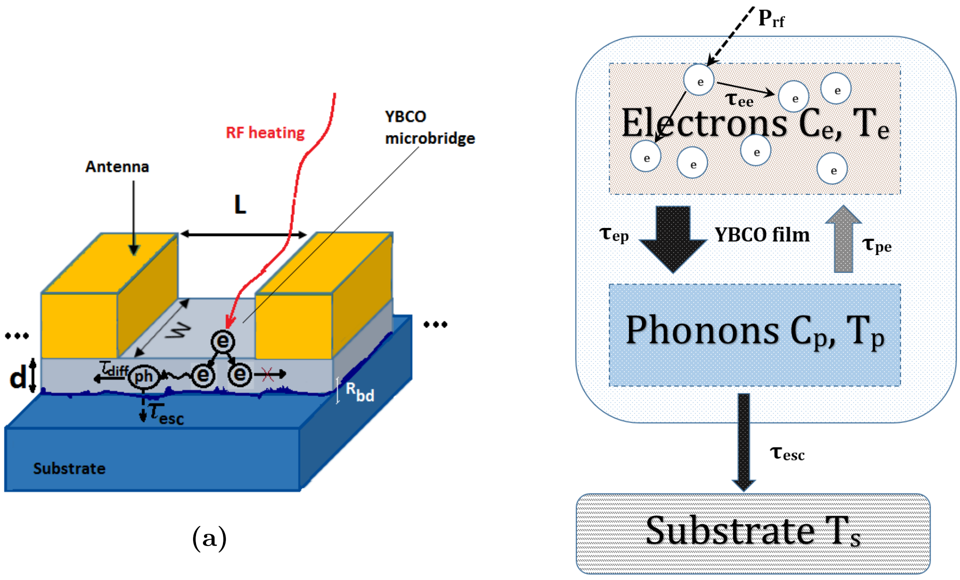

(a)

(b)

Figure 2.4: (a) Flow diagram of the thermal process on the physical device and the summarized structure. Principle of energy transfer in the bolometer with the related interaction times. (b) equivalent of (a) in a block diagram, diffusion into the contact pads and substrate diffusion is neglected. Pictures adapted from [17] and [29].

There remains two heat contributions which could have an effect on the frequency dependency of the response. First vertical diffusion in the YBCO film, the temperature in the film is found to be uniform based on [30]. Secondly and most importantly an effect commonly observed is heat diffusion inside the substrate, the substrate in previous derivation was assumed to be an ideal thermal batch, this means that the temperature is always fixed at T_s, even just underneath the interface. However the finite conductivity of the substrate causes a thermal gradient to appear right below the heated film, and

---

[11] A bolometer exploiting this effect is referred to in literature as 'hot electron bolometer'

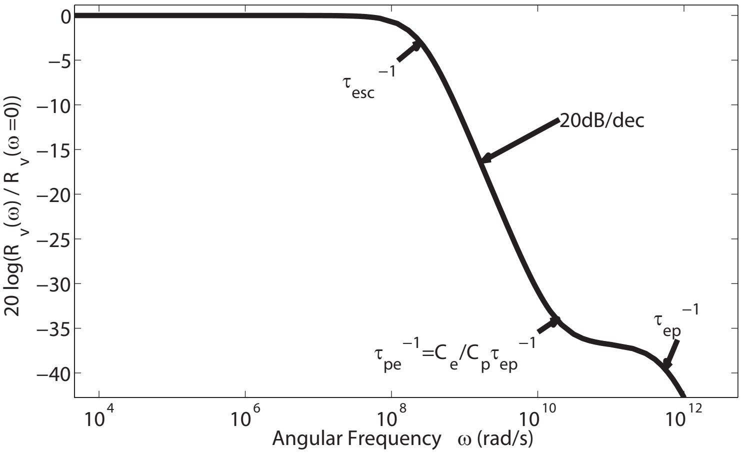

Figure 2.5: Prediction of the (modulation) frequency behavior of the bolometer of the two temperature model, using equation (2.25) with $c_p = 2.44JK^{-1}cm^{-3}$, $c_e = 0.072JK^{-1}cm^{-3}$, $\tau_{esc} = 4ns$ $\tau_{ep} = 1.7ps$. Three regions are identifiable, a low frequency plateau associated with the classical bolometric regime, followed by a roll-off with a cutoff frequency at the escape time of phonons to the films (associated with the thermal boundary resistance), and a high frequency plateau where the electrons are heated above the film phonon temperature, followed by a roll-off associated with the electron phonon interaction time.

causes an additional thermal resistance. Hu et al. describe an analytical solution by solving the two dimensional diffusion equation assuming a circular contact area of the film with the substrate, with the boundary condition $T_s(r = \infty) = T_s$,[12] and calculating the thermal conductance G_s associated with this thermal profile [31]. Written in terms of thermal resistance,

$$R_s(f) \equiv 1/G_s = \frac{a}{A\kappa_s}\left[\left(1 + \frac{a}{l_s(f)}\right)^2 + \left(\frac{a}{l_s(f)}\right)^2\right]^{-1}$$

, with A the bolometer area, κ_s the substrate thermal conductivity, $l_s = \sqrt{D_s/(\pi f)}$, and $a = L/\sqrt{\pi}$, with L the device length.

The resistance between the electron and the substrate is defined as $R_{e-s} \equiv \Delta T_e/P$ where ΔT_e where the electron temperature of the film obtained in equation (2.23). As suggested in [17], R_{e-s} appears in series with R_s, leading to:

$$R_{tot} = R_{e-s} + R_s$$

Figure 2.6 shows that for our bolometers substrate diffusion is negligible, this is due to the very high thermal conductivity κ_s of sapphire.

---

[12] This assumption is justified by the fact that the bolometer dimensions is much smaller than the substrate thickness

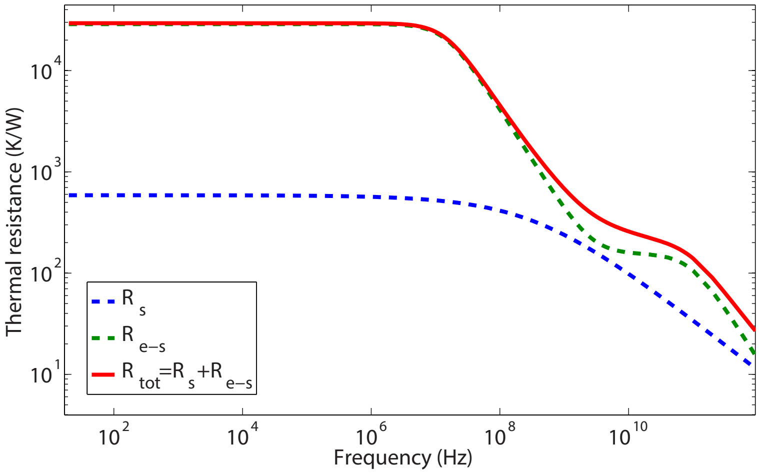

Figure 2.6: Thermal resistance of the bolometer as a function of frequency. Parameters used: for the YBCO film: $L = 1.5\mu m$, $d = 70nm$, $c_e = 0.072JK^{-1}cm^{-3}$ $c_p = 2.44J/cm^3K$, $\tau_{esc} = 11ns$, for the substrate:$\kappa_s = 6.4Wcm^{-1}K^{-1}$; $c_s = 0.39JK^{-1}cm^{-3}$. Substrate diffusion can be neglected: it is seen that R_{e-s} almost coincides with R_{tot}.

2.5 Coupling of the radiation

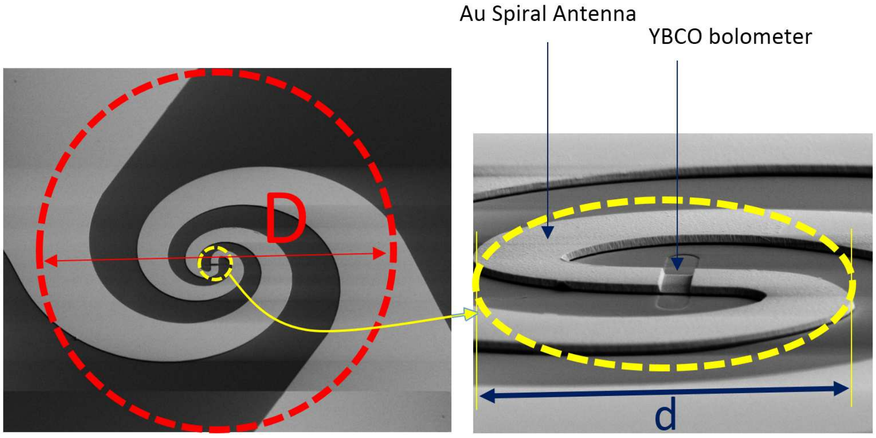

Figure 2.7: An image of the final device, taken with scanning electron microscope adapted from [12], showing the log spiral antenna and the YBCO microbridge. The inner $d = 20\mu m$ and outer $D = 230\mu m$ diameter determine the lower and higher cuttoff wavelengths. Although the antenna must be at least comparable in size to the wavelength, the dimensions of the region in which the infrared power is thermalized can be made much smaller [31].

2.5.1 Antenna integrated bolometers.

In order to couple THz radiation into the bolometer a common technique is to use a planar antenna, with characteristic dimensions comparable to the incident wavelengths (see next paragraph), this antenna is planar and situated on the same chip as the bolometer.[13] In this work a logarithmic spiral antenna was used, based on the work in [20], it consists of two spiral-shaped arms which are connected by the detector bridge in the center of the structure. RF-current generated by the antenna necessarily pass through the exposed YBCO film, the resistance is much higher in that region (because of the higher resistivity of YBCO with respect to gold), therefore heat develops in the microbridge. The advantage of a log-spiral design is that it is inherently broadband and has a nearly frequency independent real impedance whereas the imaginary part is approximately zero, this allows to avoid a design of a complex RF matching circuit. Also, their fabrication is quite easily done using lithographic techniques (see next chapter).

Since the design is self-complementary (i.e. the structure covered by metal is the same as the structure of the dielectric), as a corollary of Babinets' principle, the antenna-impedance can be estimated by [33][34]:

$$Z_{antenna} = \frac{Z_0}{\sqrt{[2(1+\epsilon)]}} = 88.4\Omega \tag{2.26}$$

, where $Z_0 = \sqrt{\mu_0/\epsilon_0} = 377$ is the characteristic impedance of free space, and $\epsilon = 10$, the dielectric constant of sapphire[14]. This value is important in order to achieve high coupling efficiency between antenna and detector: Assuming the RF-impedance of the detector element (the YBCO microbridge) equal to the DC-resistance, and knowing the resistivity of the film, a proper geometry should be chosen to satisfy this constraint (the dimensions are given in section 2.3).

The operating spectral band of the detector can easily be determined by the antenna design, a rule of thumb for the lower and higher frequency cutoff is given in [20]: $\lambda_{max} = 6D$ and $\lambda_{min} = 20d$, where D and d are the outer diameter of the smallest circle that encompasses the spiral structure and d the inner diameter of the smallest circle at which the arms still obey the spiral equation (see figure 2.7). In the case of our research $D = 230\mu m$ and $d = 20\mu m$, hence $f_{min} = 217GHz$ and $f_{max} = 740GHz$. In this work we use RF frequencies at 80 GHz, although this does not fall into the above mentioned interval, the measured signal strength is still high enough.[15]

---

[13] As an alternative to on-chip integrated planar antennas, at microwave and submillimeter frequencies up to 0.5 THz the radiation is coupled most often to the bolometer by way of wave guides, which provide for precise low-loss coupling. At increasing frequency, the dimensions of the waveguide have to scale with the wavelength and become unpractically small[32]. Although corrugated horns can be fabricated for frequencies of a few terahertz they are getting more expensive to manufacture and the effect of misalignments becomes more severe [20].

[14] Sapphire is anisotropic, its dielectric constant varies between 8.9 and 11.11 [35].

[15] It is not possible generate higher carrier frequencies with the available microwave equipment. The choice of the frequency band is based on a set of different experimental tests besides the ones conducted in this work, for instance characterization of the optical responsivity of the bolometers (using sources lying in the frequency band of the antenna).

2.5.2 THz Lenses

The antenna placed on a dielectric substrate, assuming it operates in transmission mode, primarily radiates into the substrate [33]. For this reason, and by the reciprocity principle, backside illumination is used in order to couple most of the light into the antenna (now in receiver mode). More specifically, the ratio between power coupled into the substrate, with relative dielectric constant ϵ, and air scales more or less as $\epsilon^{3/2}$ [33]. For sapphire $\epsilon_{sapphire} \simeq 10$, this means a ratio of more than 95% [16]. However this is not accounting for substrate losses: the main beam of such antenna is rather broad [16], and hence a significant portion of rays radiating from the antenna are subject to 'total internal refraction, those having an angle incident on the sapphire-air interface higher than the critical angle $\theta_{cr} = \arcsin(1/\sqrt{\epsilon_{substrate}})$. The problem is solved by introducing a substrate lens as shown in figure 2.8), the same rays that were previously reflected now face the surface almost perpendicularly and are hence (at least partially) transmitted. The lens has to have as close a dielectric constant as possible to the substrate material, therefore a silicon lens is appropriate ($\epsilon_{Si} = 11.8$). Different shapes are possible, hemispherical, hyper hemispherical or ellipsoidal. An elliptical lens is used in this work, justification of this choice falls outside of the scope of this work, but are explained in [36]. Although not done, to improve the coupling even further, a quarter-wavelength anti-reflection coating with appropriate thickness can be applied on the lens, but then as the name suggests this only is improved in a specific frequency range [37][38].

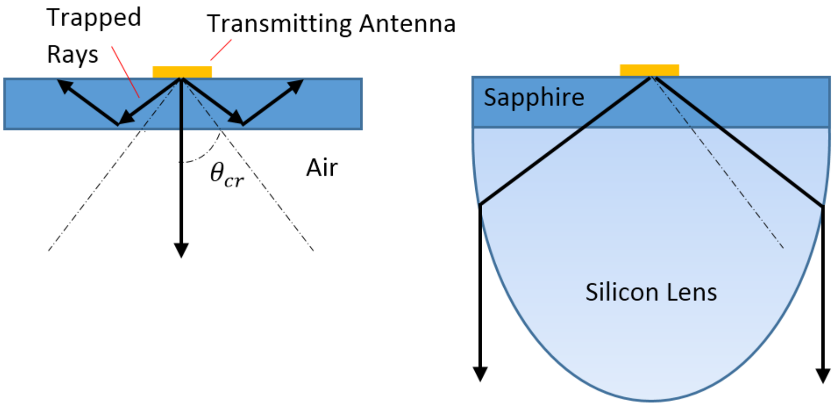

Figure 2.8: Schematic drawing showing the relevance of using a lens: substrate modes are suppressed and the coupling of the beam to the antenna is increased. Note that the antenna is operated in transmission mode but by reciprocity a high outwards coupling from antenna to the air where the receiver is situated, is equal to a high inwards coupling from the source, located at the position where the receiver was, to the antenna (now acting as receiver). Picture inspired by [16],[33].

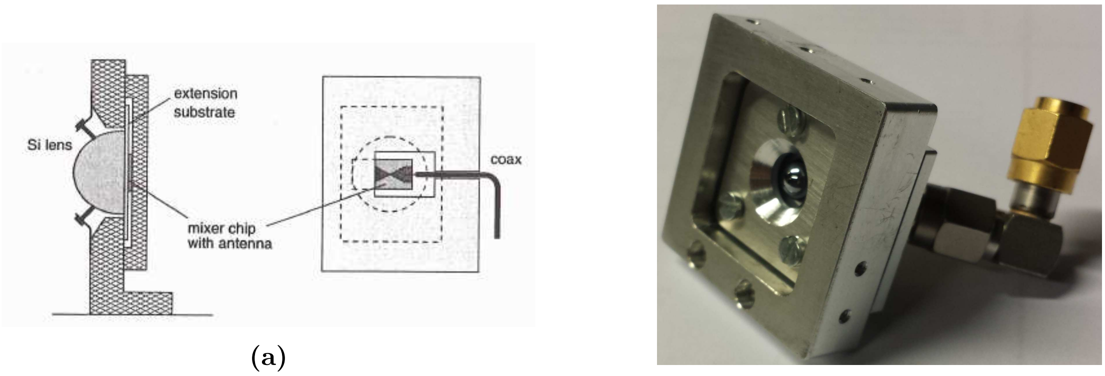

(a)

(b)

Figure 2.9: (a)Schematic drawing of the final device mount for backside illumination. The lens is well visible on the actual mount (b).

2.6 Material selection

YBCO was used as the absorbing and transducer material. Originally the choice of YBCO was made because of its superconductive properties: the bolometer is operated at cryogenic temperatures around 88 K where the bolometer undergoes a transition to super-conducting state, this transition is characterized by a very high drop in resistance in a short temperature range leading to very high responsivity ($R_v = 190V/W$ (read-out limited), [39]). Later on the group at Chalmers measured the exact same bolometer at room temperature, and even though (as expected) the device is less responsive ($R_v = 15V/W$), it is still very fast, a comparison with other room temperature detectors can be found in [18]. Metallic films in bolometers can work as well, having a TCR comparable to YBCO, however conductivity of metals is so high that in order to make a proper impedance match with the antenna (impedance around $50 - 150\Omega$) the thickness of the films should be very much reduced, such thin films (below 20 nm) are very difficult to grow uniformly. Hence only a few metals that have a low enough conductivity can be taken into consideration [40]. Semiconductor based films have the advantage of having a much higher TCR (100 times higher),[16] however the resistance ($R = k\Omega$ -$M\Omega$, [19]) is much higher than the antenna impedance, leading to significant reflection losses.[17][18] To decrease the resistance, the semiconductor can be doped but this leads to a much decreased TCR, leading to a responsivity loss. Recently however a

---

[16] The high TCR in intrinsic semiconductors is due because of the exponential dependence on temperature of the charge carrier concentration

[17] Design of high impedance antennas is possible [41], but at the expense of a reduced bandwidth of the antenna

[18] Semiconductor bolometers (VOx) with $100\mu m * 100\mu m$ size is used in multi pixel arrays for detection in the infrared range, the TCR combined with a suspended bridge design leads to very high responses up to several kV/W (compared to $15V/W$ for the YBCO bolometer) [42] This suspension results in slow devices (ms seconds instead of ns), also they can not be used for THz detection because of the large wavelength in the THz (they are not antenna integrated) [19].

paper was published using planar antenna integrated semiconducting PBCO thin films showing higher responsivity than (and similar speed as) the YBCO room temperature detectors [19].

The substrate on which the YBCO film is deposited has to satisfy certain properties, a good summary of the it has to satisfy is found in [32] and [43]:

- High thermal conductivity - the substrate acts as a thermostat [14], hot phonons coming from the small YBCO microstrip are efficiently evacuated[19]
- Chemical compatibility - no chemical reaction at the interface that can degrade the film
- Mechanical strength - should not bend or crack process during handling
- Crystalline lattice match - to provide epitaxial growth.
- Atomically smooth surface - to provide epitaxial growth
- Thermal stability - should withstand temperatures up to 900° C
- Thermal expansion coefficient - to avoid stress and cracks during handling
- Electrically isolating- no interference with the electrical circuit

Epitaxy refers to the growth of a substance (here crystalline YBCO) on the crystal surface of a substrate, where the growth is oriented, i.e. with a consistent crystallographic relationship between those two [44], if this condition is not satisfied this will result in uncontrolled defects degrading the performance and increasing variability. Several substrates answer above mentioned requirements, like $LaAlO_3$ and $SrTO_3$ which provide the best lattice match [45]. However the device is backward illuminated using THz frequencies (i.e. the waves travel through the substrate prior to reaching the bolometer for reasons explain in section 2.5) so dielectric constant matching with the silicon lens, absorbtion, low loss tangent are thus factors to consider as well in addition to the ones mentioned above ([32],[45]). $LaAlO_3$, $SrTO_3$ do not meet these requirements, Al_2O_3 and MgO do, at the expense of bigger lattice mismatch [32]. Research in the group had already started using single crystalline Al_2O_3,also called sapphire ($\epsilon_r = 5 - 12$, loss tangent = 8.4 -10.6 (at 77 K)), hence the choice to continue with this material. Sapphire is anisotropic, the crystallographic 'R-plane' is used as the plane on which the YBCO is grown ($1\bar{1}02$). The mismatch between both materials, if directly grown on top, is 6% on the a-axis and 12% for the b-axis. Also chemical reactions occur between the sapphire and the YBCO.[20] leading to a suppressed T_c (and hence lower quality films) To solve

---

[19] It might be argued that the substrate should have a low thermal conductivity in order to increase the device responsivity. However this leads to an frequency dependence of the response and not under control of the resistive film (the boundary resistance) anymore (see e.g. [17] or [31]) .

[20] This chemical reaction occurs by diffusion of aluminum contained in the sapphire to the YBCO film [46]

these two issues, a thin layer ,typically between 8 and 100 nm, is sandwiched between the the sapphire and the YBCO, called the 'buffer layer'. For this particular 'R-plane', CeO_2 as a buffer layer has been found to yield the best results. The resulting lattice mismatch with the YBCO is now greatly reduced, 0.2% and 1.3% along the a and b axis respectively [47] providing an even better lattice match than $LaAlO_3$ or $SrTO_3$ [45]. In crystallographic terms it is summarized as: $YBCO(001) \parallel CeO_2(001) \parallel Al_2O_3(1\bar{1}02)$. Although quite commonly used as a choice in research, investigation of the actual the thickness of this buffer layer is limited to evaluate film quality in terms of Tc [48], no paper mentions the effect of the thickness on the bolometric frequency response.

2.7 Brief comparison with other detectors

In this short section, a brief comparison with some other teraherzt direct detectors is made, by means of a table (table 2.1). It shows that the ultimate detector having all the desired properties is not present (i.e. fast, large (carrier) frequency range, high voltage responsivity, low NEP, room temperature operation).

Detector type	Speed (s)	Frequency Range (THz)	Responsivity (V/W)	NEP $(W/Hz^{0.5})$	T (K)
Composite Si_3N_4 bolometer [49]	11×10^{-3}	$0.06 - 1.2$	9×10^7	2×10^{-17}	0.3
Superconducting YBCO microbolometer [39]	300×10^{-12}	$0.3 - 1.6$	190	20×10^{-12}	77
Pyroelectric detector [50]	200×10^{-3}	$0.1 - 30$	10^5	10×10^{-10}	295
Golay cell [51]	15×10^{-3}	$0.2 - 20$	10^5	10×10^{-10}	295
V antenna Suspended bridge Bi bolometer [40]	1×10^{-6}	x	100	30×10^{-12}	295
Schottky diode [52]	10×10^{-12}	$0.3 - 1.2$	$1000 - 125$	10×10^{-12} -80×10^{-12}	295
Room temperature YBCO microbolometer [18]	2.5×10^{-9}	$0.3 - 1.6$	15	450×10^{-12}	295
Room temperature YBCO nanobolometer [53]	2.5×10^{-9}	$0.3 - 1.6$	45	50×10^{-12}	295

Table 2.1: Comparison of a few THz (direct) detectors based on different figures of merit. The speed refers to the inverse of the characteristic time constant as defined in chapter 2. The frequency range indicates the range in which the corresponding voltage response was measured. NEP refers to the Noise Equivalent Power, defined as the incident signal power required to obtain a signal equal to the noise in a one Hz bandwidth [14], or equal to the noise voltage divided by the voltage responsivity. The videobandwith corresponding to the values of NEP indicated is left unspecified in this comparison. The temperature (abreviated by T) refers to the temperature at which the device is operated. Schottky diodes are the most sensitive room temperature detectors below 1 THz, but as the frequency increases the voltage response and the NEP starts to increase. Because of the lack of information on the noise in the schottky diode used here, the NEP was deduced using a noise voltage equal to $1 \times 10^{-8} V/Hz^{0.5}$ from zero biased schottky diode in-house data. A higher response is obtained for the nanobolometers while speed is maintained with respect to the same bolometer with micron sized dimensions. Bridge suspension (instead of direct contact with substrate) results in a higher response at the expense of speed.

3

Fabrication

THE Terahertz bolometers are fabricated in the cleanroom of the Department of Microtechnology and Nanoscience in Chalmers, MC2. The final device is shown in Fig. 2.7, it simply consists of a piece of YBCO coupled to a spiral antenna. The fabrication procedure is relevant to explain, since errors or modifications in the fabrication steps can affect the performance of the bolometers.

3.1 Substrate preparation with Pulsed Laser Deposition

Towards fabrication, a YBCO film with a thickness of 70 nm is grown on top of a 0.43 mm thick 10 × 10 mm polished R-plane sapphire wafer. This requires the deposition of a CeO_2 bufferlayer (see section 2.6). On top of the YBCO film a gold layer of 20 nm is deposited in-situ. The use of the 20 nm gold layer is to avoid the YBCO to be unnecessarily exposed to the environment during the further processing as well and allows to have an improved YBCO/Au electrical contact resistance (compared to a situation were the gold is deposited ex-situ). The chip after the multiple depositions is shown in figure 3.2.

First, the $Ce0_2$ buffer layer is deposited using RF sputtering at substrate temperature of $750°C$ and oxygen pressure of $p_{0_2} = 0.1mbar$. After the deposition the oxygen pressure was raised to 730 mbar and the substrate cooled down to room temperature at a rate of $10°C/min$. The thickness is a variable parameter under investigation, we tried (approximately) 12, 25 and 50 nm.

Next follows the deposition of the YBCO. High Tc superconductors have a complex crystalline structure and so require the use of a pulsed laser deposition (PLD).[1] A KrF laser emits pulses focused on a rotating target containing bulk amorphous YBCO material. This results in emission of particles in the form a plume. Particles from this plume

---

[1] There exists other techniques to deposit crystalline YBCO, but PLD is probably the most widely used; advantages and disadvantages of this technique are discussed in [32].

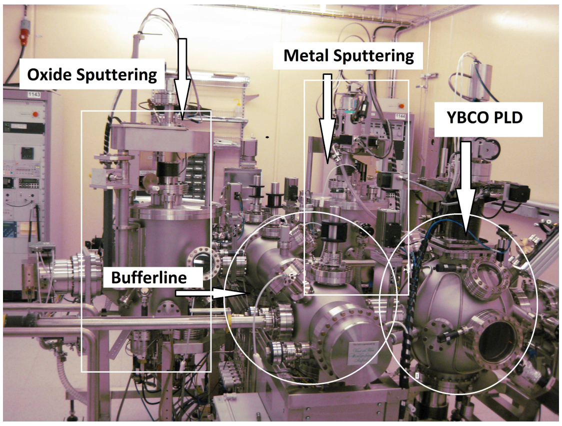

Figure 3.1: The deposition system used is equipped with three chambers (tool 1142): Two of them are dedicated to metal and oxide sputtering while the third chamber is dedicated only to YBCO deposition. These three chambers are connected through a buffer line which is kept at a base pressure of $10^{-7} mbar$ allowing for in-situ multilayered deposition of the different materials.

are deposited on the substrate and the films starts to grow *epitaxially* . The physics involved in this PLD process are very complex, not surprisingly the film that is obtained is very sensitive to the exact condition of deposition. In order to get the YBCO in its fully oxygenated structure an external source provides oxygen in the chamber as well. A list of parameters that influence the YBCO film quality in terms of crystallinity, uniformity and stoichiometry is given below:

1.Deposition temperature - under investigation in this work: varied between $780°C$ and $855°C$ for the different samples

2.Oxygen pressure during deposition - $p_{O_2} = 0.6mbar$

3.Laser energy- $1.6J/cm^2$

4.Laser frequency - $4Hz$

5.Substrate to target separation - $53mm$

6.Oxygen pressure after deposition, during cool down - $p_{O_2} = 860mbar$

7.Annealing conditions - not applied here since the critical temperature (Tc) remained unaffected.

deposition temperature *Elevated deposition temperatures and oxygen pressure during the growth lead in general to high critical temperature at the expense of surface morphology* according to [54]. However, smoother surfaces are obtained if the deposition temperature and oxygen pressure is *lower* [54]. Hence it is a priori not clear what choice of parameters will give the best results.

The YBCO thickness is determined by the number of pulses, to obtain 70 nm, this amount was 1250. Lastly the 20 nm gold layer is deposited using RF-sputtering.

The purpose is to fabricate 10 bolometers of different sizes on the same wafer. The following subsections will explain in detail how the fabrication was carried out. For convenience and without loss of information, the illustrations are shown for only one

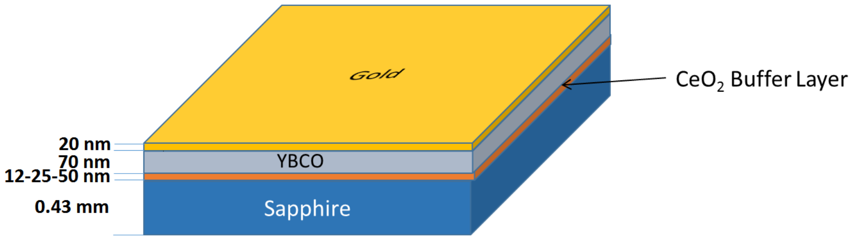

Figure 3.2: The wafer after PLD

device.

3.2 Introducing Optical Lithography

In order to fabricate and pattern layered structures, optical lithography is used in this work. This technique requires an optical mask, a flat transparent glass object covered in specific areas with light-impenetrable chromium representing the features that needs to be transferred onto the wafer. This mask is placed directly on top of a light-sensitive material called photoresist (abbreviated as 'resist') that is covering the wafer. After an eventual allignement of the mask with respect to the wafer, UV light is applied (usually) perpendicular to mask. The light reaches the photoresist on places where no coverage is provided by the mask, affecting (locally) the chemical properties of the resist. Using the appropriate developer, the light exposed part or light unexposed gets removed depending on the nature of the resit, a 'positive' and 'negative' resist, respectively (see figure 3.3). The features on the mask are hence transferred to the resist. The patterned resist can now be used as a mask for deposition or etching.

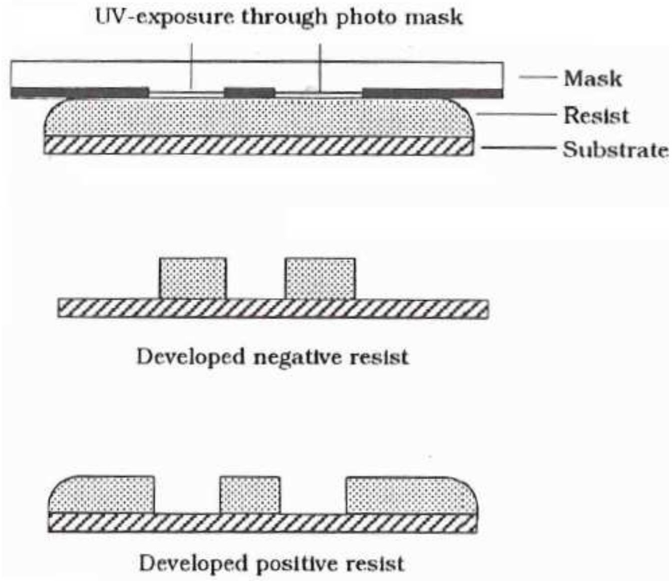

Figure 3.3: Principle of optical lithography.

3.3 Bolometer Length Definition

The purpose of this step is to define the length of the bolometer. Throughout this thesis, dimensions are defined with respect to the current flow: the length of the bolometer is referred to as the dimension corresponding to the (average) direction along which the electrons propagate when a DC current is applied on the contact pads.

Fabrication starts by spin-coating a layer of HDMS primer (spinning for 30 sec with a speed of 4000 rpm). This is done to improve the adhesion of the resist which is spin-coated right after that. AZ5214E resist is used, and the spinning is performed for 30 sec with 4000 rpm. Next, a soft baking is performed at 110 degrees C for 60 seconds. Before lithographically defining the features, the resist on the the edges removed with an *edge bead exposure* (figure 3.4). The reason for this is that on the edges the resist is usually much thicker than at the center and hence might prohibit a good contact of the mask with the chip which is important to get the exact features of the mask on the resist. The edge bead exposure is done with a mask with an dark (light impenetrable) square pattern just smaller than the area of the chip for 60 seconds under UV light. The UV light intensity in all the exposures is equal to $6mW/cm^2$. Since the resist at that stage still acts as a positive resist, the exposed edges will be dissolved in the developer solution: the chip is immersed in AZ351B developer and water mixture (ratio 1:5) during 60 seconds, followed by water rinse and N_2 blow dry.

To define the patterns lithographically, we use what is called 'image reversal lithography' IRL. IRL is carried out using resist which in the first exposure step acts as a positive resist, the exposed parts are soluble. However, after applying a baking step and extra UV exposure the previously soluble parts become insoluble and the process

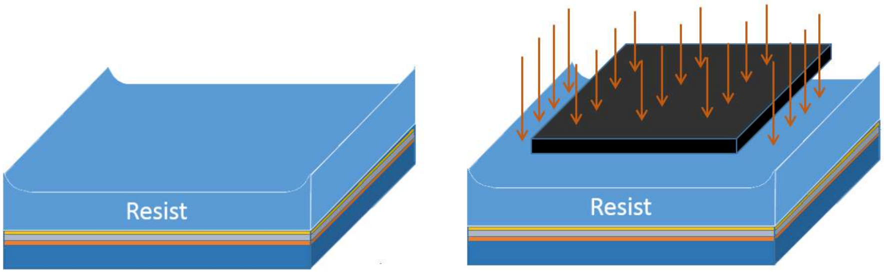

Figure 3.4: The chip after depositing the resist. The resist on the edges is thicker and will prohibit good contact with the mask, so the resist is removed by exposing and then developing. The bufferlayer will be omitted in following figures although it remains present below the YBCO film.

becomes equivalent to using a negative resist lithography in the sense that the the final pattern has resist remaining on the places where the mask allows light to penetrate. Figure 3.5 depicts the IRL process.

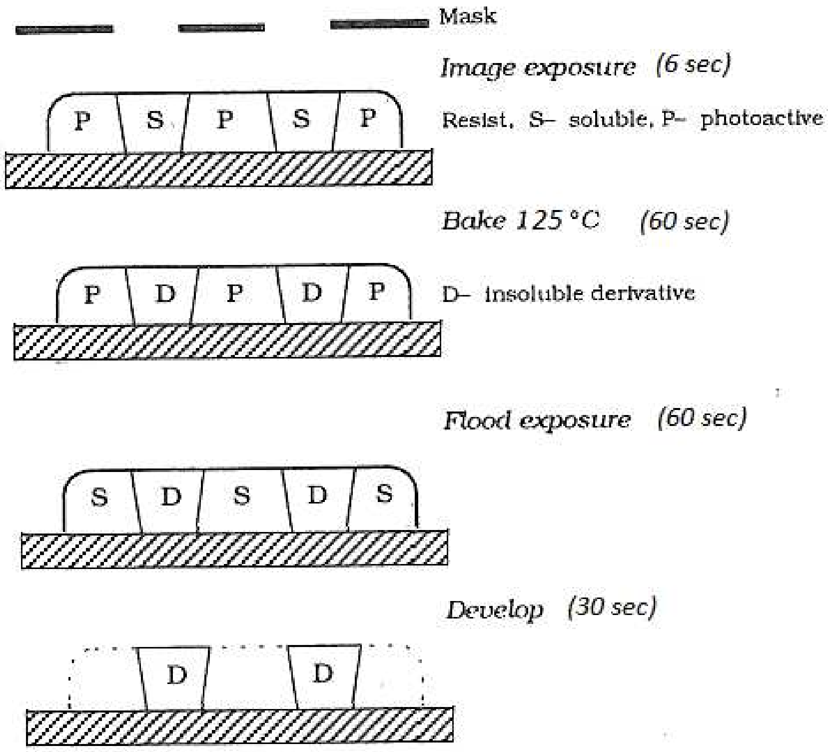

Figure 3.5: Image reversal lithography, note that the edges of the wafer are free of resist. Picture adapted from [13]

Since the image will be 'reversed', a mask is used which is chromium covered everywhere except in tiny rectangles where the bolometers will later be situated.[2]

Using the Karl Süss mask alligner (Tool 210), this mask is placed on top of the resist and exposed to UV light for 6 seconds. As was mentioned, the resist acts as a positive resist, the exposed parts become soluble.

Towards IRL, we bake the chip for 60 seconds at 125 degrees C. The areas that were just exposed by the light are now inert to the developer while the unexposed areas remain photosensitive.

After this we expose the whole chip again without any mask for 60 seconds, also called flood exposure, followed up by 30 seconds resist developing in the developer AZ351B solution(ratio and AZ351B - water = 1:5) and a rinse in water. To completely remove unwanted residuals of resist we proceed to plasma descumming, the chip is placed in shortly in a weak oxygen plasma. The chip at this stage of the process looks as shown in figure 3.6.

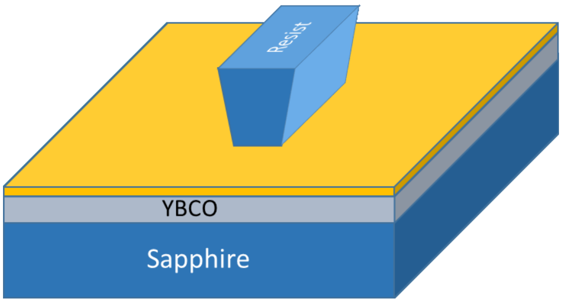

Figure 3.6: The chip after applying image reversal lithography and developing the resist.

The reason to use this image reversal lithography is justified by the fact that it allows us to obtain a resist pattern with an undercut, facilitating lift-off. This undercut is a result of the scattering properties of light so that light is less and less intense on the edges as it goes deeper into the substrate. A negative resist (e.g. me-N 1410) can also achieve this undercut, but it does not allow to combine it with the edge-bead exposure step, in this case the contact between resist and mask is not as tight and less well defined features are the result.

After IRL, a Ti/Au/Ti (10 nm/ 250 nm/10 nm) stack is deposited using the Lesker Evaporator (Tool 451). The result of this step is shown in figure 3.7. The first Ti layer is used to improve adhesion of the 250 nm layer of gold with the wafer. The 250 nm of gold itself will be etched in the right shape to form the antenna and the contact pads. The upper Ti layer is used as an etching mask during subsequent process steps. The figure shows the undercut where no material is being deposited. The resist undercut prevents contact between the resist and material deposited on the substrate.

Next metal 'lift-off' is performed, the result is shown in figure 3.8. The lift-off is effectuated by putting the chip in $70°C$ warm acetone: The resist is dissolved by the

---

[2] Apart from these rectangles, the mask also contains allignment marks. These marks will serve in a later step to allign the wafer with another mask that contains other features.

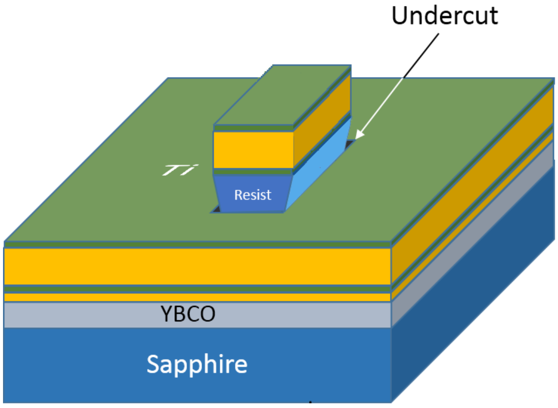

Figure 3.7: The chip after the deposition of Ti/Au/Ti metal stack. The undercut is also shown. The scales are unrepresentative: the resist-thickness is more than a micron while the deposited material Ti/Au/Ti is 270 nm in total.

acetone so that the metal structure on top of the resist starts to separate from the chip. Low power ultrasounds are applied to facilitate the process.

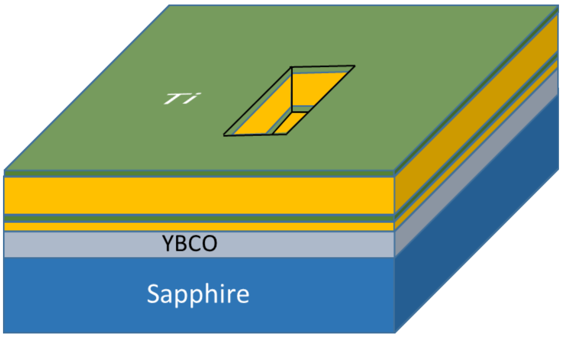

Figure 3.8: The chip after resist lift-off.

In a last step the exposed 20 nm gold layer is etched using an acid gold etchant solution. Acid ($KI : I_2$) and water ratio of 1:10 is used for 8 seconds, etching all gold that is not protected by the Ti, followed by water rinsing for 4 seconds. This results in exposing the part of YBCO (also unsensitive to the acid solution): this exposed region will form part the final resistive bolometer bridge. However, since the wet-etching is isotropic and the gold is being laterally exposed to the acid solution, an underetch is present of about 0.2 microns in all directions (not shown on figure), increasing the effective length of the device to an approximate additional $0.4\mu m$ (hard to estimate in the optical microscope). The device now looks as shown in figure 3.9:

The dimensions of this rectangle is not representing the final bolometer bridge: only the width of this rectangle widht defines *the length of the bolometer* (see figure 3.9). The large geometric length of the exposed YBCO rectangle will in the next process step be reduced to define the width of the bolometer. As will become clear, the reason to take

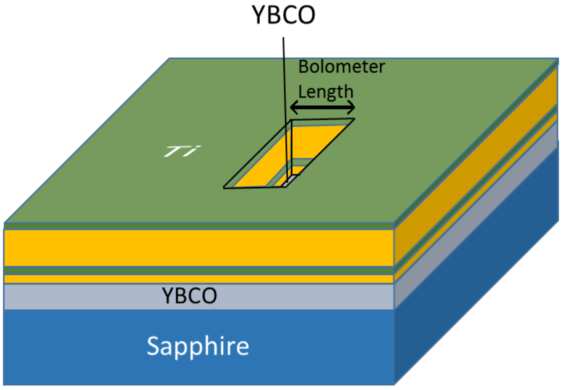

Figure 3.9: The exposed 20 nm gold is etched, and the window has YBCO is exposed.

it much larger is to allow an easier allignement in the next lithography.

3.4 Bolometer Width and Antenna Definition

The width of the bolometer and the spiral antenna are defined in the same step.

To achieve this, first a positive resist AZ1512HS is spun on top of the wafer.[3] After pattern transfer onto the resist, all parts that are not protected by the resist will be removed by Argon bombardment. It is hence important to position the mask properly so that after exposure and developing, the resist covers a part of the exposed YBCO window -the small YBCO rectangle not covered by any (highly conductive) metals defined in previous lithography-, as already mentioned it is that specific part that will act as the resistive (and hence heated) element of the bolometer. In order to obtain this precise positioning, allignment marks are used: those are situated both on the mask and on the wafer (the allignment marks on the wafer were defined along with the YBCO window in the first lithography). Some allignement flexibility is allowed in the direction along the rectangle width since the window is more elongated then the desired bolometric width. In the direction along the length of the bolometer very accurate allignement is necessary in order to respect the symmetrical design of the antenna (see figure 3.12).

Once the mask (figure 3.11) is properly alligned to the wafer underneath (when the allignement marks on wafer and mask overlap), light exposure is applied during 9 seconds. After 20 seconds develop time in AZ351B and water solution (AZ351B - water ratio = 1:5) and a water rinse, this results in the resist pattern depicted in figure 3.10.

Ion Etching Next the wafer is placed in the Oxford Ion Beam Milling System "Tool 417" . This machine applies Argon bombardment perpendicularly to the chip to remove everything that is not protected by the resist as depicted in figure 3.13. Ionized argon

---

[3] Spinning of HDMS layer and spinning of resist both at 4000 rpm, scratching the resist corners and applying the edge-bead procedure applies here as well. The resist being different, the softbake is performed at 100°C instead of 110°C and exposure time and developing time are 30 seconds instead of 60.

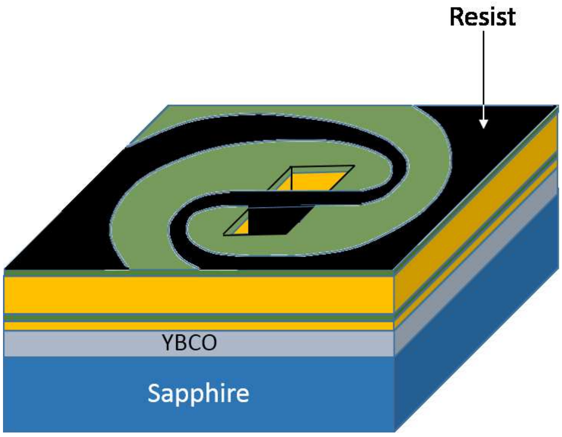

Figure 3.10: Resist patterned in order to define both the bolometer width and the antenna, the length of the device is determined by the width of the window (defined in previous lithographic step). The resist is shown in black and has a finite thickness around 1,3 μm in contrast to what the image suggests.

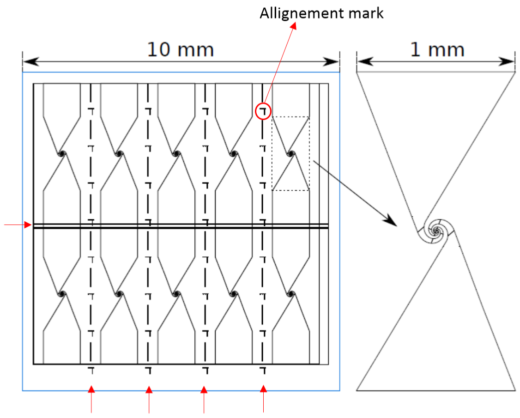

Figure 3.11: Mask used for lithography the second lithography, the external frame represents the total dimensions of the substrate ($10 * 10mm^2$). The allignement marks (the small L shapes, red circle) and dicing marks are shown (small red arrows). As was mentioned a total of 10 antenna integrated microbolometers are fabricated, each with a different length and width.

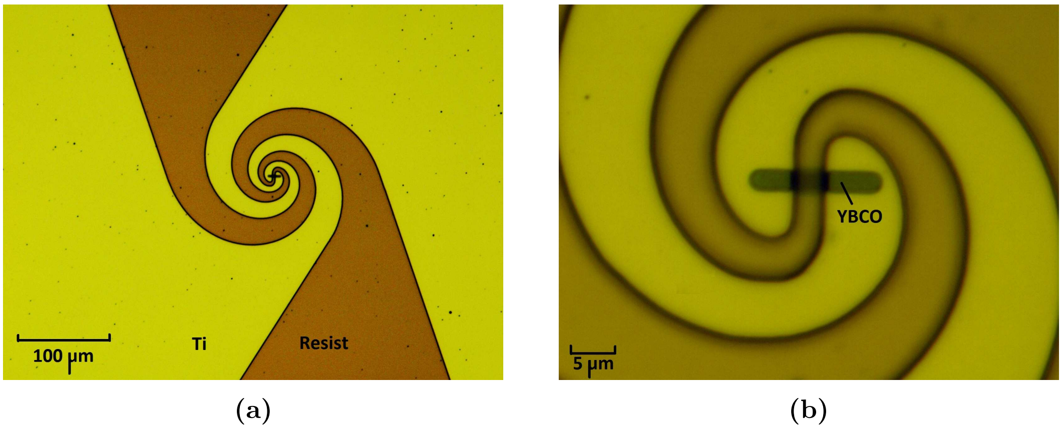

(a) (b)

Figure 3.12: (a)Optical microscopy image of the chip after resist patterning for the definition of bolometer width and antenna,(b)zoomed-in version of (a). The dark color is the deposited resist. This bolometer is well alligned in the vertical direction , but not so in the horizontal direction, but this does not affect the device performance. Note that the pictures are 90° rotated with respect to the schematic of figure 3.10.

atoms are accelerated in an electric field V so as to gain momentum, enabling them to knock out atoms from the surface of the exposed film once they reach it. The argon flow was set to $2sccm$, the acceleration voltage to 250 V and the ion beam current density to $0.2mA/cm^2$. The angle of incidence of the beam with respect to the substrate is 90°[4] so as to have straight etched sidewalls[5].

Considering that we want to remove all material stacked above the sapphire substrate, etching was performed for a total of 75 minutes since the etching rate under above mentioned conditions is 2-3 nm/min for YBCO , 1-2 nm/min for titanium and 11-12 nm/min for gold.[6]

A serious drawback of this etching method is excessive heating: Part of momentum transfer from the argon-ions is converted into heat dissipation of the lattice. YBCO starts to lose oxygen content already above 100° as reported by [32] leading to degradation in film quality.[7] For this reason water cooling is applied underneath the substrate on which the film is lying. Additionally, after each 5 minutes of etching a shutter covers the wafer from the Argon-ion beam for 5 minutes.

---

[4] This corresponds, for the tool parameter, to an inclination angle of 0° of the substrate.

[5] The sidewalls of the etched material do have a slope even under perpendicular beam exposure according to what is reported in [32], for YBCO this slope is about 30°.

[6] We did not measure the etch-rate of this layer. Although the CeO2 is non conducting, removing it was unnecessary.

[7] The lithography steps could affect YBCO quality as well, since the baking of the different resists, although only for a short duration, occurs at 100 and 125 degrees

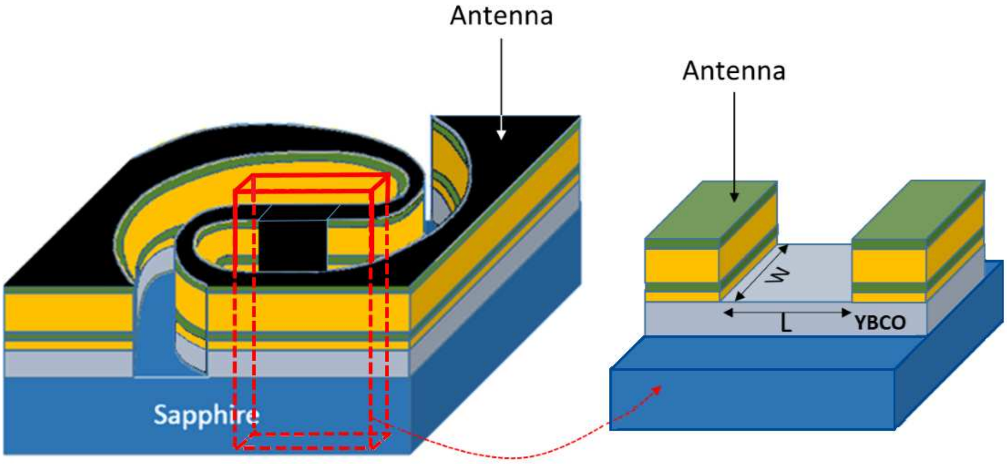

Figure 3.13: The final structure after ion milling. The resist remains present on top of the YBCO contrary to what is shown on the right figure.

3.5 Dicing

The last fabrication step consists of separating all ten bolometers using a dicing blade. This was done using a dicing diamond saw (Tool 1008). Since sapphire is a very hard material, careful selection of the blade was required and to achieve a single cut, two cuts on different depths had to be performed. The blade was manually displaced before each cut, and oriented by using the dicing marks provided on the chip (figure 3.11). Also important to note is that during dicing a lot of dust is produced, this originates from the substrate (as well as, in negligible amounts, from the blade itself which is loosing material). In order to protect the bolometers, a resist coating was spun onto the chip beforehand, and during the dicing itself water is continuously removing the particles. To avoid heating of the substrate due to the cutting, another jet of water is specifically directed onto the blade. After dicing,there is no need to remove the remaining resist (both the one which was spun before ion-milling as well as the one before the dicing), the contact pads are scratched using a scalpel, also the RF-measurements will not be affected by this resist since backside illumination is applied.

4

Measurement setups

After fabrication the bolometers were characterized using three different types of measurements: DC-power versus resistance, resistance-temperature and voltage response versus modulation frequency or IF Power versus IF frequency depending on the frequency range. The first two only requires DC sources, while the other one requires an extensive RF setup.

4.1 DC measurements

4.1.1 Power-Resistance measurement

By definition, the thermal conductance G is equal to $\frac{dP}{dT}$. Neglecting the electrothermal feedback (this hypothesis is verified once measurements are done), equation (2.7) simplifies to:

$$R_v = \frac{i\frac{dR}{dT}}{\frac{dP}{dT}} = i\frac{dR}{dP} \tag{4.1}$$

By measuring the current-voltage characteristic (V-I), both R (R=U/I) and P (P=U*I) are obtained. Then, from the slope of R(P), $\frac{dR}{dP}$ is calculated.

The setup is simple and is shown in figure 4.1. The voltage is applied by placing probes on the contact pads. Care should be taken to increase the voltage slowly so as to be able to have enough sampling points. Also shunt diodes (not shown) are used to minimize risks of damaging the devices during the measurement, these will short circuit the bolometers if the (undesired) voltage peaks are generated above a certain threshold. Hence it is important not to increase the voltage supply above that threshold to avoid having an IV curve which does not reflect the bolometer properties.

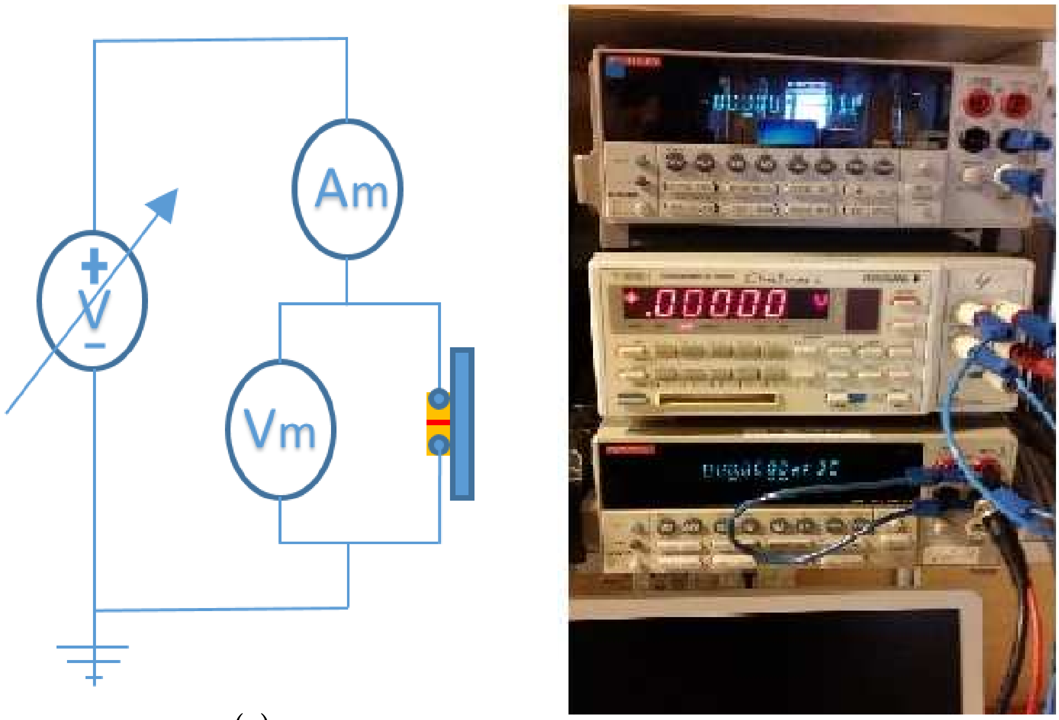

(a)

(b)

Figure 4.1: (a)Schematic picture of the power-resistance measurement, the contact pads for the DC connections are on the extension of the antenna. (b) Instruments used, Keithley multimeter and Yokogawa 7651 programable DC source (middle).

4.1.2 Resistance-Temperature Measurement

Setup. In order to extract the value of the other physical parameters, the thermal conductance and the time constant, it is required to measure how the resistance changes with temperature. Indeed:

$$G \equiv \frac{dP}{dT} = \frac{dP}{dR}\frac{dR}{dT}. \tag{4.2}$$

The first term $\frac{dP}{dR}$ is obtained in previous section, to obtain the $\frac{dR}{dT}$, a current bias of $500\mu A$ is applied, and the resistance is measured while the device is being cooled down. A priori, since we are interested in room temperature operation, only a temperature range of a few kelvin is required to measure the thermal dependence. However since the bolometers are made of YBCO, it is interesting to measure the superconducting transition properties so get an idea of the material quality.[1] For the superconducting transition to occur cooling below 77 K is required, hence the interest of using liquid helium. The bolometer was placed between two electrodes on the edge of a long stick, which was then

---

[1] The bolometer superconducting transition is compared to the transition of the complete film prior to the fabrication.

lowered into a bath of liquid helium. A thermometer close to the bolometer continuously measures the bolometer temperature, while the resistance was measured with a simple two-probe measurement. A schematic picture can be seen in figure 4.2. The inside of the tube is not in direct contact with the helium bath, this would lead to a very slow cooling because of the mismatch in thermal conduction. Hence the tube is filled with helium gas as well.

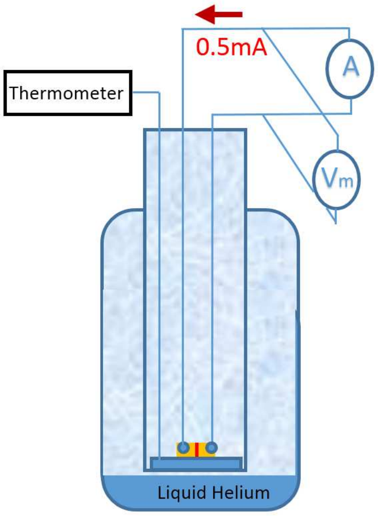

Figure 4.2: The experimental setup used for the characterization of the bolometer resistance as a function of temperature. The temperature is regulated by lowering the holder into the dewar.

4.2 RF measurements

As discussed in Chapter 2, gain bandwidth measurement allows to extract the relevant physical parameters. From previous experiments with these type of bolometers, as well as from predictions from the DC-measurements, it is known that the range of interest is between $10Hz$ and $15GHz$. In order to obtain the responsivity over this wide frequency range, due to the limitations of the available equipment, there is a need to rely requires to use two different measurements setups instead of one: For the frequencies between $10Hz$ to $100kHz$, the bolometer is operated as a direct detector. For the frequencies between $100kHz$ to $15GHz$, the bolometer is operated as a mixer.

4.2.1 Measurement setup $10Hz$ to $100kHz$, direct detection

To obtain the response versus frequency, we apply amplitude modulation as explained in the section on direct detection (section 5.2.1). A power P at frequency ω needs to be applied to the bolometer and corresponding voltage V is read:

$$R_v(\omega) = \frac{V(\omega)}{P(\omega)}$$

If the power $P(\omega)$ is kept constant when the frequency is varied, the read-out voltage will be proportional to the responsivity. Since we are only interested in the relative variations of R_v versus frequency, the absolute value of the power does not need to be known.

The quasi-optical setup requires a sufficiently high carrier frequency. Simultaneously these frequencies should low enough such that they can be generated by the available tools. The frequency generator,Agilent technologies, E8257D PSG Analog Signal generator,reaching a maximum frequency of 20 GHz, combined with a frequency multiplier, OML E8257 DS 10, with a multiplication factor of 6, can meet this requirement: 80 GHz as carrier frequency was used.

Summarized, an amplitude modulated signal with a fixed carrier frequency of $80GHz$ is generated where the modulation frequency f_{AM} is varied from $10Hz$ to $100kHz$ in discrete steps, with a modulation depth of 50%:

$$y(t) = \left(1 + 0.5\cos(2\pi f_{AM}\Big|_{10Hz \to 100\text{kHz}} t + \phi)\right) E\sin(2\pi 80\text{GHz } t)$$

The amplitude E of the signal is unknown, but is set to the maximal possible value on the source generator in order to achieve the highest voltage response. This signal is send over the air using a 3.6 mm diagonal horn antenna with a directivity of 26 dB and captured by a lens which focuses the signal on the bolometers log-spiral antenna. The beam waist of the horn antenna and the detector (on the 5 mm silicon lens) are hence placed about 5 mm from each other in order to achieve a high coupling efficiency.[2]

DC BIASING: A voltage source with a $10k\Omega$ resistance in series with it creates a constant current source.[3] As can be seen from equation 2.7, the higher the current, the higher the the response. A bias of $500\mu A$ is applied during all measurements (for both setups discussed), since it is high enough to observe the response with the the available equipment.

The bolometer will produce a voltage response at the modulation frequency ω_{AM}.[4] The response is recorded using a Stanford research system, SR830 DSP lock-in amplifier. This type of amplifier has an internal reference source used for the detection of the AM

---

[2] Although we are not interested in the absolute values of responsivity, it is interesting to note some important losses in the setup. The spiral antenna is circularly polarized in contrast to the incoming beam emitted by the horn antenna which is linearly polarized, this leads to an estimated 0.5 coupling loss. Also the lens air interface has a transmission coefficient of 0.7. These values were taken from [39].

[3] The bolometer has a typical resistance between 50 and 100 Ohms and is placed in series the $10k\Omega$, hence the assumption of an ideal current source is valid. During noise measurements in the group, additional noise appeared when using a current stabilized source, possibly attributed to the current control feedback loop of the current source. This is the reason for the current biasing using a voltage source in series with a resistance although this is not a requirement here where we are interested in the IF response which lies well above the noise flour.

[4] A response is also present at $80GHz$. However this response is much weaker since this frequency is much higher than ${\tau_{ep}}^{-1}$, only the electron subsystem is able to translate these power oscillations in thermal oscillations. In any case this is undetectable by the lock-in amplifier.

signal. The internal reference is synchronized with the generator by a connection of the generator to the lock-in amplifier.

The voltage read out on the lock-in is given by:

$$V_{lock-in}\Big|_{\omega_{AM}} = \frac{1}{2\sqrt{2}}0.5 * (0.5E^2)R_v(\omega_{AM})$$

,where the factor $\frac{1}{2\sqrt{2}}$ is present because the lock-in read out gives the root mean square value of the peak to peak amplitude of the signal, and the definition of the responsivity, equation (2.6), assumes the half-width voltage. Standing wave phenomena between the horn and the bolometer detector block makes that the response varies as a function of the position of the bolometer. This is the reason that the bolometer (together with the lens) is mounted on an adaptable table where screws that can shift the device in the 3 spatial directions so as to maximize the incoming power. Once a maximum is found, the modulation frequency can now be varied and at each of the steps the bolometer response at the corresponding modulation frequency is recorded by the lock-in amplifier. The setup scheme is found in figure 4.3.

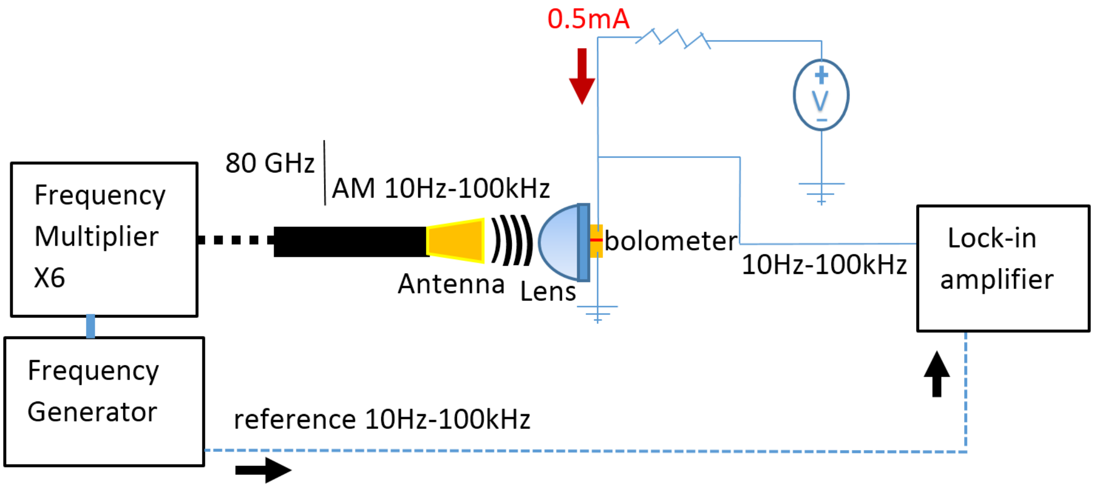

Figure 4.3: Schematic picture of the experiment setup for the bandwidth measurement $10Hz$ to $100kHz$. Signal emitted at carrier frequency of 80 GHz, and the AM modulation varied after readout on lock-in. A signal with frequency equal to the AM frequency signal is being sent from the signal generator as a reference signal to the lock-in through a seperate cable (dotted lines).

4.2.2 Measurement setup $100kHz$ to $15GHz$, heterodyne detection

To obtain the frequency response for higher frequencies a different setup is required (figure 4.4). Indeed, the lock-in amplifier used in previous measurement setup is not able to go above $100kHz$. The spectrum analyzer will be used instead. The lock-in amplifier is however still used but for a different purpose, i.e. to compensate for frequency dependent fluctuations in the incident power as will be explained later on. The main limitation of the previous setup however is the inability of the frequency generator to produce a reliable amplitude modulation above $100kHz$. This new setup avoids this particular issue by exploiting the mixing property of the bolometer.

In this setup we will apply two incoming signals at frequency ω_{LO} and ω_{RF}, the mixer produces a voltage as was deduced in previous section (2.11):

$$V(\omega_{IF},t) = R_v(\omega_{IF})2\sqrt{P_{LO}P_{RF}}\cos(\omega_{IF}t) \tag{4.3}$$

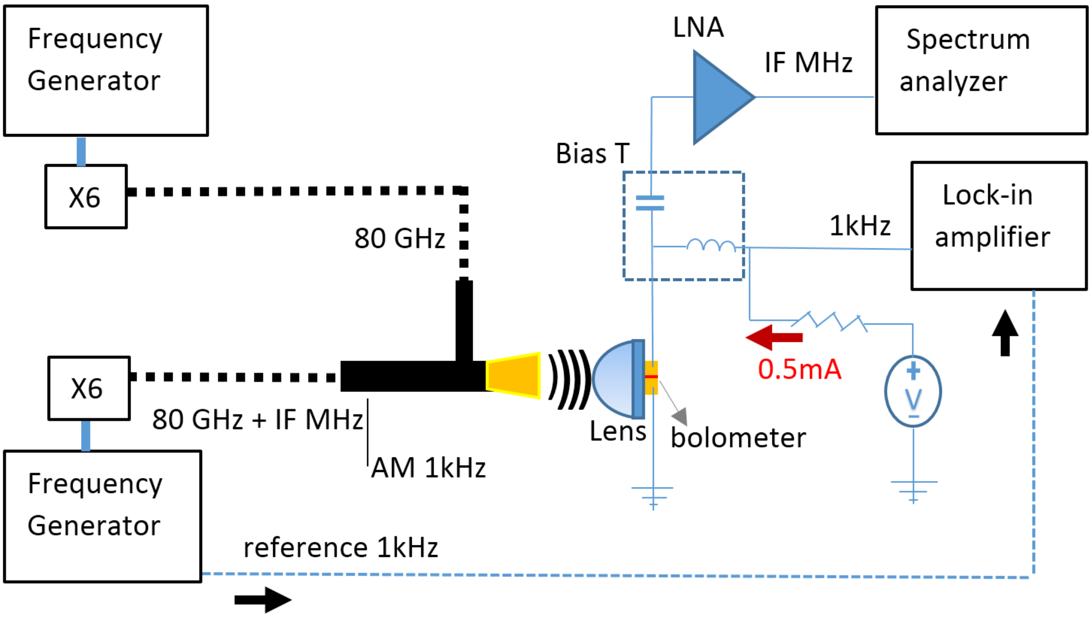

Figure 4.4: Schematic picture of the experiment setup for the bandwidth measurements for Intermediate Frequency (IF) from $100kHz$ to $15GHz$. The two LNA amplifiers (represented by the single triangle on the figure), are added for IF between 70 MHz and 15 GHz.

Signal emission: As was explained in Chapter 2, two sources are needed for mixer operation, one source responsible for the generation of the LO signal, the other for the RF signal. The frequency generators (Agilent technologies, E8247c, PSG CW signal generator and Agilent technologies,E8257D PSG Analog Signal generator) can generate signals up to 20 GHz. This maximum frequency is not high enough for the quasi-optical detection setup (as was already mentioned for previous setup). Hence the respective signal from each frequency generator goes through a SMA cable into a frequency

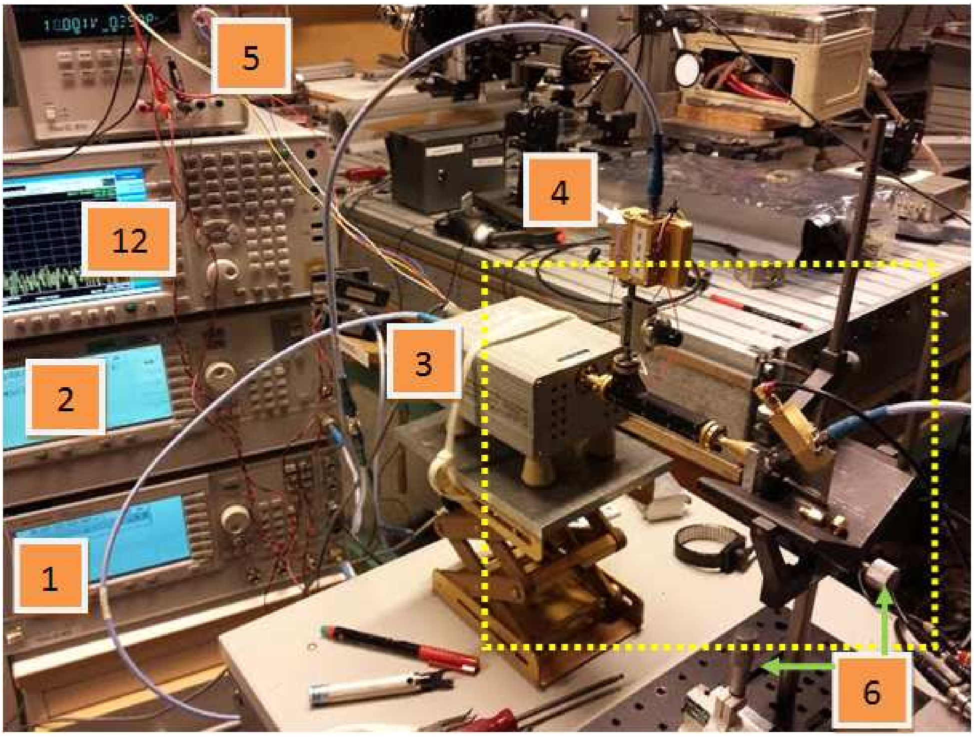

Figure 4.5: Experimental setup for the bandwidth measurement, for Intermediate Frequency (IF) from $100kHz$ to $15GHz$. Legend: 1-2 Frequency generators, 3-4: frequency multipliers, 5: voltage source for the LNA amplifiers, 6: screws to adjust the measurement setup, 12: Spectrum analyzer. LNAs visible on the upper left of the number 3 square. Missing numbers: see zoom in on figure 4.6.

multiplier, OML E8257 DS 10 and Omnisys Instrument frequency multiplier, with the multiplication-factor of both being 6, enough to reach final frequencies of 80 and 95 GHz. In order to obtain the responsivity over the desired frequency range of the IF frequency, $100kHz$ to $15GHz$, the LO oscillator generator is kept fixed at 80 GHz and the RF-generator is being varied from $80.0001GHz$ to $95GHz$.[5] After this the signals are combined in a waveguide using a directional coupler (Flann microwave instruments). This single waveguide is followed up by the horn antenna emitting the combined signal to detector block. A schematic picture of the setup is shown in figure 4.4, and one of the actual setup is shown in figure 4.5 and4.6.

Signal detection: Similar to the first setup the signals coming from the antenna, are going into the detector block: signals are focused by the lens onto the spiral antenna which further brings the radiation to the bolometer.

Since the bolometer works as a mixer, the bolometer will generate a signal at the intermediate frequency $|\omega_{LO} - \omega_{RF}|$. The bolometer is supplied with a constant bias

---

[5] In this setup, it is clear that either source can be interpreted as being the LO or RF source. We will take here the convention that the RF signal is designated as varied signal.

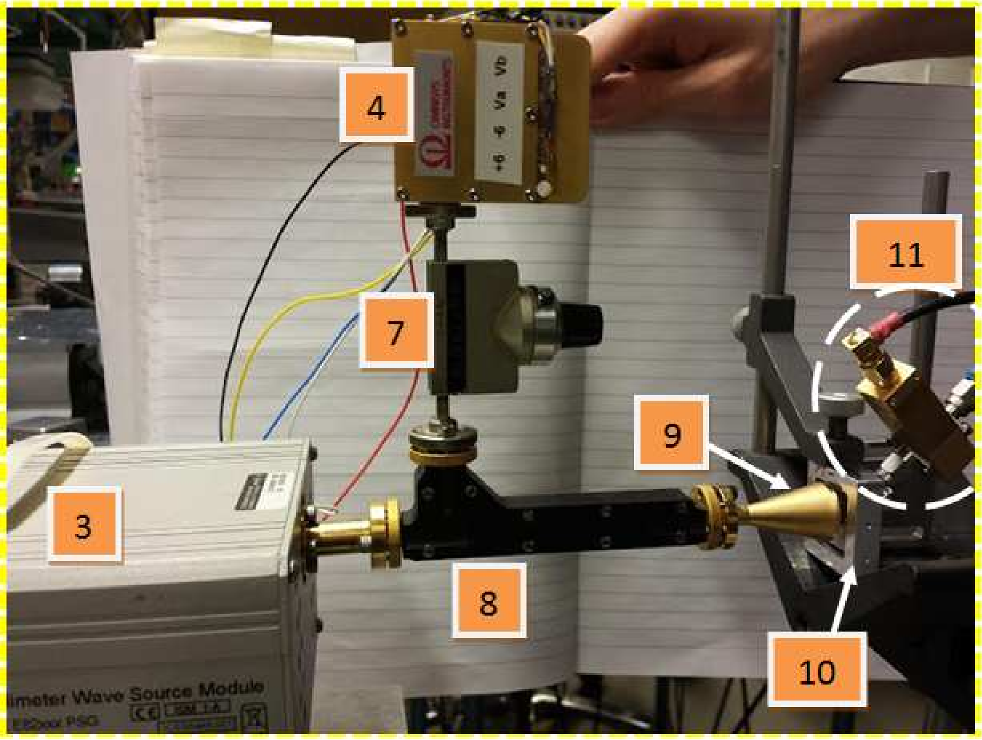

Figure 4.6: Picture of the experimental setup for the bandwidth measurements . Legend: 3-4 Frequency multipliers, 7: Tuner to tune the amplitude of the local oscillator signal, 8: directional coupler/waveguide, 9 horn antenna, 10: lens and bolometer, 11: bias T.

current of $500\mu A$. Simultaneously the IF signal, our signal of interest, has to be separated from the DC signal and read out subsequently. This is done by a so called 'bias T' , a three terminal device where one port is the combined IF and DC signals, one output has a capacitor letting the IF signal through and blocking signals with frequencies between 0Hz to 3 kHz so as to protect the ac measurement instruments from DC currents, and the third port contains an inductance, allowing the DC signal to bias the bolometer and simultaneously blocking ac signals from 40 kHz to 40 GHz, as to avoid a loss of IF signal.

The AC signal, separated from the DC-bias by the bias T, is led to a spectrum analyzer: either Agilent technologies, PXA Signal analyzer 3Hz-28.5GHz N9030A or Rhode and Schwarz FSUP Signal source analyzer 20Hz-50GHz, depending on the availability of the instruments on the day of measurement. This frequency analyzer will give the power contained at each frequency of the incoming signal, that is the information we desire: the amplitude of one peak situated at $|\omega_{LO} - \omega_{RF}|$.[6]

The bolometer response starts to roll off at IF around 1MHz, at 100MHz the signal is typically 20 dBm weaker than at 1MHz, at 1GHz up to 50 dBm weaker, hence the signal

---

[6] Video bandwidth and Resolution bandwidth for the Agilent analyzer is set to 75Hz and 12Hz respectively. For the Rhode and Schwarz: 100Hz and 50Hz.

can start to drop below the noise floor of the spectrum analyzer (-130 dBm). Hence, either the incoming power must be increased, but is discarded since it is already at the maximal value. The other option is to amplify the detected signal using microwave low noise amplifiers (LNA) : two myteq 0.1GHz-20GHz amplifiers are used, having a total of 42 dB gain and 50Ω input impedance, but raising the noise floor to (-110 dBm), so the signal to noise ratio is improved by 20dBm, enough to record the response of the devices up to 15 GHz. These amplifiers are added to detect the IF signal, between 70 MHz and 15 GHz (figure 4.4).

Monitoring of power variation of the RF source during the frequency sweep: The voltage read-out will be representative of the sensitivity over the whole frequency range only if the incoming power incident onto the bolometer is frequency independent, as seen by the mixer equation (equation (4.3)). This is however not the case: To obtain the desired bolometric response over the frequency range from $100kHz$ to $15GHz$, the RF source is varied from $80{,}0001GHz$ to $95GHz$, resulting in a different interference pattern between horn-antenna and the detector block as a function of frequency.[7] The detector, being held in a fixed position, will produce a lock-in read-out different from the intrinsic response at that given frequency. Hence, this should be rewritten as:

$$\parallel V(\omega_{IF},t) \parallel \propto R_v(\omega_{IF})\sqrt{P_{RF}(\omega_{IF})} \tag{4.4}$$

The RF-power or at least the way it varies with frequency has to be estimated. This is done by amplitude modulating the varying frequency source,the RF signal, and reading the response at the chosen AM frequency using a lock-in amplifier (the same lock-in amplifier as for the low frequency measurements). This lock-in readout is effectuated at each point of the frequency sweep and is used to take into account the power loss when reading the signal amplitude on the frequency analyzer. The AM-frequency was chosen at $1kHz$ allowing this signal to go through the DC port of the bias T.

Mathematically, we can derive the mixer behavior with an amplitude modulated signal by substituting in the incident power expression, equation (2.9) of E_{RF} by $E_{RF}(1+M\cos(\omega_{AM}t+\phi))$. The short proof is found in appendix, the final expression after this substitution gives:

$$\begin{aligned} P_{dissipated} = P_{LO} + P_{RF} + \mathbf{P_{RF}M}\cos(\omega_{\mathbf{AM}}\mathbf{t}+\phi) + M^2\cos(2*(\omega_{AM}t+\phi)) \\ + 2\sqrt{P_{LO}P_{RF}}\cos(\omega_{IF}t) \\ + 1\sqrt{P_{LO}P_{RF}}\cos((\omega_{IF}+\omega_{AM})t+\phi)) + 1\sqrt{P_{LO}P_{RF}}\cos((\omega_{IF}-\omega_{AM})t-\phi)) \end{aligned} \tag{4.5}$$

From this equation it is deduced that the lock-in amplifier locked in on the AM frequency will produce a voltage proportional to the incident RF-power:

---

[7] The antenna emission itself and interferences inside the directional coupler as well lead to varying RF-power, however those contributions are negligible. The generators and the multipliers have a flat response over the whole frequency range.

$$V_{lock-in}\Big|_{\omega_{AM}} = \frac{1}{2\sqrt{2}} R_v(\omega_{AM}) M \mathbf{P_{RF}}$$

We decided to normalize the AM lock-in response with respect to the AM lock-in response when the RF signal is at 80,1GHz.[8]

Since

$$P_{RF}(\omega_{RF}) = P_{RF}(\omega_{RF=80,1GHz}) \frac{V_{lock-in}\big|_{\omega_{AM}}(\omega_{RF})}{V_{lock-in}\big|_{\omega_{AM}}(\omega_{RF=80,1GHz})}$$

,the correction applied to the measured IF voltage will be, using equation (4.4):

$$\parallel V_{IFcorr} \parallel = \frac{\parallel V_{IFmeas} \parallel}{\sqrt{\frac{V_{lock-in}\big|_{\omega_{AM}}(\omega_{RF})}{V_{lock-in}\big|_{\omega_{AM}}(\omega_{RF=80,1GHz})}}}$$

The spectrum analyzer does not indicate the voltage response but gives the intermediate frequency power as was already defined in chapter 2, $P_{IF}(\omega) = \left\langle V_{IF}^2(\omega,t) \right\rangle / 4R_L$, expressed in units of dBm, note that this assumes a lossless transmission line with matched impedance, which is not entirely the case (R_L the load is fixed at 50Ω which the detector seldom matches to). Since we are not interested in the absolute response values but only the behavior as function of frequency this is not a problem.

Side remark: When the signal on the spectrum analyzer is read out it is necessary to switch off the amplitude modulation. As seen in previous equation (A.3) the AM modulation causes harmonics to appear around the IF frequency with a spacing equal to whole multiples of the AM frequency. These peaks are lower in amplitudes than the one at the IF, and it is possible that the computer takes one of those as a sample point instead. Also, part of the power is redistributed on these other frequencies, making the effective amplitude at the IF lower as without AM-modulation.[9]

Side remark: In principle it does not matter which source is used as local oscillator source and which one as RF source. However it is clear that the one whose frequency is being varied should be the one with amplitude modulation. Also only the frequency generator Agilent technologies,E8257D PSG Analog Signal generator, is able to apply modulation.

Compensation of the transmission line after the detector block: The cables after the detector block where the IF is generated, the bias T, the LNA (when used) and the spectrum analyzer do not have a flat response over the whole frequency range. Hence their transfer function needs to be evaluated, this is experimentally done by simply effectuating a sweep over the IF frequency range (i.e. from 100kHz to 15 GHz) onto the bias T entrance (removing the detector block) and measuring the response on

---

[8] This normalization is strictly speaking not necessary since, as already mentioned, we are not interested in the absolute value of the responsivity

[9] All the readout is done via LabView on a desktop computer through GPIB port connections. LabView also applies to appropriate control signals to each measurement device (for instance to switch off AM modulation prior to readout on spectrum analyzer).

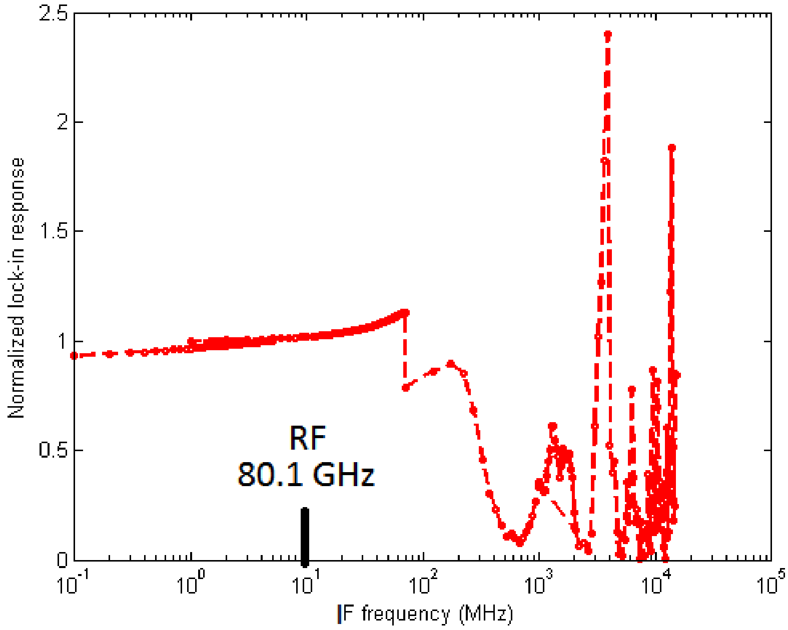

Figure 4.7: Lock-in response normalized to the lock-in response as a function of the intermediate frequency. The lock-in response is normalized with respect to its value when the RF source is at 80.1 GHz. The standing waves become more apparent when the wavelength starts to be comparable in dimensions to the distance between antenna and detector, as expected.

the frequency analyzer. Although not mentioned before, a similar measure was taken for the other setup (from 20 Hz to 100kHz).

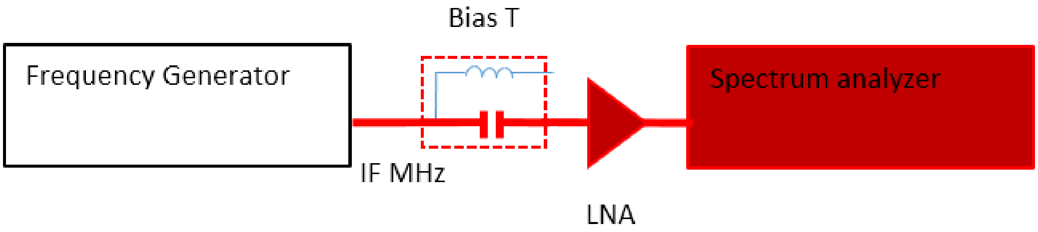

Figure 4.8: Setup used to evaluated the transfer function of the IF line.

To conclude, the setup discussed here can not be used to obtain the band 10 Hz-100 kHz because the frequency generators are not able to produce 'carrier' frequencies with a precision below 100 kHz (e.g. $f_{RF} = 80GHz + 10kHz$ can not be generated), limiting the lowest possible IF frequency to that same value. We again note that in the frame of this research it is the relative variations of IF power with respect to frequency that is of

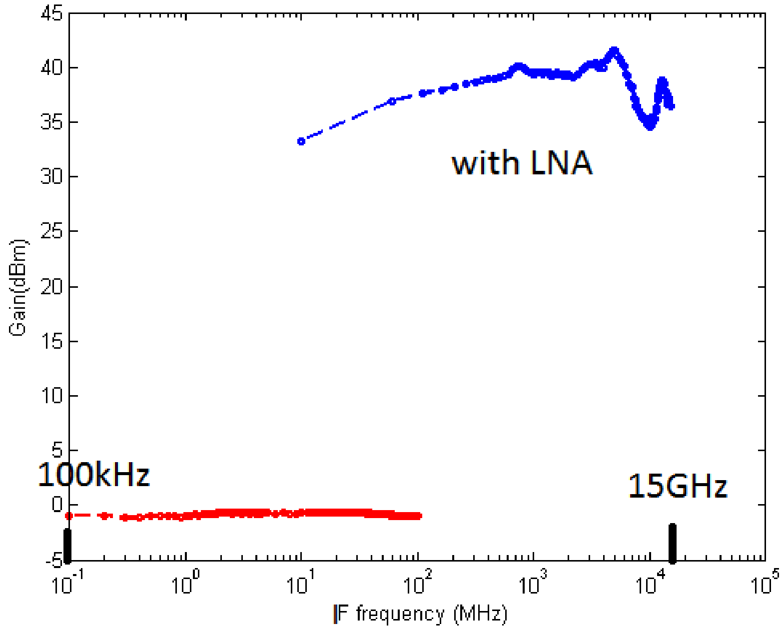

Figure 4.9: Transfer function of the IF line, evaluated by the setup shown if figure 4.8, using the Rhode and Schwartz spectrum analyzer. Red curve is for the response between 100 kHz and 100 MHz were the LNA was not present in contrast to the blue curve taken between 10MHz and 15 GHz. We can deduce that gain of the LNA is approximately40 dBm. At higher frequencies, the response is not so flat, this is due to interference effects inside the transmission line.

interest, the absolute values are not of interest. [10] AM-modulation was used not as the detection signal of interest but as a calibration tool to compensate for carrier-frequency dependent losses, the modulation frequency was hence kept constant.

---

[10] In order obtain absolute values of the responsivity, the incident powers on the bolometer have to be known, this would require to estimate the losses (mainly reflection losses on the air-lens interface and polarization losses).

5

Results and discussion

This chapter outlines the results obtained from the DC and RF measurements. These results are discussed and also briefly compared with the two-temperature model that was introduced in chapter 1. No reproducible results are obtained inside a batch and across the different batches so we show the data of all measurements, both DC and RF, for each batch consecutively. The chapter ends by summarizing and further commenting the observations made (supported by additional summarizing graphs), together with some suggestions for future work.

5.1 Films

After PLD deposition and prior to the lithography the films are as depicted in figure 3.2. For each, the resistance versus temperature is measured, in the range where transition to superconducting state occurs.[1] This allows to give have an idea of the film quality. The higher the transition temperature Tc and the less broad the range of temperature over which transition to zero resistivity takes place the better.[2] Typically high quality YBCO possesses a Tc of 88 K and transition width of 0.5K. The film quality is very sensitive to the deposition conditions as was already mentioned previously, measuring the Tc a one way to characterize the quality, even though it is a priory not clear wether this parameter has any effect on the thermal properties (we are specifically how the phonons will be scattered at the interface between film and substrate). Deposition temperature and buffer-layer-thickness are the two parameters that have been varied in this work. Figure 5.1 shows the result of these measurements.

---

[1] This requires cooling in liquid helium or liquid nitrogen, the experimental setup is almost same as the one used for individual bolometers described in figure 4.2 where instead of a 2-probe measurement, a 4-probe measurement is used

[2] The Tc coresponds to the point of highest slope and the transition width at 90% of the resistance values at the point where the change in slope occurs.

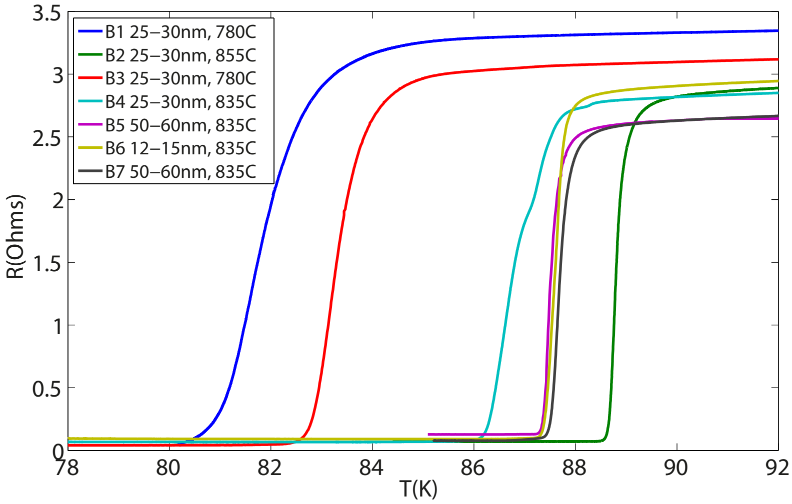

Figure 5.1: Resistance as a function of the temperature for the different batches. The buffer thickness has no apparent influence. The higher the deposition temperature the higher the Tc, a trend that has been reported before. As a side remark, the values of the resistance is only a few ohms above the superconducting transition, this is because the film is coated with the thin layer of gold which has higher conductivity compared to the YBCO film underneath.

In the four first batches, from figure 5.1 it is seen that the temperature depositions of 780 degrees gives the worst result, 855 the best. We decided to keep the deposition temperature at $835°C$ and vary the thickness of the buffer layer. From the graph it is clear that the thickness of the buffer-layer has no influence on film quality regarding its superconducting transition features.

5.2 Batch-per-Batch Review

5.2.1 Batch 1, 25-30 nm, $780°C$

First a discussion on the dc measurements obtained is presented, following this the RF measurement for this batch is discussed and compared with the DC-results.

Only 3 devices could be characterized in this batch, all others showed extremely high resistance values, more than $10k\Omega$, an explanation for this might be that the devices are very sensitive to electrostatic discharges. Since the slope is constant over a large range of temperature and we are not fast enough to record the data immediately when the cooling is applied, we generally extrapolated the values at room temperature $(294K)$from the slope at around $260 - 280K$ of the RT curves, plotted below in figure 5.2. At low temperature, a change in slope that is most probably associated with superconducting transition, as was the case for the film prior to device fabrication, however the resistance in that case is expected to drop completely to zero but does not(figure 5.2). We do not know the cause of this. For later batches this identical problem was observed only in a one case, device 2 of batch 6 (figure 5.15). A possible explanation lies in a residual contact resistance, in series with the bolometer, while the device still goes into superconduction with effectively zero resistivity. But the physical origin of this series resistance can still not,in that case, be explained. The other possibility, being the YBCO itself and not some series resistance that explains the phenomena, is supported by observation in device 4 of batch 7, on figure 5.15 the first kink at $86K$ is followed by a second drop only at much lower temperatures -around 55K. Since we only cooled down till 60 K, a small experiment could consist of recording the whole temperature range and observe wether the zero resistivity occurs.

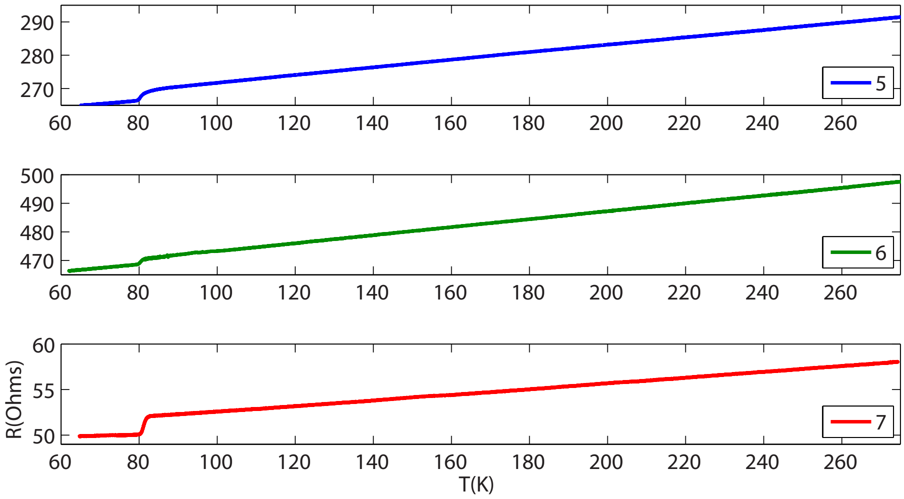

Figure 5.2: Resistance as a function of temperature for bolometers 5, 6 and 7 (different vertical axis values). A drop in resistance is observed in the three devices around 80K.

The resistivity of the device is obtained by measuring the resistance (at room temperature), $\rho = (R * l * w)/d$, l the bolometer length, w the width, d the thickness of the YBCO film, in all cases equal to 70 nm. Since this parameter is an intrinsic property of the material it should be constant for all devices , yet it is not in this case (table 5.1). An explanation might be a wrong estimation of the area. We use the dimensions on the lithographic masks for all calculations, and we verify under optical microscope, which has roughly estimated,a precision of half a micron. It turns out that the lengths are between $0.5\mu m$ and $0.75\mu m$ larger than the one on the mask although the width is very well respected.[3]This error can explain a possible offset in the values measured, but not scattering in data. The resistivity is also much higher than in the other batches and to what is reported by [18], the dimensions are estimated in exactly the same way and uses the same material and fabrication process (scattering is not mentioned). Defects in the YBCO film probably are probably at the origin of the scattering.

---

[3] The increase in length is probably due to the wet etching which creates an undercut in the gold-layer

bolometer number	Length (μm)	Width (μm)	R (Ω)	dR/dT ($10^{-2}\Omega/K$)	dP/dR ($\mu W/\Omega$)
5	1.5	2	294	8	40
6	1.5	1	500	11	18
7	1.5	4	58	3	228

bolometer number	ρ ($\mu\Omega cm$)	α ($10^{-3}/K$)	G ($\mu W/K$)	R_{bd} ($10^{-3}cm^2K/W$)	R_v at $1mA$ (V/W)	τ (ns)	$\boldsymbol{f_{DC}}$ (MHz)	$\boldsymbol{f_{RF}}$ (MHz)
5	2740	0.4	4.5	6.8	25.0	120	**1.3**	×
6	5250	0.3	2.5	5.9	56.2	110	**1.5**	**0.4**
7	1640	0.5	7.2	5.6	4.4	100	**1.6**	**1.1**

Table 5.1: Summary for batch 1. The upper table contains the information directly obtained from the measurements (all obtained at 295 K), the lower table gives the relevant physical parameters extracted from these. f_{DC} and f_{RF}, in bold, correspond respectively to the 3dB cut-off frequency that is calculated from the DC-measurements and the actual 3dB roll-off taken from the RF-measurements using a lorentzian fit.

The value of $\frac{dR}{dT}$ is in accordance to what is reported by [18]. However the resistances of device number 5 and 6 are higher than those reported by that same paper, this makes the temperature coefficient of resistance,TCR, $\alpha = \frac{1}{R}\frac{dR}{dT}$, another intrinsic material property, lower than what is reported by [18] ($0.5.10^{-3}/K$ instead of $2.10^{-3}/K$) (a comparison with the other batches, see figure 5.26). Contrary to resistivity where dimensions are estimated, the TCR is deduced using nothing but electrical measurements. It is noticeable that the lower the TCR the higher the resistivity. These low values for the TCR indicate that the film quality is low, this is as well reflected from the low Tc (around $80K$) for all devices and film. It was hence interesting to plot the relation TCR versus Tc for the devices in all batches: the result is that there is no general correlation present, but a high Tc is a necessary condition to have a high TCR.

From the $\frac{dP}{dR}$, as was shown in equation (4.1) the responsivity of the device is directly obtained.[4] The smaller the bolometer area, the higher the responsivity, as is expected (see chapter 2). However the response, for a given area, is one order of magnitude higher than what was previously reported by the same paper [18] as well as what is measured on the next batches.

The responsivity being higher and the $\frac{dR}{dT}$ being the same as in [18], this means that, using equation (4.2), the thermal conductance G is an order of magnitude lower than what is found in that same paper. Somehow the bolometer is more isolated from the environment. The thermal boundary resistance is calculated by dividing the thermal conductance by the area[5], equation(2.13). We note that to extract the thermal

---

[4] It can be verified that the electrothermal feedback can be neglected. The worst case values used in this work, for a current of $1mA$, $\frac{dR}{dT} = 1.10^{-2}\Omega/K$ $I^2\frac{dR}{dT}$ is 100 times smaller than $G = 1\mu W/K$

boundary resistance this assumes that the principal path of heat removal is through the substrate $G \simeq G_{substrate}$. Values of the thermal boundary resistance are almost equal in each case. This is expected since this parameter is independent of geometry and solely determined by the materials interface, also the scaling of G with the area confirms the above mentioned assumption. It is however not observed in all batches (figure 5.28).

Higher thermal boundary resistance, although beneficial for the responsivity, will lead to slower devices. The time response found in the table is calculated using the definition in equation (2.15), dividing the thermal capacity C by the thermal conductance G or equivalently using $d.c.R_{bd}$ where the thickness d is $70nm$, R_{bd} given in the table, and the specific heat capacity c equal to $254.10^4[J/(m^3.K)]$. The corresponding frequency roll-off is calculated in the next-to-last column as $\frac{1}{2\pi\tau}$ and is, not surprisingly anymore, an order of magnitude lower than what is previously measured in paper [18]. Also compared to the other batches, as seen in figures 5.23, the thermal boundary resistance is higher (and corresponding roll-off frequency lower) in this first batch.

The RF measurements, from $100kHz$ to $15GHz$ intermediate frequency, were performed on device 6 and 7, device 5 was 'killed' during measurement. The result is shown in figure 5.3. A first observation is that for device 7 the IF power is higher than for device 6 although the DC-responsivity is lower. This is not necessarily in contradiction with the DC measurements: incident power for both bolometers is not necessarily the same. Each time a device is measured, it is required to align the bolometer: by visual adjustment the bolometer is aligned with respect to the lens, once this done, the whole detector block is aligned with respect to the horn antenna by adjusting the position until maximal response is obtained on the lock-in amplifier. This alignment is hence not very rigorous and can thus easily defer from one device to another. Since this contradiction is present in other batches as well, we will hence not make any further comparisons in that respect.

The second and most important observation, relates to the shape of the curves. The shape of both curves are very different, between $600kHz$ and $5MHz$ device 6 has a distinctly higher slope than device 7, device 6 shows a flat response between 6 and $40MHz$ (black ellipse on the figure), and then rolls off again whereas device 7 rolls of continuously. Also in that same range, after $40MHz$ the slopes are identical.

The simple model derived in section (or the two-temperature model) states the response is flat at low frequencies and starts to roll-off with a slope of 20 dB (or dBm) per decade. We decided to make a lorentzian fit of equation (2.7) using the least square method, this allows to extract the characteristic time constant τ. The equation shows that $\frac{1}{2\pi\tau}$ is the frequency at which the signal is 3 dB lower than at zero frequency, so that an estimation of this parameter can be made directly on the graph. The model fits very well for device 6, whereas for device 7 there is a significant deviation.

The time constant of the RF measurements and from the DC-measurements can be compared. The characteristic roll-off frequency from the fitted curve ($\frac{1}{2\pi\tau}$) is placed in

---

[5] As was already mentioned the thermal boundary resistance is extracted using the area that is present on the mask, with exception of batch 3 where the dimensions had to be reevaluated by optical microscope due to the fabrication error.

the last column of the table for the DC measurements (referred to as f_{RF}), and the one of the DC measurements (referred to as f_{RF}) is placed as well on the RF-curve (black arrows). For device 7 the time constants match (we note though that the fit for device 7 is not perfect), but not for device 6. In later batches, this match is far from being the case (with the exception of batch 3).

We further proceed with the analysis of the RF-measurements at higher frequency. As already mentioned device 6 shows a flat response between 6 and $40MHz$, assuming that the first plateau is associated with the phonon escape time, this plateau (black ellipse on figure) can not be associated with the hot electron response since the frequencies are far too low (occurring most often above $1GHZ$ as seen in other batches (figure 5.29) and literature, for instance in [55]), furthermore starting at $10GHz$ there seems to be the onset of such a plateau (although the picture is quite noisy somehow). The observed behavior is unexplainable by the two-temperature model as described in section 2.4). The lowest frequency shelf could be associated with another thermal phenomena and then we could attribute the second one to the thermal boundary resistance (in that case -for this batch- this would give a low value for the thermal boundary resistance in contradiction with the thermal boundary resistance extracted from the DC measurements, at least in this batch). In literature (e.g. [17], [31], [56]) heat diffusion *in* the substrate is mentioned to be responsible for a low frequency slope. However a simulation shows that heat diffusion in sapphire, having a very high thermal conductivity and thermal capacity, only contributes to a very minor frequency dependence (see section 2.4, 2.6). Device 7 rolls of continuously and the onset of a plateau at $4GHz$ seems to be present for device 7 (dashed black ellipse on the figure).

In summary, from the DC measurements, on the three devices that were measured, the device properties deviate from previous reported values as well as on the other batches that were measured, but apart from the resistivity which scatters a lot and a resistance which shows a drop without reaching superconductivity, the DC-results inside this first batch are consistent. The thermal boundary resistance extracted from the DC-measurements is exceptionally high. The RF-measurements show two devices with entirely different behavior. A very good match with the DC extracted time constant is found for device 7.

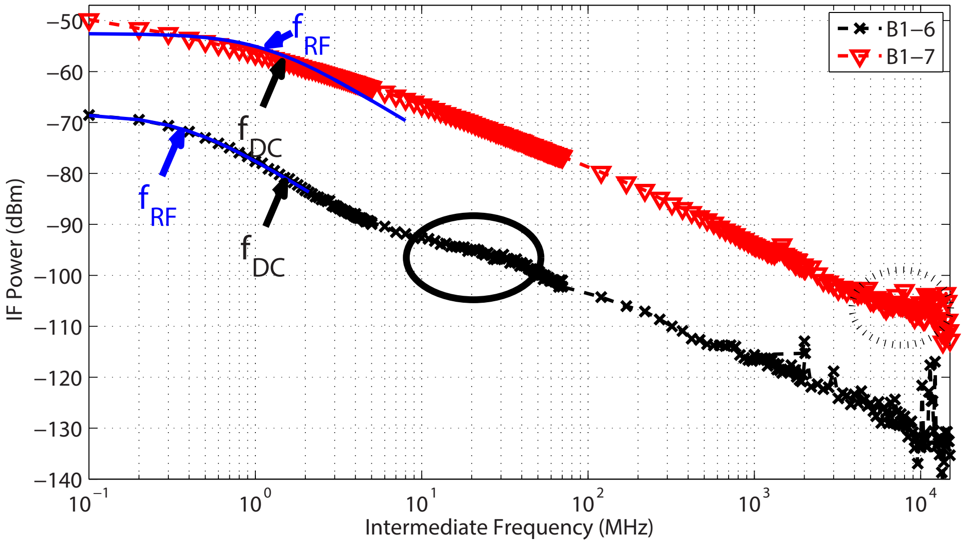

Figure 5.3: IF output power versus intermediate frequency for the mixing using the setup discussed in subsection 4.2.2. For all measurements, in all batches, the noise floor is at -130 dBm from 100kHz up to 70 MHz, and the *equivalent* noise after adding the LNA amplifiers from 70MHz on is situated at -150 dBm ; this noise is due to the spectrum analyzer (and LNA's when present). Note that the fluctuations of the incoming power as well as the transmission-line are taken into account. The arrows indicate the frequencies at which the roll-off ought to occur based on the DC-measurements. In the range between 5 and 11 MHz, a flat response is present for device 6. At much higher frequencies from 7GHz on, for device 7 a flat response is visible as well.

5.2.2 Batch 2, 25-30 nm, $855°C$

In this batch, 7 out of the 10 devices were DC measured (1 device was 'dead' and 2 were left unmeasured) and 4 of those were RF-measured. The results inside this batch are scattered (TCR, thermal boundary resistance...). The initial film quality in terms of Tc is the best of all batches (89K,figure 5.1), however on the individual devices the transition properties are only as well preserved for two devices, number 1 and 10. The other devices show significantly lower Tc (zero resistivity is measured, in contrast to previous batch). Not unsurprisingly, this scattering is also present in the other quantities like the resistivity, and the thermal boundary resistance and number 10 and 1 also pair up together with lower values for those quantities. The scattering on the thermal boundary resistance can also be seen in figure 5.28, where the thermal conductance G is not following the area in a linear trend. Device 2 and 6 have a very high thermal boundary resistance $2.9.10^{-3}cm^2K/W$. The TCR is relatively good for device 3 and 8 ($1.5.10^{-3}/K$) even though the Tc is bad (80 K).

The RF curves show very interesting behavior for the devices that were measured (figure 5.5). First observation is that the pairing up of device 1 and 10 is more or less

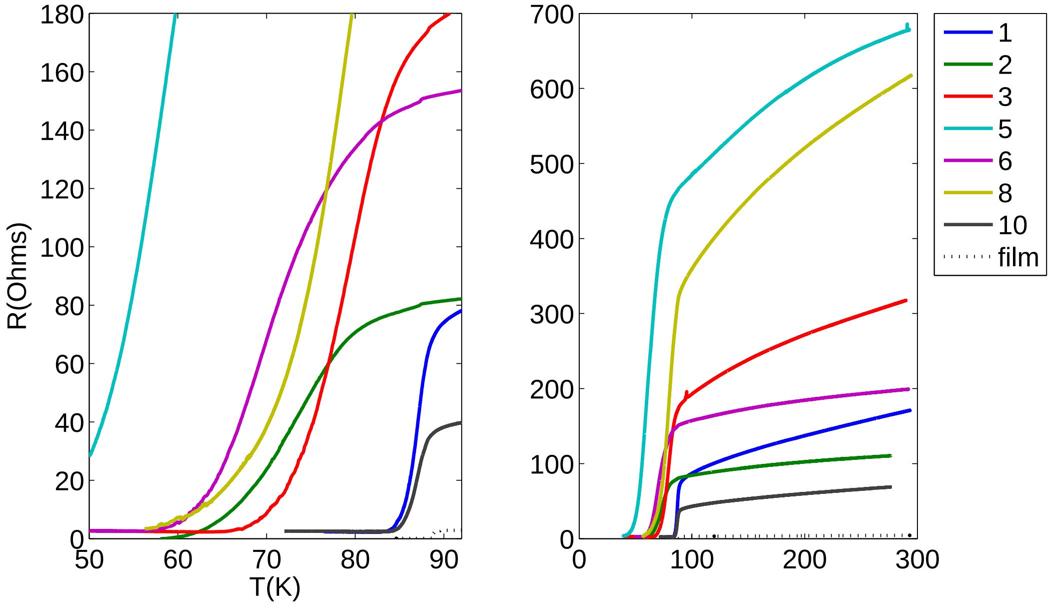

Figure 5.4: Resistance-Temperature curves for batch 2

present as well here. These two curves start reaching the plateau associated with the electron phonon interaction, very early, already at $100MHz$ (upper dashed ellipse)! For device 6 this plateau is observed as well but only at $3GHz$ (lower dashed ellipse). The data for device 2 is partly missing, the effect might still occur. Device 1 and 6 show a change in slope which we could associate with a second plateau at low frequency (we will from now on define it as 'intermediate plateau') for both situated between 6 and $11MHz$. This was the same range as device $B1-6$, although in the latter the effect was more pronounced (really flat). All devices show more or less the same response at $100kHz$, and this is the case for the DC-responsivities as well.

For device 1 the response is seen to be flat at $100kHz$. The 3-dB roll-off occurs somewhere around 1MHz as seen on the figure (see f_{RF}, extracted from lorentzian fitting in table), this is in contradiction with the DC-measurements that gives a cut-off at $38MHz$ (black arrows on figure 5.5). There is actually a roll-off for device 1 somewhere between $40-45MHz$, close to the place where the arrow is pointing. As was already pointed out in batch 1, it is possible that the first roll-off in this feature is associated with an even slower relaxation process than the phonon escape time from the film to the substrate. Device 6 shows this same roll-off feature as device 1 (at $40MHz$), although in this case the DC roll-off arrow points to $3MHz$.

It is important to note that the time constant from the lorentzian interpolation (that matches very well for device 1 and 6, but not so for 2 and 10), if it would indeed correspond to the phonon escape into the substrate, leads to a thermal boundary resistance that is by far too high compared to what is measured in literature and for all DC-

bolometer number	Length (μm)	Width (μm)	R (Ω)	dR/dT ($10^{-2}\Omega/K$)	dP/dR ($\mu W/\Omega$)
1	1.5	1.5	34	8	279
2	1	4	112	9	147
3	1	2	320	49	187
5	1.5	3	679	58	213
6	1.5	2	199	14	71
8	1.5	1	617	96	41
10	1.5	3	71	11	1000

bolometer number	ρ ($\mu\Omega cm$)	α ($10^{-3}/K$)	G ($\mu W/K$)	R_{bd} ($10^{-3}cm^2K/W$)	R_v at $1mA$ (V/W)	τ (ns)	$\boldsymbol{f_{DC}}$ (MHz)	$\boldsymbol{f_{RF}}$ (MHz)
1	1200	2.02	97	0.2	4	4	**39**	**1.7**
2	3140	0.85	14	2.9	7	51	**3**	**0.7**
3	4480	1.52	91	0.2	5	4	**41**	×
5	9510	0.85	123	0.4	5	7	**24**	×
6	1860	0.73	10	2.9	14	52	**3**	**0.6**
8	2880	1.53	39	0.4	24	7	**23**	×
10	1490	1.52	108	0.3	1	5	**32**	**1.8**

Table 5.2: Summary of DC measurements. The upper table contains the information directly obtained from the measurements (all obtained at 295 K), the lower table gives the relevant physical parameters extracted from these.

measurements (not considering batch 1), e.g. $f_{RF} \leq 3MHz$ (a value below most of what is predicted by the DC-measurements) leads to a thermal boundary resistance of $R_{bd_{RF}} \geq 3.10^{-3}cm^2K/W$. Cherednichenko et al. reports using the same DC measurement technique for sapphire with CeO_2 buffer layer $R_{bd} = 0.3 - 0.4.10^{-3}cm^2K/W$ [18]. Nahum et al. reports $R_{bd} = 0.8 - 1.4.10^{-3}cm^2K/W$ for YBCO on sapphire but with other buffer layers (with a different method but stilled based on static (zero frequency) dissipated power), [57]. The thermal boundary resistances has also been extracted from the optical response vs frequency modulation, for different substrates and with other buffer layers in [55], thermal boundary resistance $R_{bd} = 0.4 - 0.8.10^{-3}cm^2K/W$ was obtained.[6]

From $10GHz$ and higher, the IF power starts to fluctuate considerably (inside square orange rectangle on figure),but since it is out of range of interest (we were initially inter-

---

[6] These measurements were performed at cryogenics, but the thermal boundary resistance is found to be very weakly dependent on temperature (much less then 1 order of magnitude difference between 10 and 300K) [18], [58],[57], [59].

ested in the roll-off frequency related to the phonon escape time) we did not investigate this further. The problem is probably caused by the LNA's used to amplify the IF signal. Due to this coming figures show the response up to $10GHz$ (instead of $15GHz$).

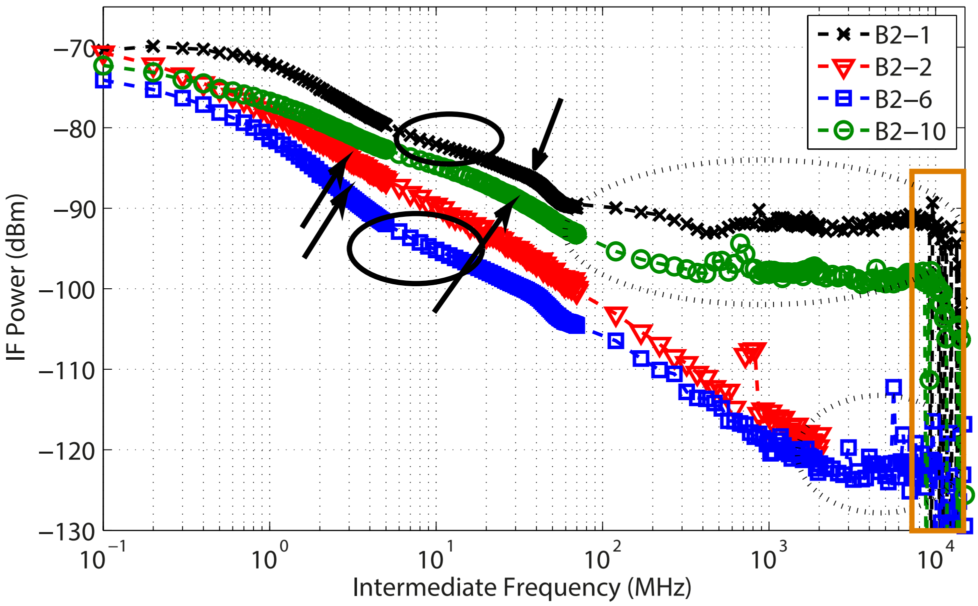

Figure 5.5: Intermediate Frequency output power versus IF-frequency. The fitting curves are omitted (values for roll-off see table). The arrows indicate the time constant extracted from the DC measurements; for device 2, 6 and 10 they do not point to any specific actual roll-off. The onset of the high frequency plateau occurs already at 100 MHz for device 1 and 10, not observed in literature.

5.2.3 Batch 3, 25-30 nm, $780°C$

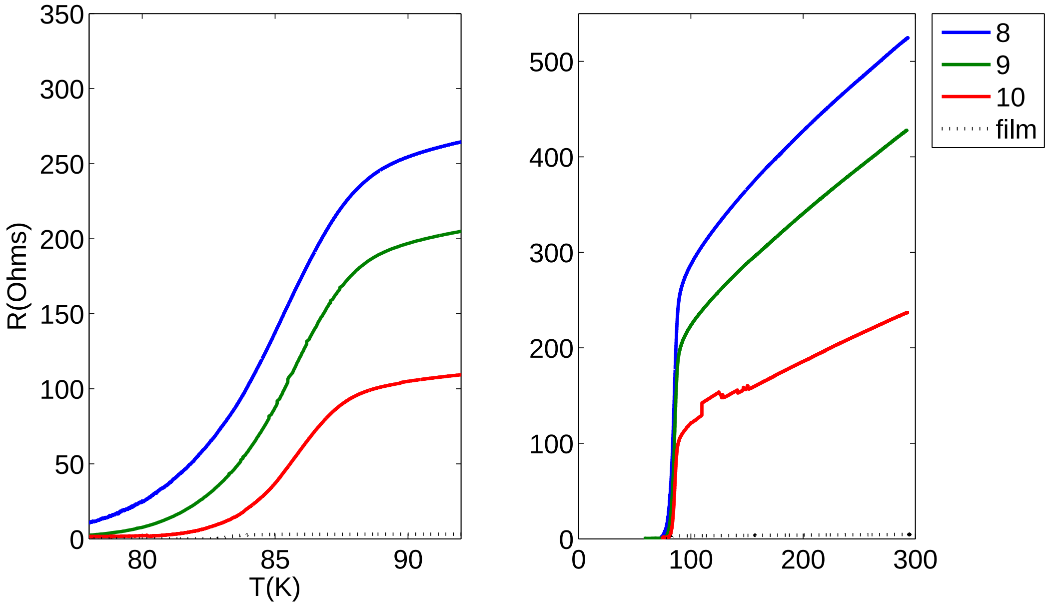

Figure 5.6: Resistance-Temperature curves for batch 3

Because the unusual results obtained in batch 1 , (for instance the very high thermal boundary resistance extracted from the DC measurements), we decided to fabricate a new batch with exactly the same parameters. The Tc of the film was very low as well (83K compared to 82K for batch 1). The Tc of the devices is higher than the film, simultaneously the transition is broader. The resistivity was extremely high in most devices, only 3 devices had a resistivity below $3000\mu\Omega cm$ (table 5.3).For those 3 devices the DC-measurements are very close to each other: almost identical and quite high TCR (around $2.10^{-3}/K$) and a thermal boundary resistance in the range that is expected based on literature and on measurements on other batches. The resistivity is relatively high ($2650\mu\Omega cm$ for device 8 and 9, and $2000\mu\Omega cm$ for device 10).

The RF curves were obtained for two samples (figure 5.7) . Both curves are very similar to each other (as are the values from the DC-measurements), and are very different from the ones measured in previous batches: No intermediate plateau is present, a 4dB/dec slope is followed by a 10dB/decade slope till 100MHz, followed by a 15 dB/dec slope till 120 MHz to finally slow down and reach the high frequency plateau. The onset of the plateau occurs however earlier for device 9. Transition between the 4dB/dec and 15dB/decade slope occurs at around 12Mz.

Even though the lorentzian fit is not very accurate in this case, the time constant matches well with the DC-measurements (for both devices), as can be seen in table 5.3, or by the arrows on the figure that indicate the roll-off estimated from the DC-measurements.

bolometer number	Length (μm)	Width (μm)	R (Ω)	dR/dT ($10^{-2}\Omega/K$)	dP/dR ($\mu W/\Omega$)
8	2.8	2	526	100	89
9	3.4	3	430	92	151
10	3.3	4	236	53	363

bolometer number	ρ ($\mu\Omega cm$)	α ($10^{-3}/K$)	G ($\mu W/K$)	R_{bd} ($10^{-3}cm^2K/W$)	R_v at $1mA$ (V/W)	τ (ns)	$\boldsymbol{f_{DC}}$ ($\boldsymbol{MHz}$)	$\boldsymbol{f_{RF}}$ ($\boldsymbol{MHz}$)
8	2630	1.92	90	0.6	11	11	**14**	×
9	2650	2.14	151	0.7	7	13	**12**	**15**
10	2000	2.24	363	0.7	3	13	**13**	**12**

Table 5.3: Summary of DC-measurements for batch 3. Resistivity for devices 1 to 7 is higher then $3000\mu\Omega cm$, so no tests were performed on those devices. The effective length is estimated here by optical microscopy to account for processing errors. The single lorentzian was used for the fit of the roll-off frequency in the last column, instead of the 2T-model, to remain consequent with respect to the other batches.

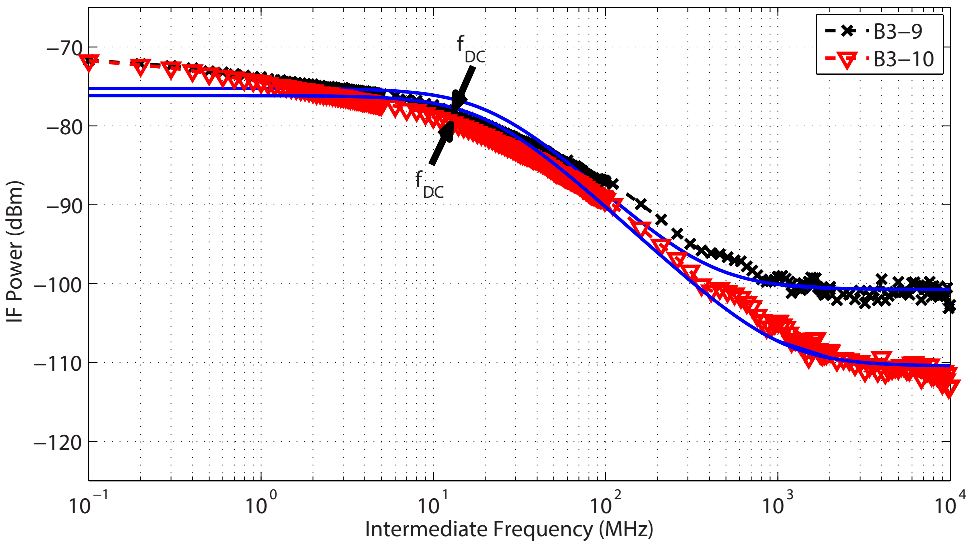

Figure 5.7: IF output power vs IF frequency combined with the a least square fit with using the two temperature model (equation (2.23), τ_{esc} and τ_{pe} and an amplitude factor are used as fitting parameters). The slope at low frequency is unexplained by the model, in literature this is attributed to substrate diffusion (e.g. [55], not for sapphire), but simulations using the appropriate parameters seem to contradict this. The roll-off fits with the time constant evaluated using the DC-method.

The DC-characteristics (TCR, thermal boundary resistance) of the devices were not at all identical to the first batch, and more in line with other batches and the values reported by [18]. Why the results are so different even though the fabrication parameters (deposition temperature, CeO_2 thickness) are the same, might reside in fabrication errors. Errors could have occurred in the first batch, although none were noticed, since it was the first made, this is still possible. An error, of which the cause is unknown, occurred during fabrication of the third batch. After the wet etching, respecting the etch-time, the 20nm of gold was not fully removed as seen by inspection under microscope (figure 5.8a). It was decided to continue etching for 15 seconds, and it resulted in the almost complete (and desired) disappearance of the gold, some spots are still visible on after the last process step, figure 5.8b. The same figures also reveals the presence of a large under etch, explained by the longer etching time. This undercut increases the effective bolometer length, but not to the extend to explain the very high value of the resistances. Definitely another batch should be fabricated with same deposition temperature and CeO_2 thickness to confirm or contradict results in batch 1 and 3.

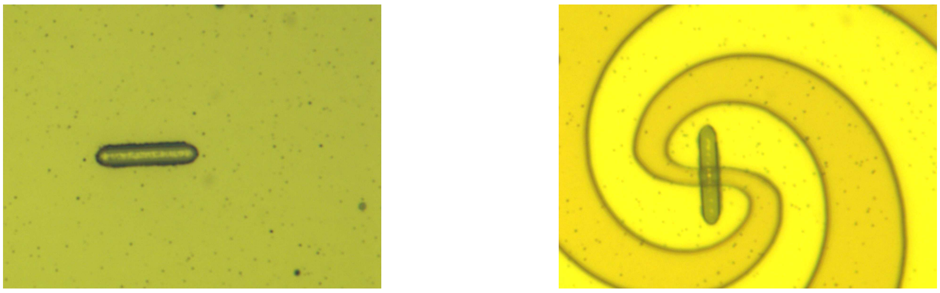

(a) (b)

Figure 5.8: (a) After first wet etch, gold is still visible on top of the grey YBCO. (b) After a second etch and performing the rest of the lithography gold is still present but in lesser amounts. The underetch is also visible (blue ripples on the border of the YBCO) .

5.2.4 Batch 4, 25-30 nm, $835°C$

DC tests were performed on six devices in this batch. It is the only batch where all measured devices have a transition to superconductivity above 85K (figure 5.9). Maybe surprisingly, devices 1 and 2 had a Tc that was better than the film itself. The TCR is between $2.10^{-3}1/K$ and $2.4.10^{-3}1/K$ for all devices with the exception of device 4 having TCR equal to $1.10^{-3}.1/K$ (visible by the lower slope on figure 5.9). Resistivity remains below $1500\mu\Omega cm^2$ for all devices, this trend is also present for the batches that are fabricated afterwards (figure 5.25). This batch has the lowest measured thermal boundary resistance of all batches, and has a low scattering, with values between $0.14.10^{-3}cm^2K/W$ and $0.25.10^{-3}cm^2K/W$.

For the RF-measurements only three of the six DC-characterized devices were still working. The three curves are very similar, all flat at low frequency, all three show a

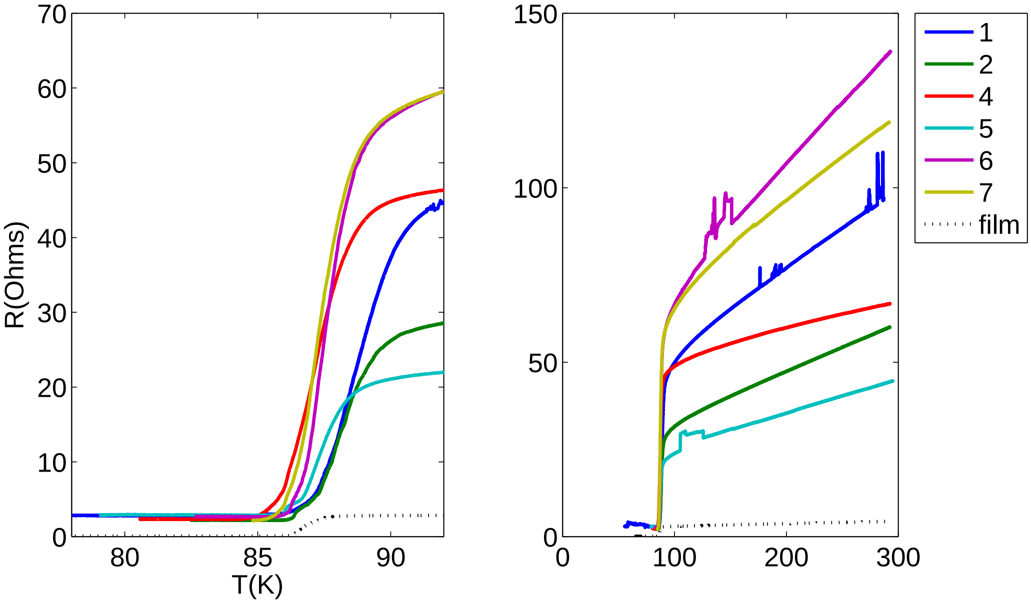

Figure 5.9: Resistance-Temperature curves for batch 4

first roll-off around 3 MHz -the DC extracted time constant lies at least 10 times higher in frequency (figure 5.10)- and all reach the plateau at $1GHz$. Device 6 and 7 have a change of slope at $6MHz$. Their initial slope is $10dB/dec$, whereas for device 1 it is lower, $6dB/dec$. From $6MHz$ on all have the same slope. At $40MHz$ the slope becomes steeper again,14 dB/dec for all of them, to finally become flat at 1GHz.

By accident, device 7 was first measured without applying any bias current (leaving the bias line open), surprisingly the device showed a non-zero response above the noise level of the amplifier. The effect has been observed for THz pulses (80ps) in [60], however the author attributes it to heat dissipated by vortex motion in the YBCO generated by the RF-currents. Yet vortexes are only observed when a material is in its superconducting state, so this can not justify the response at room temperature (where the film is in its normal state). Hence the origin of this phenomena remains unexplained, and puts a doubt on the explanation at superconducting state found in [60]. We decided to repeat this experiment, and measured the curve for different bias currents between 0 and $500\mu A$ (else the bias current is always at $500\mu A$) on a device in batch 7 (see figure 5.21).

bolometer number	Length (μm)	Width (μm)	R (Ω)	dR/dT ($10^{-2}\Omega/K$)	dP/dR ($\mu W/\Omega$)
1	1	2	97	22	634
2	1	3	60	14	794
3	1	1.5	119	×	350
4	1	1	67	58	558
6	1.5	1.5	139	14	262
7	1.5	1	119	14	385
9	1.5	3	72	×	667
10	1.5	4	49	×	1000

bolometer number	ρ ($\mu\Omega cm$)	α ($10^{-3}/K$)	G ($\mu W/K$)	R_{bd} ($10^{-3}cm^2K/W$)	R_v at $1mA$ (V/W)	τ (ns)	$\boldsymbol{f_{DC}}$ (MHz)	$\boldsymbol{f_{RF}}$ (MHz)
1	1360	2.26	139	0.1	1.6	3	**62**	**2.8**
2	1270	2.25	108	0.3	1.3	5	**32**	×
3	1250	×	×	×	2.8	×	×	×
4	470	1.04	39	0.3	1.8	4	**35**	×
6	980	2.46	90	0.3	3.8	4	**36**	**2.6**
7	560	1.98	91	0.2	2.6	3	**54**	**2.4**
9	1000	×	×	×	1.5	×	×	×
10	910	×	×	×	1.0	×	×	×

Table 5.4: Summary of DC-measurements for batch 4. The discrepancy in the estimated time constant from both methods is extreme (two last columns), not even a correlation is present.

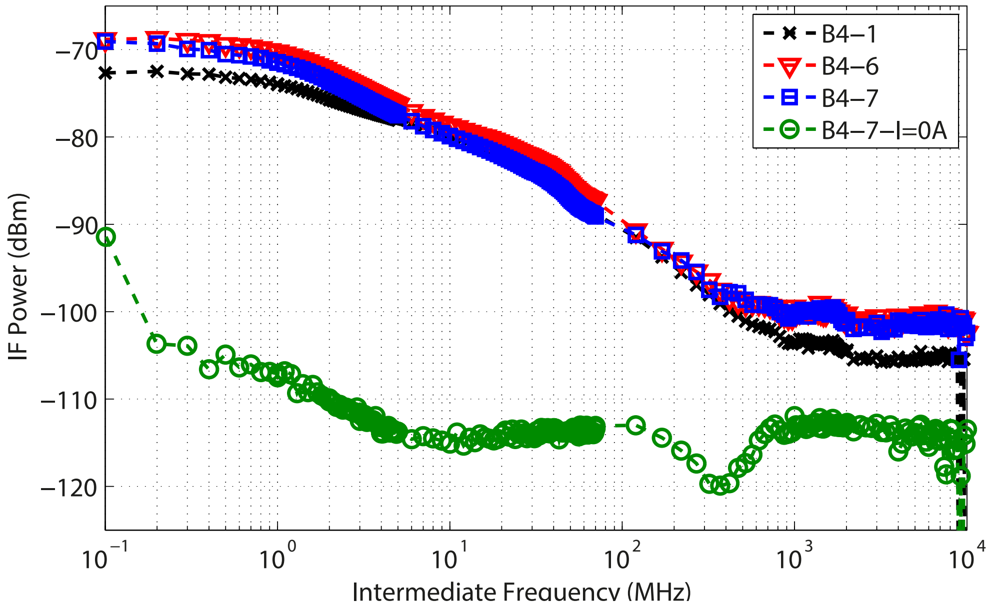

Figure 5.10: IF power versus IF frequency. Device 7 left unbiased gives a frequency response above the noise floor, but with an overall shape very different from when the $500\mu A$ is applied.

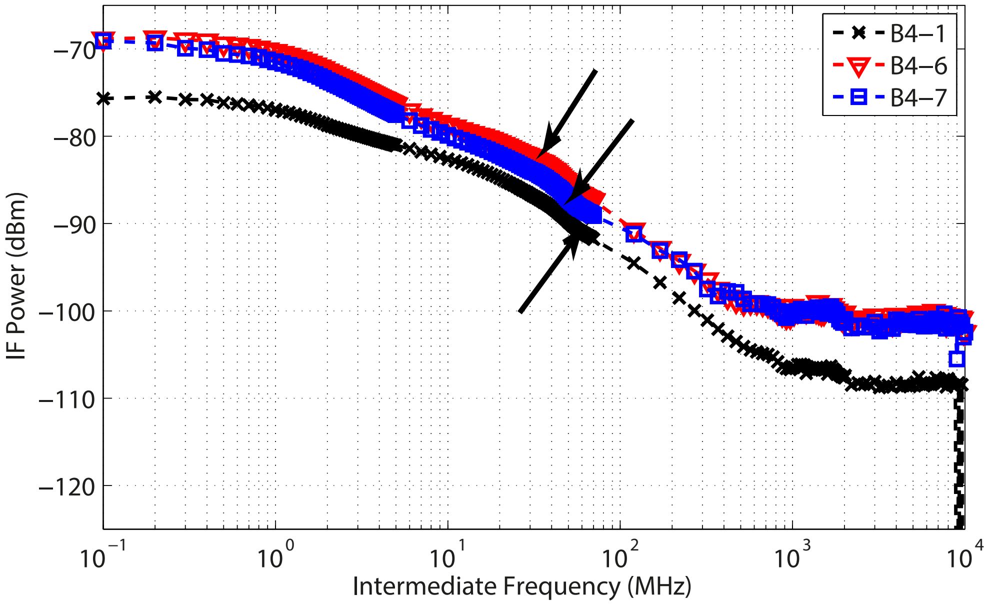

Figure 5.11: IF power versus IF frequency. The response of device 1 has been shifted down by $3dBm$ in order not to overlap with the other curves. All curves are very similar. The arrows do point at a place where a change in slope is occurring, but it is not associated with the lowest frequency roll-off (occurring around $3MHz$).

5.2.5 Batch 5, 50-60 nm, $835°C$

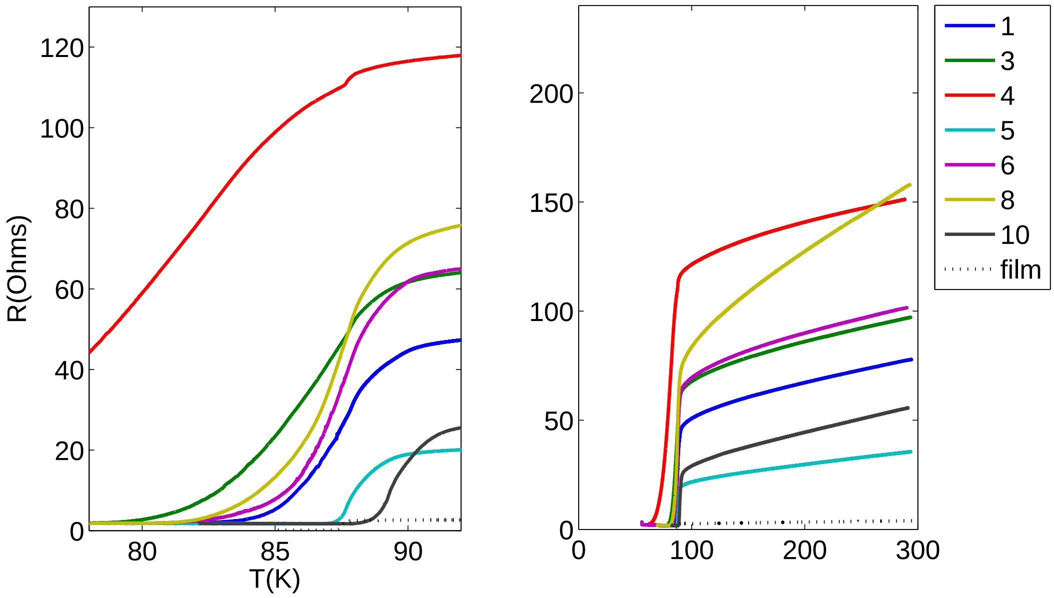

Figure 5.12: Resistance-Temperature curves for batch 5

From this batch on we decided to maintain the temperature deposition at $835°C$ and vary the buffer thickness. As was already mentioned, the Tc of the films remained unaffected by the buffer thickness (figure 5.1).

Prior to the discussion, it is important to note that a fabrication error was made in this batch. Etching of the 10nm of gold to expose the YBCO was forgotten, the mistake was only noticed when the second lithography had already been performed and the sample had been exposed to 10 minutes of ion etching. To correct for this, the (baked and burned) resist for the pattern definition had to be removed. After several plasma-etches (up to 3 minutes on 350W of oxygen plasma) and high-power ultrasonic baths remains of resist were still visible on the microscope. Nevertheless, the gold etch was then performed and the second lithography repeated. Here alignment was crucial in both (lateral) directions since the film had already been exposed once to argon bombardment that started to pattern the YBCO bridge. Surprisingly, in spite of this mistake and the numerous extra processing that required to correct this, results in terms of transition to superconducting state and resistivity for batch P5 are good.

Nothing peculiar in this batch in terms of DC measurements is present. The resistivity of all devices is relatively normal, with an average of $1100\mu\Omega.cm$ and standard deviation of $200\mu\Omega.cm$. The TCR is not so good overall, with only 2 out of 7 measured devices having a TCR above $2.10^{-3}/K$. The transition to superconducting state is rather good, although the transition width is somewhat broad, compared to batch 4, all Tc's lies between $85K$ and $90K$ (as defined as the point where the slope is highest),

bolometer number	Length (μm)	Width (μm)	R (Ω)	dR/dT ($10^{-2}\Omega/K$)	dP/dR ($\mu W/\Omega$)
1	1	2	78	10	455
2	1	3	56	×	1690
3	1	1.5	97	11	250
4	1	1	152	11	2380
6	1.5	1.5	102	12	360
8	1.5	2	158	32	190
10	1.5	4	56	12	667

bolometer number	ρ ($\mu\Omega cm$)	α ($10^{-3}/K$)	G ($\mu W/K$)	R_{bd} ($10^{-3}cm^2K/W$)	R_v at $1mA$ (V/W)	τ (ns)	$\boldsymbol{f_{DC}}$ (MHz)	$\boldsymbol{f_{RF}}$ (MHz)
1	1090	1.33	47	0.4	2.2	8	**21**	**0.09**
2	1180	×	×	×	9	×	×	×
3	1020	1.17	28	0.5	5	9	**17**	**0.06**
4	1060	0.74	11	1.0	5	17	**10**	×
5	1000	1.68	142	0.3	0.4	5	**32**	**0.7**
6	714	1.15	42	0.5	2.8	10	**17**	**0.4**
8	1480	2.05	62	0.5	5.3	9	**18**	×
10	1050	2.13	80	0.8	1.5	13	**12**	**1.0**

Table 5.5: Summary of DC-measurements for batch 5. As for batch 4, the discrepancy in the estimated time constant from both methods is extreme (two last columns)

with the exception of device 4, which is clearly different. Also noticeable is device 10 showing a higher Tc than the film. The thermal boundary resistance is comparable to the one in batch 6 and 7, but overall less scattered, and higher than batch 4 (figure 5.23). Related to this, the (DC measured) thermal conductance scales well with the area, with the exception of device 10.

The RF-measurements reveal very different curves. Contrary to batch 4 where all devices have flat response between $100kHz$ and $1MHz$, here none of the devices do. We decided to record the response below $100kHz$ using the setup described in figure 4.3. This setup reads the response at the amplitude modulation frequency in units of volts on the lock-in amplifier and was thus converted to units of power (assuming a 50Ω load for conversion) so that after concatenation with the data above $100kHz$, both frequency ranges could be shown on the same graph. There is continuity of the slope at $100kHz$ for all devices, with the exception of device 5, this is clearly due to some measurement artifact. $3dBm$ roll-off extracted using the lorentz fitting reveals frequencies below $1MHz$. Like for batch 4, this is more than a factor of 10 lower than the DC estimated frequency roll-off occuring for all devices above $10MHz$!

Looking at figure 5.14, device 1 and 10 show very similar behavior versus frequency as well as device 3 to some extend with 6. The thermal boundary resistance extracted by the DC measurements is again not revealing a cut-off or change in slope. Also, the thermal boundary resistance for 5 and 10 are very different, $0.28.10^{-3}cm^2K/W$ and $0.78.10^{-3}cm^2K/W$ respectively, although the frequency behavior are very similar. The Tc is seems not to be a factor for the frequency behavior: devices 3 and 6 have almost identical transitions (figure 5.12) but non similar frequency curves.

The last plateau is reached at $200MHz$ for device 1, 5 and 10 , at $1GHz$ for device 3 and $4GHz$ for device 6. Also for this behavior no correlation was found with the measured DC-parameters (ρ, TCR, Tc, R_{bd}).

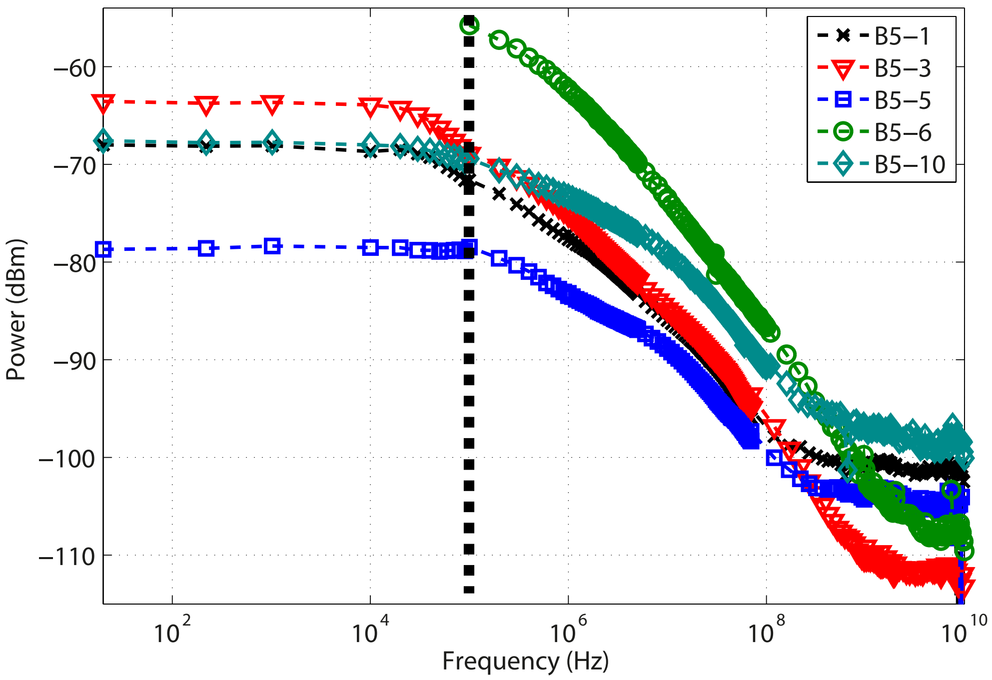

Figure 5.13: IF power versus IF frequency. Note that the lock-in amplifier voltage response for the low frequencies has been converted to an equivalent power expressed in dBm to enable to view the overall response on a single graph. The setup is changed at 100 kHz, denoted by the black line. The frequency response below 100 kHz was not taken for device 6.

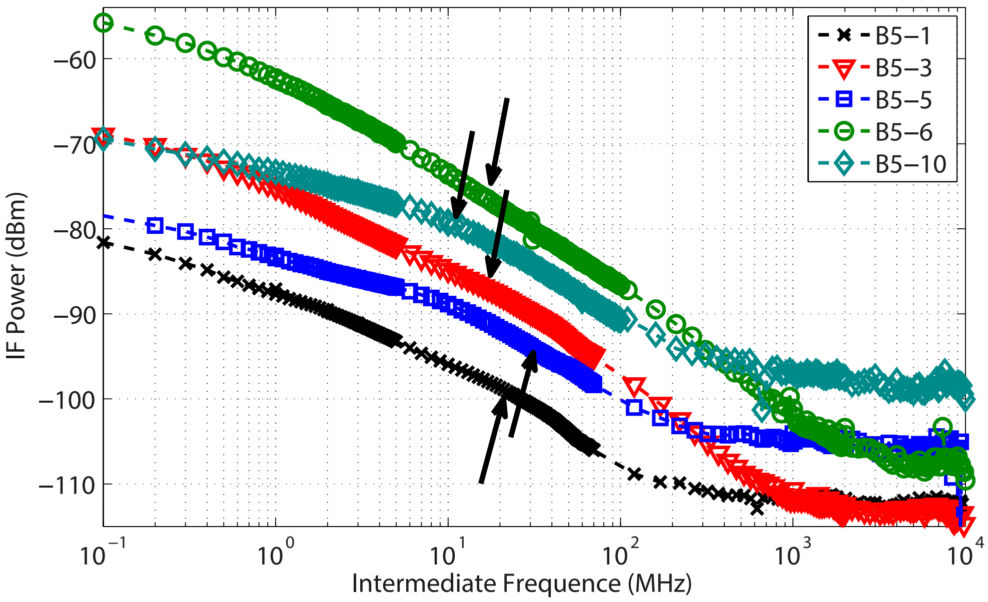

Figure 5.14: IF power versus IF frequency. The response of device 1 is shifted downwards by 10 dBm for clarity.

5.2.6 Batch 6, 12-15 nm, $835°C$

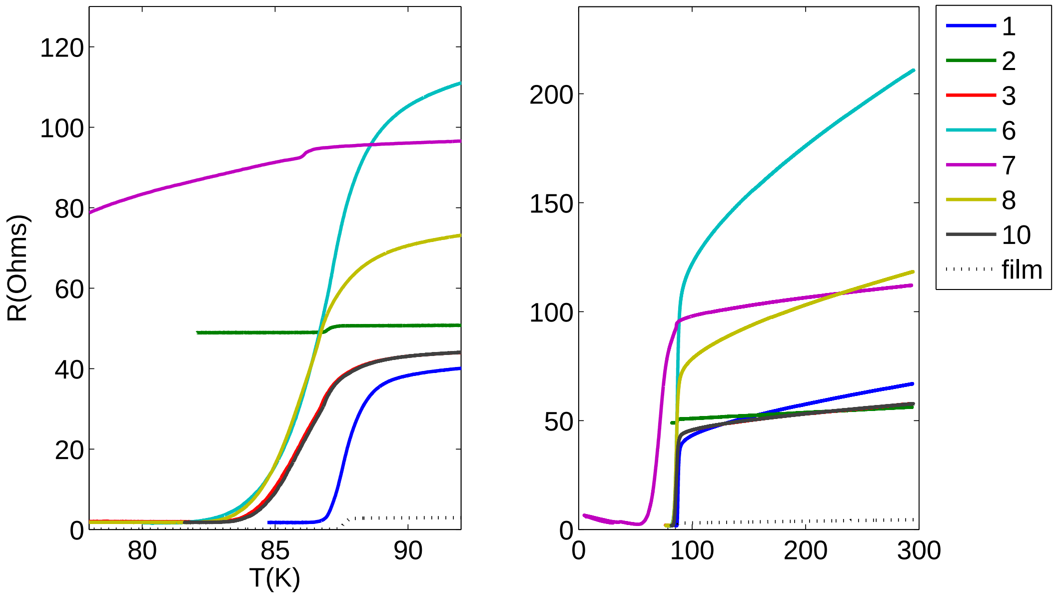

Figure 5.15: Resistance-Temperature curves for batch 6

This batch has a much thinner CeO_2 layer than the others, it does not affect the Tc of the film. The Tc of most devices lies also above $85K$. It is worth noting that device 2 does not reach to zero resistance, although a small feature related to the superconducting transition is visible, this is similar to what was observed in batch 1.

The resistivity of the film is similar to the one of batch 5 with an average of $990\mu\Omega.cm$ and standard deviation of $330\mu\Omega.cm$. The thermal boundary resistance, on the contrary, is very scattered, with device 2, 7 and 10 showing very high values between $3.5.10^{-3}cm^2K/W$ and $3.8.10^{-3}cm^2K/W$ the other devices lying between $0.4.10^{-3}cm^2K/W$ and $0.8.10^{-3}cm^2K/W$ (this can also be seen in figure 5.17, where the arrows indicate the cut-off frequency which is proportional to R_{bd}, or by looking in figure 5.23 or again at figure 5.28). The TCR is low in this bach, with an average of $1.10^{-3}/K$, the highest value measured is $1.610^{-3}/K$.

Since the slope for several devices was not flat at $100kHz$, we measured the low frequency response using the setup on figure 4.3 as was done with previous batch. This time however, the slope at $100kHz$, which is the frequency at which transition between the two setups occurs, was far from being continuous for several devices. This result cannot be explained, it is definitely not physical but linked to the measurement-setup, further investigation would be required. [7]

---

[7] The transfer function of the transmission line after the detector block for this setup was performed in a similar way as is done for the mixer setup.

bolometer number	Length (μm)	Width (μm)	R (Ω)	dR/dT ($10^{-2}\Omega/K$)	dP/dR ($\mu W/\Omega$)
1	1	2	67	9	458
2	1	3	56	3	294
3	1	1.5	58	5	385
6	1.5	1.5	211	33	176
7	1.5	1	112	5	68
8	1.5	2	118	15	253
10	1.5	4	58	4	399

bolometer number	ρ ($\mu\Omega cm$)	α ($10^{-3}/K$)	G ($\mu W/K$)	R_{bd} ($10^{-3}cm^2K/W$)	R_v at $1mA$ (V/W)	τ (ns)	$\boldsymbol{f_{DC}}$ (MHz)	$\boldsymbol{f_{RF}}$ (MHz)
1	940	1.40	43	0.5	2.2	8	**20**	**1.2**
2	1180	0.48	8	3.8	3.4	67	**2**	**0.4**
3	610	0.84	19	0.8	2.6	14	**11**	×
6	1470	1.61	60	0.4	5.7	7	**24**	**2.8**
7	520	0.52	4	3.8	14.8	68	**2**	**1.0**
8	1100	1.30	39	0.8	4.0	14	**12**	×
10	1080	0.74	17	3.5	2.5	62	**3**	**1.0**

Table 5.6: Summary of DC-measurements for batch 6. For the fitting, because of the discontinuity in the response between the two methods, only the data above 100 kHz was used in the case of device 6 and 7.

Nonetheless, it is clear by just looking at figure 5.17 that the DC extracted time constant and the fitted lorentzian function do not match.

In order to verify that the measurements are reproducible for a same device, device 2 was measured on two different occasions, identical frequency-responses were obtained (figure 5.16).

The final plateaus are reached at 200, 400 , 600MHz for devices 10, 6 and 1 respectively. For device 2 and 7 the plateau is not observed in the measured frequency-range, interestingly these have devices have a bad Tc (70 K for device 7 and a slight drop without going to zero in resistivity for device 6 at 86 K). The devices in other batches having such low Tc characteristics also did not show a clearly identifiable high frequency plateau (see summarizing figure 5.29).

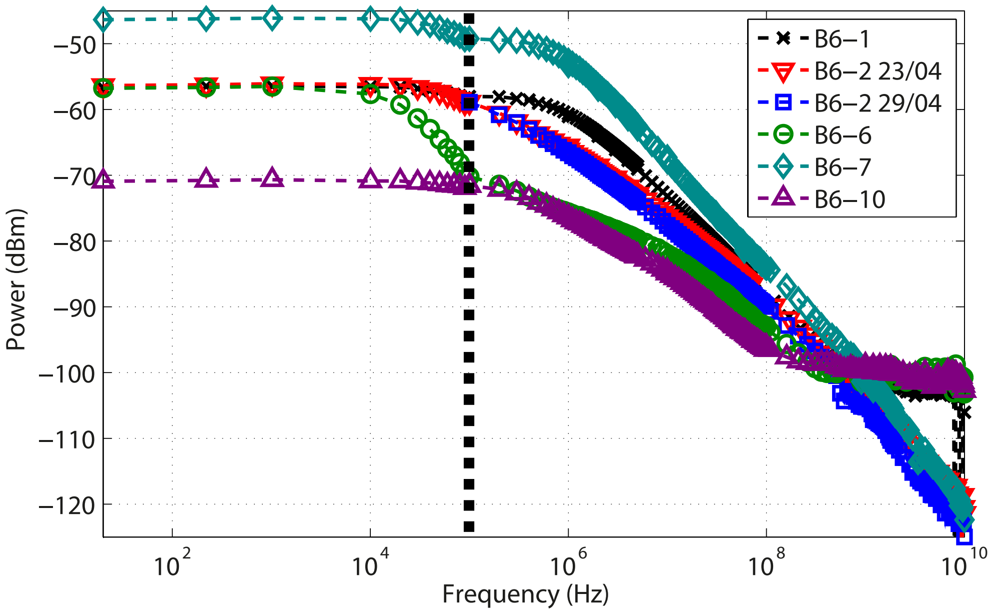

Figure 5.16: The transition from low frequency and high frequency occurring at $100kHz$ is not smooth for some devices. Device 2 was measured on two different days, the response is identical on both occasions.

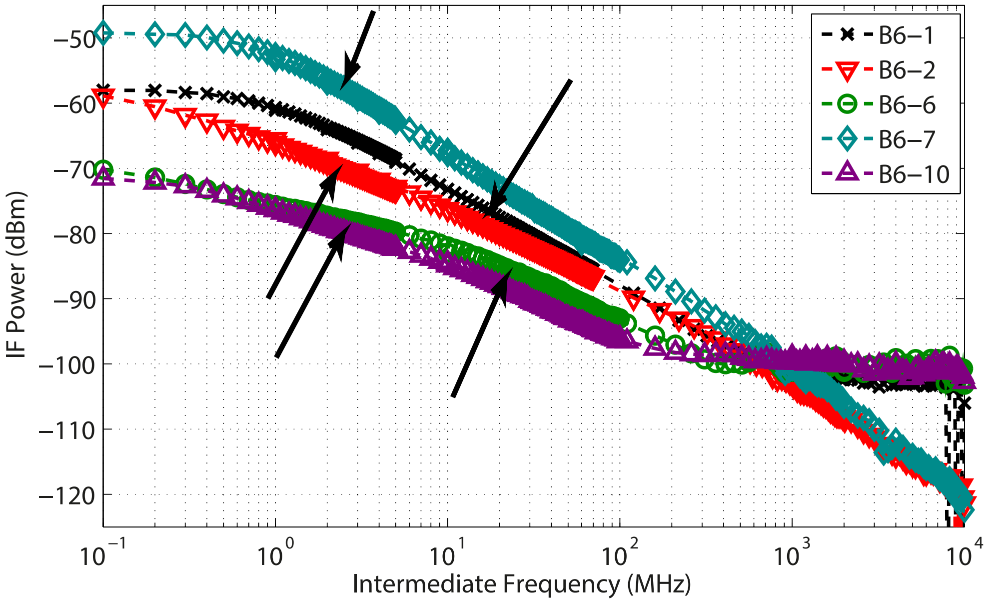

Figure 5.17: Scattering in the thermal boundary resistance. The low frequency DC roll-offs values are attributed to a low dR/dT used to calculate the thermal boundary resistance, however this does not affect by any means the actual frequency response.

5.2.7 Batch 7, 50-60 nm, $835°C$

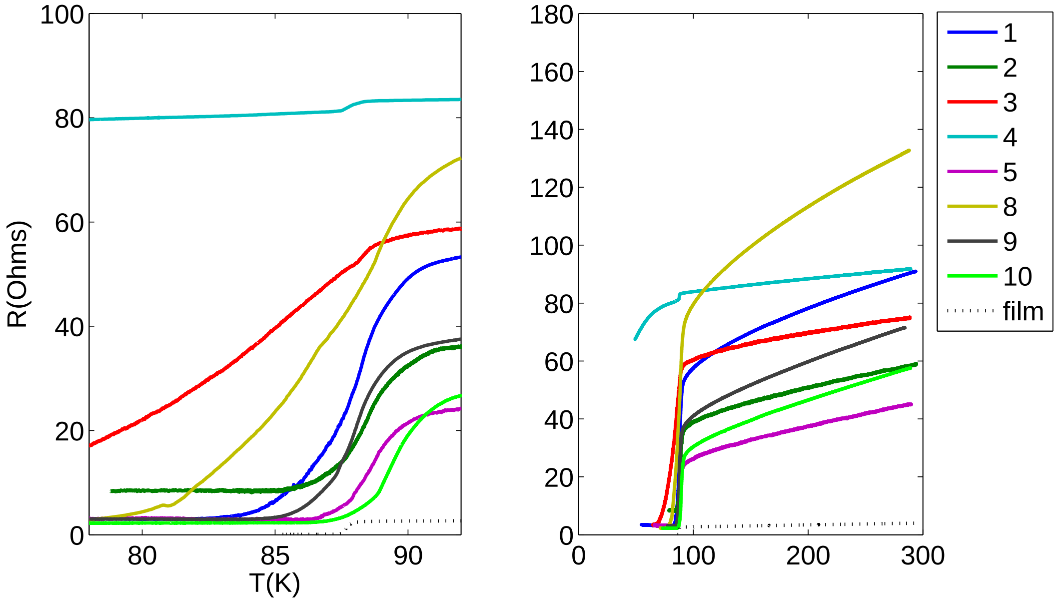

Figure 5.18: Resistance-Temperature curves for batch 7

Because of the fabrication error in batch 5, a new film was deposited in exactly the same conditions, with the same thickness of CeO_2, four times as thick as in batch 6, twice as thick as the one in batches 1-4.

Not much difference with batch 5 is observed. A slightly higher resistivity: $1180\mu\Omega.cm$ and a standard deviation of $370\mu\Omega.cm$, the TCR is scattered to the same extend. The same thermal boundary resistance is obtained (well illustrated in figure 5.28).

The RF-measurements reveal for devices 8 and 9 as was the case in batch 2 and 4, a (not entirely flat) 'intermediate plateau' around $6MHz$. Interestingly, device 9 has a very similar RF-response to the devices in batch 4 (flat till $1MHz$, change of slope at $6MHz$ and high frequency shelf starting at $2GHz$). Device 1 and 8 have some additional features between 570 and $820GHz$ (indicated in the black ellipse on figure 5.20).

Device 8, 9 and 10 have flat responses below $1MHz$, whereas device 1 is still in decrease. In contrast to batch 5 (and batch 6), the high frequency plateau occurs at much higher frequencies, $1GHz$, for device 1, 9 and $2GHz$ for 10, and $3.5GHz$ for device 8.

The thermal boundary resistance exctacted from the DC measurements is situated in a narrow range in this batch, which can also be seen by the linear behavior in of G versus area in figure 5.28.

Again it is clear by just looking at figure 5.17 or table 5.7 that the DC extracted time constant and the fitted lorentzian function do not match.

In batch 4, it was mentioned that a non zero response was obtained although the

bolometer number	Length (μm)	Width (μm)	R (Ω)	dR/dT ($10^{-2}\Omega/K$)	dP/dR ($\mu W/\Omega$)
1	1	2	91	12	290
2	1	3	59	8	770
3	1	1.5	75	5	320
4	1	1	92	3	156
5	1	4	45	8	1818
8	1.5	2	134	18	286
9	1.5	3	73	13	833
10	1.5	4	58	12	1250

bolometer number	ρ ($\mu\Omega cm$)	α ($10^{-3}/K$)	G ($\mu W/K$)	R_{bd} ($10^{-3}cm^2K/W$)	R_v at $1mA$ (V/W)	τ (ns)	$\boldsymbol{f_{DC}}$ (MHz)	$\boldsymbol{f_{RF}}$ (MHz)
1	1270	1.36	36	0.6	3.5	10	**16**	×
2	1240	1.46	66	0.5	1.3	8	**20**	**2.0**
3	790	0.67	16	0.9	3.1	16	**10**	×
4	640	0.35	5	2.0	6.4	35	**5**	×
5	1270	1.67	138	0.3	0.6	5	**31**	×
8	1250	1.38	53	0.6	3.5	10	**16**	**1.1**
9	1870	1.76	107	0.4	1.2	8	**21**	**2.8**
10	1090	2.02	147	0.4	0.8	7	**22**	**7.6**

Table 5.7: Summary of DC-measurements for batch 7. The outsider number 4 can be noted, having a low resistivity, low TCR and high thermal boundary resistance.

current was set to zero (kept floating). The response curve as such was different than the one of were a bias of $500\mu A$ was applied. Hence we decided to repeat the experience but this time we varied the bias current gradually from zero to $500\mu A$ and to gain time measured on a smaller frequency interval, from 70 MHz to 2.200 GHz. The results are plotted in figure 5.22 and 5.21. The influence of the bias current on the RF-curves was recorded for device 8. The responsivity scales linearly with the current as it should by equation (2.7) (the bias current is low enough so as not to alter the dR/dT). However for currents below $50\mu A$ the RF-curves are not a shifted replica of each other, this effect becomes visible starting at frequencies above 200 MHz.

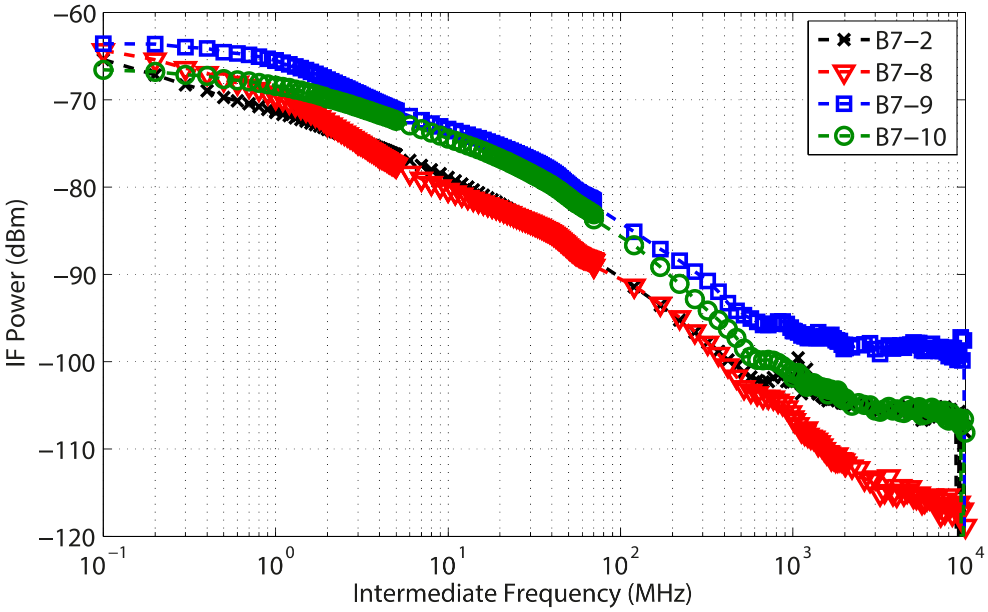

Figure 5.19: Resistance-Temperature curves for batch 7

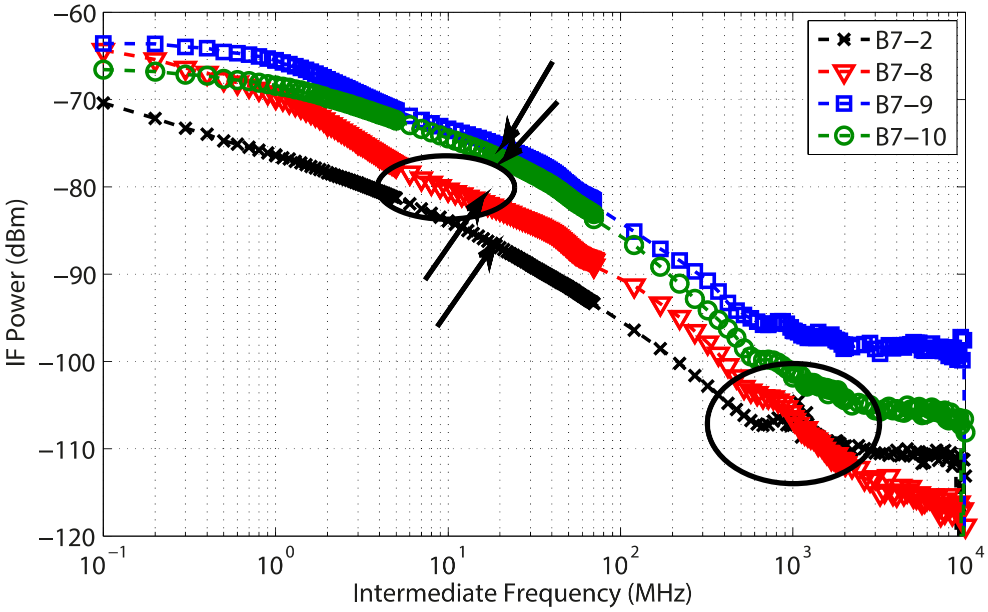

Figure 5.20: The curve of device 2 is shifted down by 10dB to allow for clarity. Device 8 has the most complex structure with 2 small plateaus on at low frequency $7 - 20MHz$ and one at $570 - 820MHz$ (indicated inside the ellipses) to finally become flat later than the other devices, at $2GHz$. DC thermal boundary resistance is exactly the same in all 4 cases (arrows on same frequency), however the responses are very different

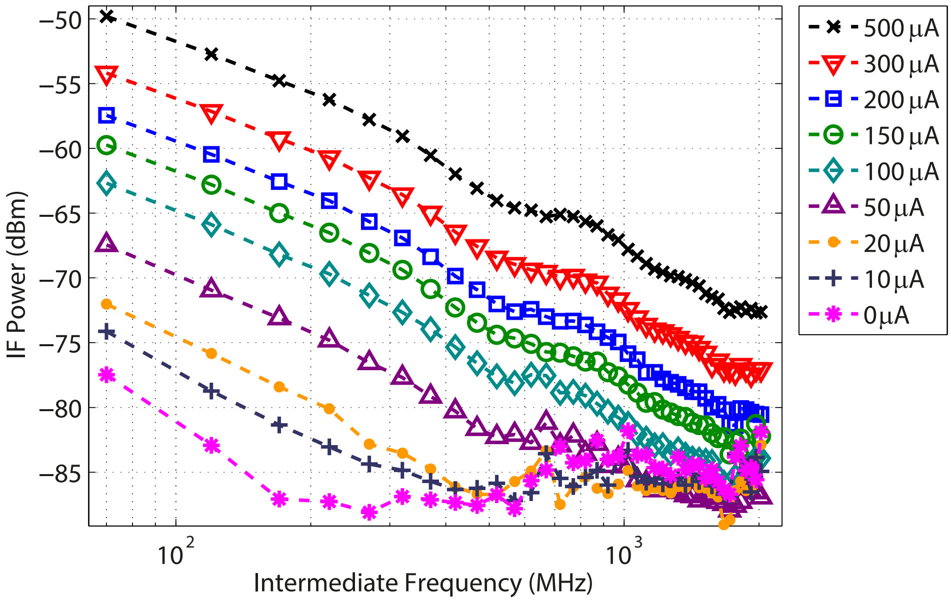

Figure 5.21: IF-power as a function of IF frequency, from $70MHz$ to $2.2GHz$, for different values of bias current of device P7-8. At bias currents below $50\mu A$, the relative responses as a function of frequency are different.

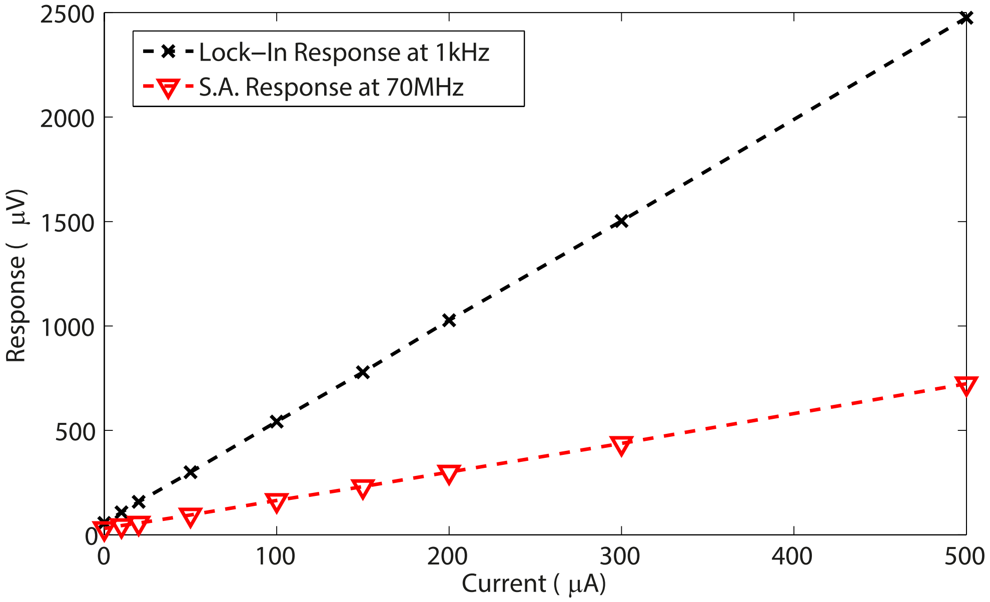

Figure 5.22: Voltage response at different bias currents, for device P7-8, at 1 kHz recorded with lock-in amplifier and at 70 MHz with the spectrum analyzer. As expected it scales linearly with current. The response on the spectrum analyzer was taken at 100 kHz from figure 5.21 and was converted from dBm to μV, assuming a 50Ω load. It can also be noted that the response is at 70 MHz is lower than that at $1kHz$, but quantitatively not in accordance to the at least 25dBm difference in response observed on figure 5.20.

5.3 Summary

The Tc of the films was clearly influenced by the deposition temperature. The buffer layer thickness did not modify the Tc. Toma reports increased CeO_2 resulted in reduced Tc [60]. Rönnung et al. on the other hand mentions no influence of the thickness of the buffer layer on Tc [48]. No literature at all is available regarding the effect of a buffer layer thickness on the thermal properties of the bolometer.

Apart from the Tc, from the results presented in this work it can be concluded that neither the temperature deposition nor the buffer layer thickness-in the range for which the parameters were varied- has any influence on the electrical or thermal properties. Specifically, the property that was hoped to be influenced upon was the thermal boundary resistance (figure 5.23). The fact that the CeO_2 thickness has no influence is maybe not surprising, when considering work in [61] and [57]: both papers investigate different substrates and buffer types, and obtain very similar thermal boundary resistances. The former extracts the thermal boundary resistance from the optical response vs modulation frequency and obtains values between $0.4.10^{-3}cm^2K/W - 0.8.10^{-3}cm^2K/W$ for different substrates. Although these measurements are performed at cryogenics, the thermal boundary resistance has been shown to remain almost constant with temperature [18], [58],[57], [59]. The latter [57], evaluates it by probing the stationary temperature profile beneath a heated YBCO strip and obtains $0.8.10^{-3}cm^2K/W - 1.4.10^{-3}cm^2K/W$ for using different buffer layers on sapphire (CeO_2 is not one of them).

The thermal boundary resistance extracted using the DC method remains fairly constant in some batches whereas in others the scattering is more pronounced (figure 5.23, we note also that not all devices in all batches have been measured). Overall the magnitude of variations is more than a factor of 10, with several values exceeding $3.10^{-3}cm^2K/W$. Thermal boundary resistances higher than $1.5.10^{-3}cm^2K/W$ to the best of our knowledge has only been reported in [59]. Most values are however, situated between $0.1.10^{-3}cm^2K/W$ and $1.10^{-3}cm^2K/W$, this is consistent with what is found in literature (i.e. for different substrate and thickness since no thermal boundary resistance has been evaluated for CeO_2 on sapphire, summarized results are found in [58]).

The thermal boundary resistance ought to be extracted using the RF method as well. Fitting a simple lorentzian, we obtained values for the time constants; these are however always below 3 MHz, with the exception of batch 3. Assuming this time constant to be associated with the phonon escape to the substrate, a thermal boundary resistance using $R_{bd} = \frac{\tau}{cd}$, would give values above $3.10^{-3}cm^2K/W$, this is in contradiction with the values mentioned in above paragraph (both from literature as from the measurements). Figure 5.30 compares the frequency roll-offs using the two methods. The two frequency roll-offs do not to match. We are unable to explain this discrepancy, but we expect it to be related to unaccounted thermal phenomena. We believe the measurement methods are correct.[8]

Deviations with the two temperature model are omnipresent. As was mentioned, for

---

[8] To confirm that the dc-responsivity, using the method described in section 4.1.1, is correct, optical responsivity tests could be performed as well.

all devices (with the exception of batch 3), the fitted lorentzian model[9] has a roll-off frequency that is below $3MHz$, this results in high values for the thermal boundary resistances, which we believe are unphysical. Also in some cases the fit on the experimental data was not accurate. Based on these arguments we suspect this first roll-off not to be associated to the phonon escape time. A considerable number of devices show after the first roll, a flat or low slope at frequencies followed by a second roll-off in a range lying between 4 and 60 MHz (for instance B1-6, B2-1, figures 5.3 ,5.5), we rather suspect this second roll-off lying at higher frequencies to be associated with the phonon escape time (at least when present). In literature a low frequency behavior is attributed to diffusion inside the substrate. It can be modeled using the diffusion equation assuming a radial temperature profile as discussed in section 2.4. Modeling this in the particular case of sapphire at room temperature however shows that the substrate diffusion cannot possibly account for the observed slope or roll-off. This is due to the very high thermal conductivity of sapphire compared to other substrates. The result of this modeling is shown in figure 2.6. Another thermal process neglected in the final equation of the two temperature model is phonon diffusion into the contact pads. It is easily verified that including this effect only results in a shift to the right of the roll-off frequency but ought to be taken into consideration for a proper quantification of the thermal boundary resistance from the RF measurements: $\tau_{effective}^{-1} = \tau_{esc}^{-1} + \tau_{diff}^{-1}$.[10] Further investigation in the thermal phenomena is hence required to find the origin of the discrepancies with the model. Since thermal constants like specific heat capacitance and conductivity are temperature dependent, it would also be interesting to measure the RF-curves at Tc to see to what extend the curves are modified.

Apart from the thermal boundary resistance, the resistivity and the TCR are independent of geometry, these intrinsic material properties should be constant for all devices inside one batch, however this is not the case (figures 5.25,5.26).

The Tc of the individual devices was in some cases lower than the one of the film. A few devices showed an excessively degraded transition to superconductivity. In those cases the TCR was very low resulting in an above average value for the thermal boundary resistance or equivalently, low value for the extracted frequency roll-off. The RF-response of these devices did not have a high frequency plateau in the measured frequency range (with the exception of $B1-7$ where it seems to occur).

The high frequency plateau was observed in most devices. According to the two temperature model (explained in section 2.4) the onset is associated with the phonon electron interaction. That onset was found to vary over a considerable range of frequencies (figure 5.29). Some devices showed, as already mentioned in above paragraph, no high frequency plateau in the measured frequency range, and it is seen that those have a degraded Tc. Apart from this, no correlation to other measurements values in this work is observed. With CeO_2 buffer layer on sapphire Rönnung et al. obtained the onset at

---

[9] The two temperature equation ,equation (2.25), at low frequencies ($\omega << \tau_{pe}^{-1}$) is approximately equal the lorentzian equation ,equation (2.7).

[10] As mentioned in section 2.4 τ_{diff}^{-1} is equal to $25ns$ for a $1\mu m$ long bridge using the heat capacitance and conductivity of YBCO at Room temperature

2 GHz [48], while in [62] it was not observed in the studied range (maximal frequency of 10 GHz). Danerud et al. reports this starts at 3-4GHz for several different substrate materials [61].[11] It should be noted that in literature all measurements are performed at Tc (where detectors are usually operated), no room temperature results are discussed. Lastly, extension to higher frequencies is required to observe the roll-off of the plateau. For an onset of the high frequency shelf at 4 GHz, the two temperature model predicts that the roll-off will take place around 140 GHz. Additionally, extending the range will allow to determine whether it occurs on the devices where the plateau was not revealed. The setup would have to be completely redesigned to reach these high frequencies.

We observed a non-zero response for unbiased devices, the shape of the curves was significantly different from biased devices however. This result is still unexplained. A discontinuity of the slope is present at the frequency at which the setups are changed (setup between 20 Hz and 100 kHz using direct detection, compared to the setup from 100 kHz to 15 GHz using super heterodyne (mixing) detection). The origin of this experimental error needs to be further investigated.

Finally the variability in the RF curves (for frequencies between 100 kHz and 10 GHz) is clearly summarized in figure 5.31, by aligning all curves at 8 GHz (for visibility concerns). Investigation on the fabrication process to gain control on reproducibility is required. In this respect, parallel with electrical characterization, a microscopic study could be performed, using AFM and TEM techniques to analyze the quality of the interface (as well as the film and the substrate).

---

[11] The physical interaction occurs in the film and is a priori unrelated to the interface.

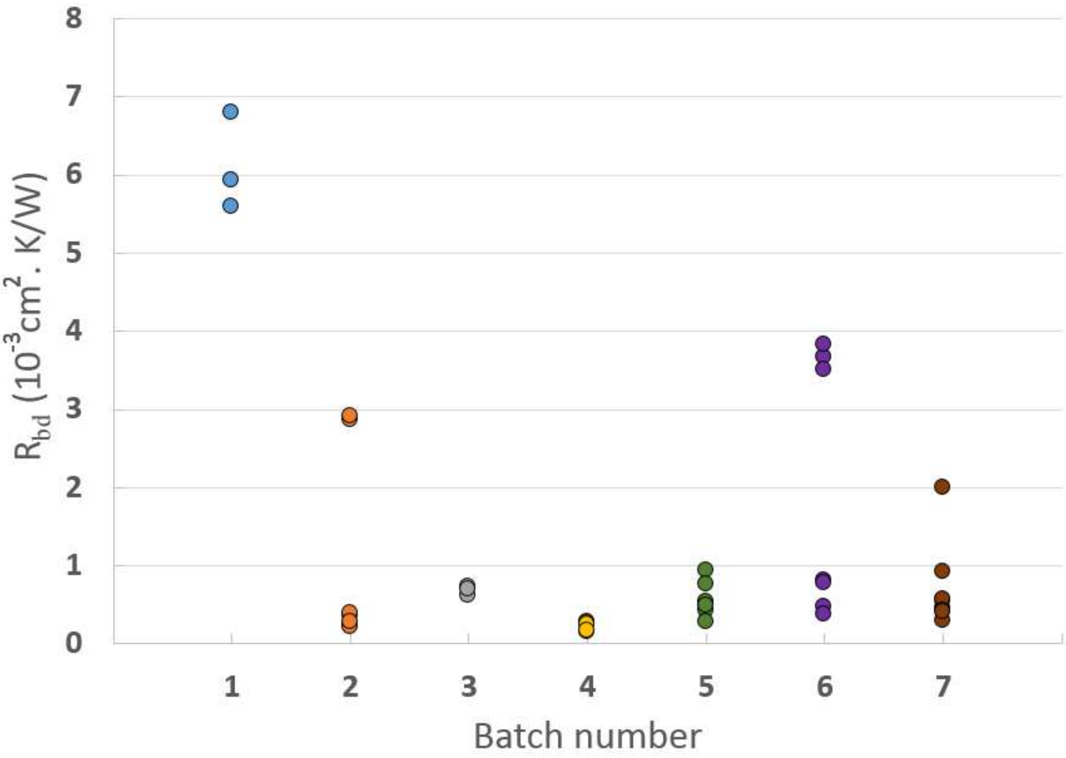

Figure 5.23: Thermal boundary resistance evaluated by the DC method for the different batches. A considerable scattering is present in each batch and between batches. Batch 4 is seen to have the lowest values and least scattering, between 0.1 and $0.3.10^{-3}cm^2K/W$. Temperature deposition was varied in the first 4 batches, buffer layer thickness in batch 5-7 with deposition temperature equal to the one in batch 4.

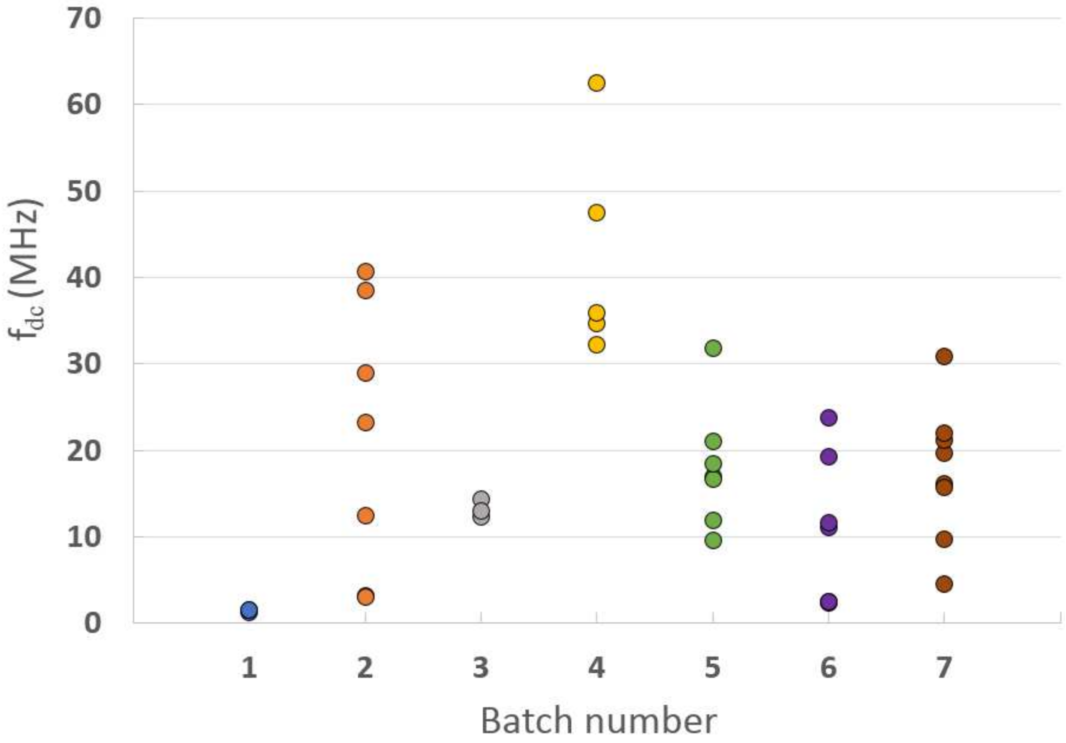

Figure 5.24: Calculated cut-off frequencies based on the DC measurements, using equation 2.4.

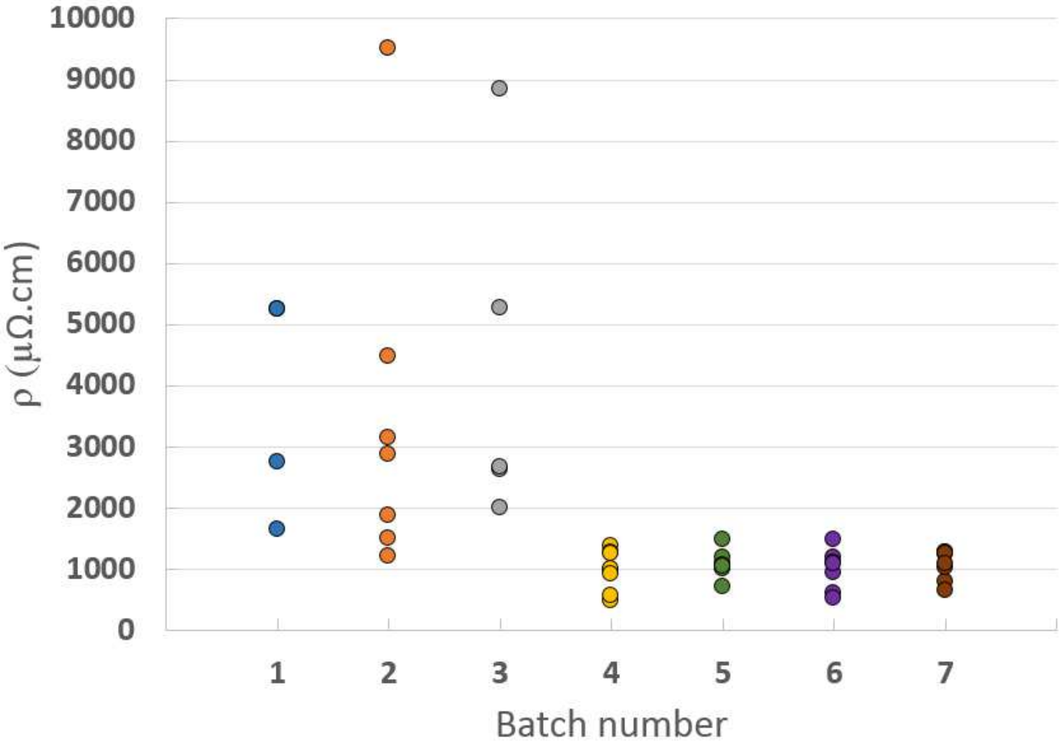

Figure 5.25: Resistivity scatter plot. This plot shows the devices having resistance below $10k\Omega$.

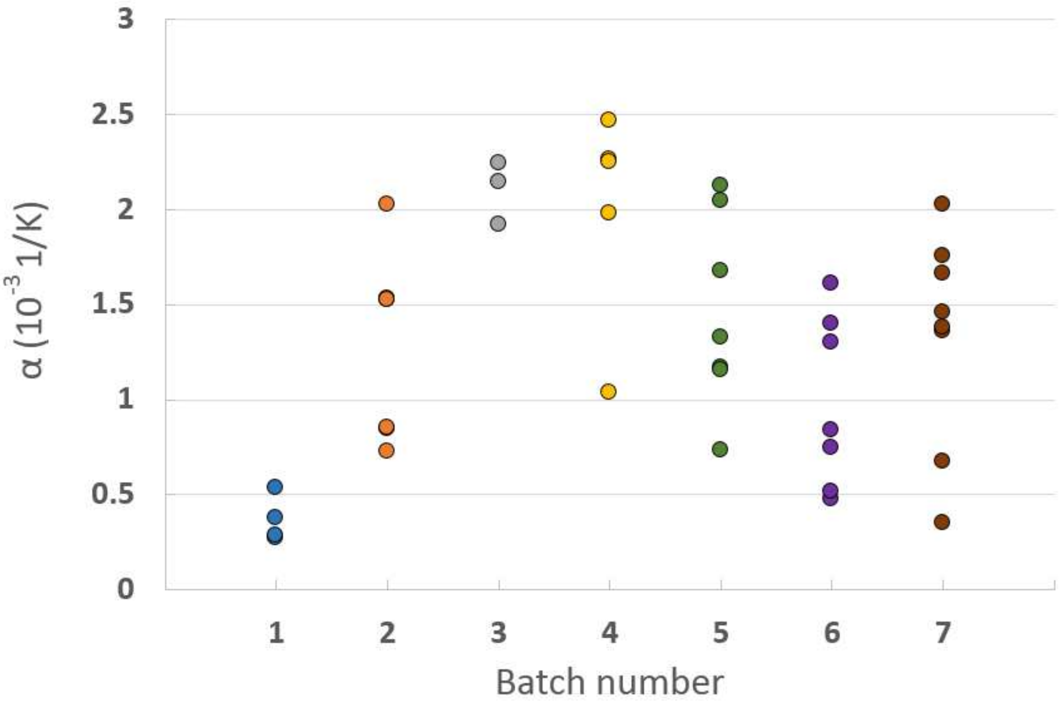

Figure 5.26: Temperature coefficient of resistance scatter plot.

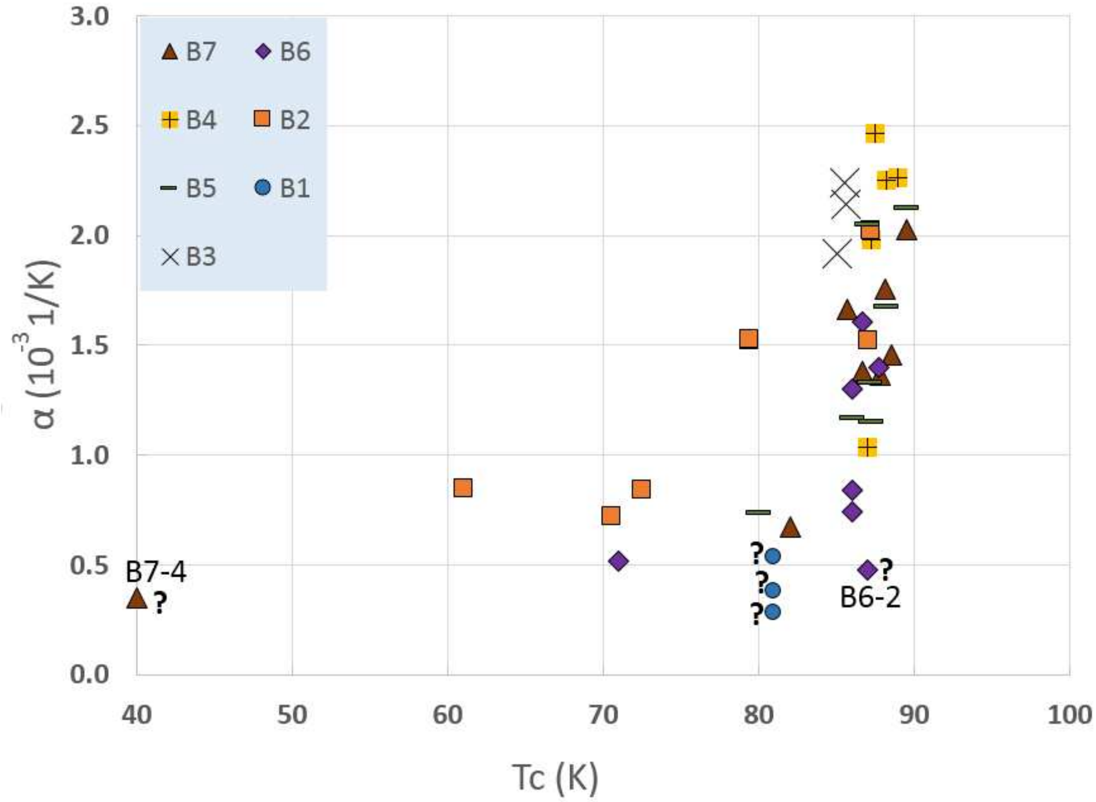

Figure 5.27: Temperature coefficient of resistance versus transition temperature to superconductive state. The highest TCR's are obtained in the case that the Tc of the film is high ,if the Tc is below 80K then the TCR is low as well, but a general correlation is not present. The question-marks beside the symbols for some of the devices mean the drop to zero resistivity was not observed.

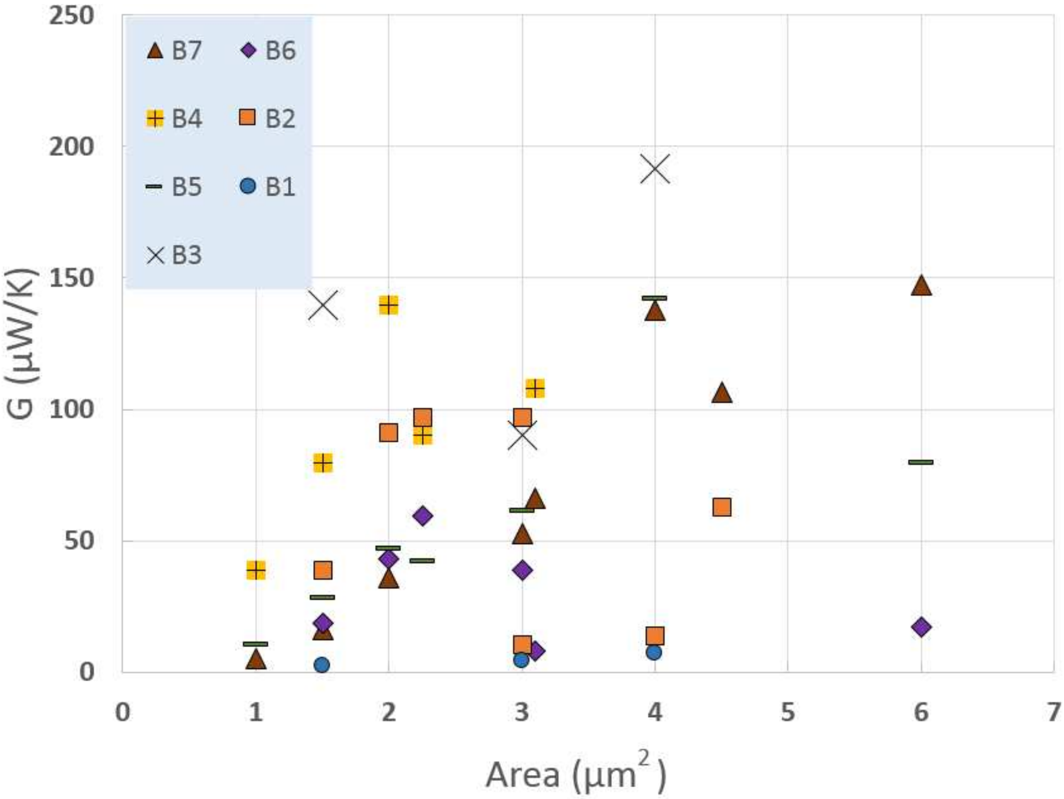

Figure 5.28: Thermal conductance as a function of the area. According to equation (2.13) the thermal conductance should scale linearly to the area, the slope being inversely proportional to the thermal boundary resistance, R_{bd}. This is verified for batches 1,4,5 and 7. This includes batch 6 if the 3 devices with area larger than $3\mu m^2$ are neglected. 5,6 and 7 have the same R_{bd}. Batch 4 has the lowest thermal boundary resistance whereas, batch 1 has the highest. Batch 2 and 3 are very scattered.

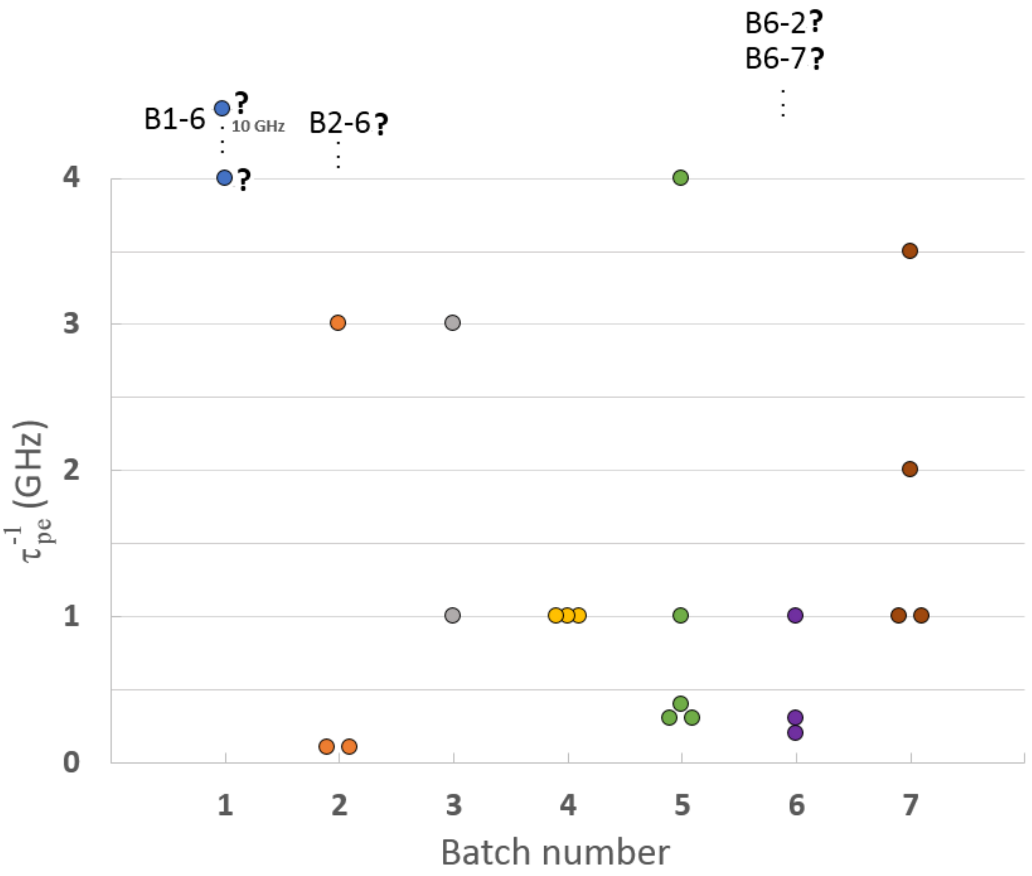

Figure 5.29: The onset of the second plateau for the different batches. Using the two temperature model this frequency is related to the phonon electron interaction time. The normalization with a factor 2π was omitted. The question marks indicate that the onset was either not clearly discernible or could still occur but falls outside the measurable frequency range (limited up to 10 GHz). Interestingly, those devices show a bad transition-curve to superconducting state (very low Tc in the case of B6-7, or a drop in resistance without going to zero resistivity, see the RT curves: figures 5.2, 5.4, 5.15).

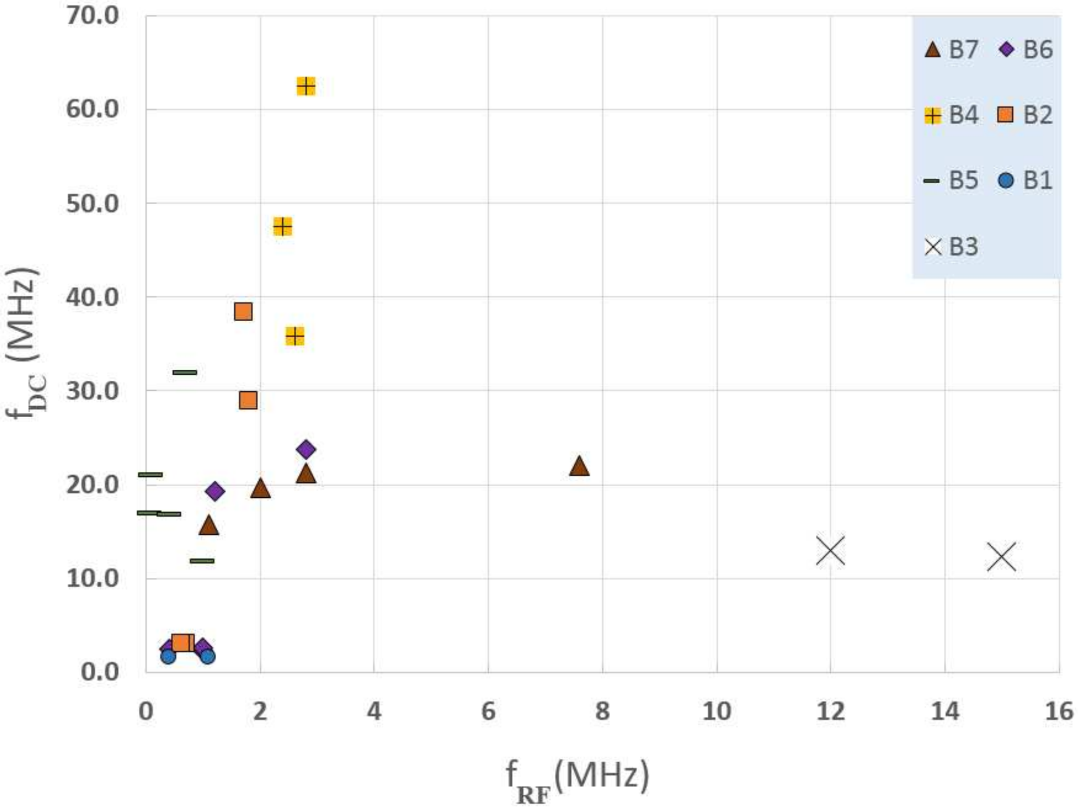

Figure 5.30: Frequency cut-off estimated by the DC-measurements f_{DC} and the frequency cut-off obtained from the lorentzian fit f_{RF} are incompatible (with the exception of batch 3). The f_{RF} cutoff lies for most devices below 3 MHz. The incompatibility remains unexplainable.

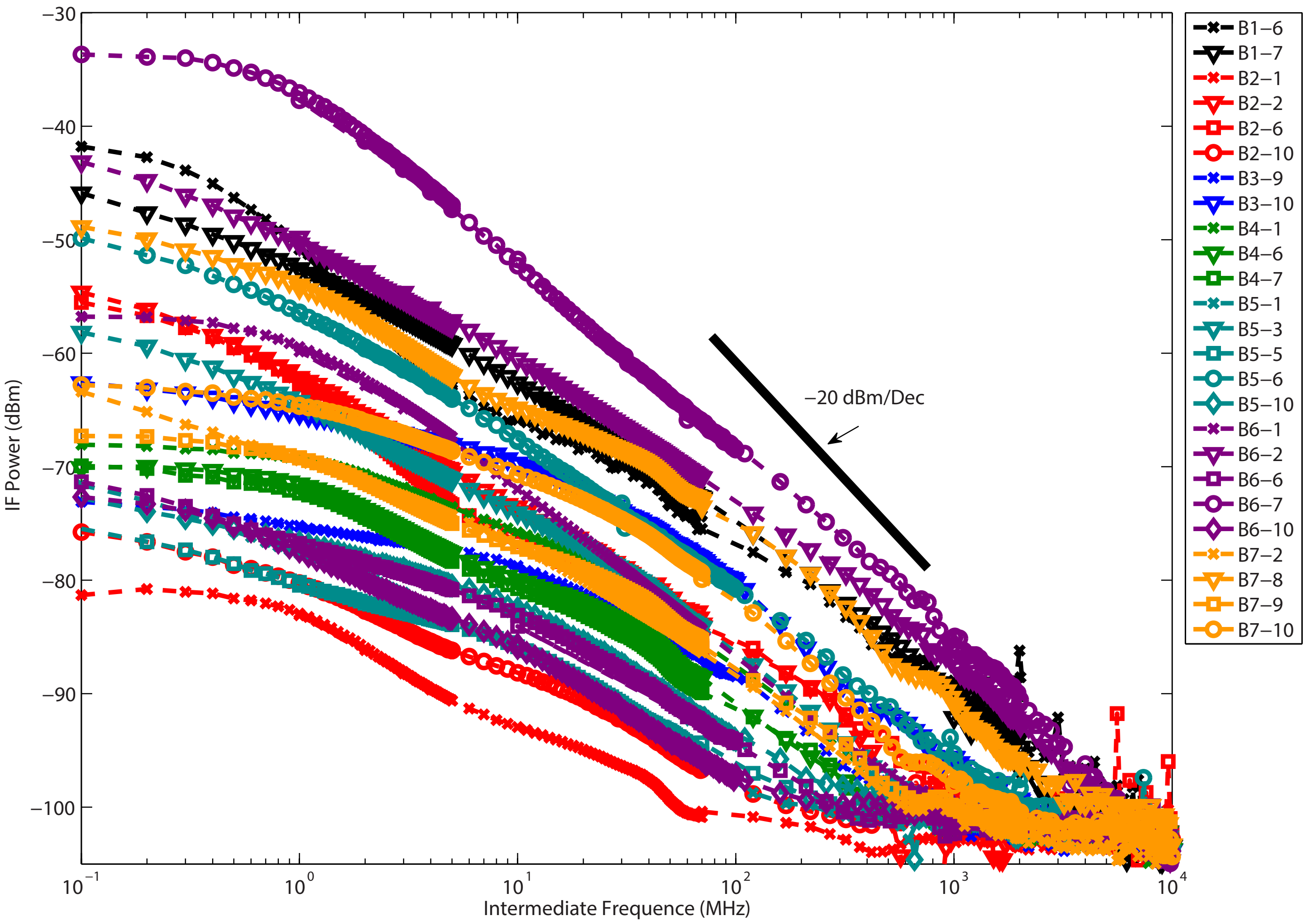

Figure 5.31: IF power versus IF frequency. The RF-curves are not at all similar among the batches and even inside each batch (exception to this is batch number 4).

6

Conclusions

The YBCO room temperature bolometers were designed, fabricated and characterized. It was observed that the thermal boundary resistance remains unaffected by the buffer layer thickness and the temperature deposition. Variability in the thermal boundary resistance was however present and needed to be controlled, $R_{bd} = 0.1 cm^2K/W - 1.0.10^{-3} cm^2K/W$ (excluding outliers). Significant variations were observed in important electrical parameters e.g. resistivity and thermal coefficient of resistance.

The RF measurements (IF power vs. intermediate frequency) showed variability over the whole frequency range. Further, from the complex frequency behavior, it was deduced that, excluding the thermal resistance at the interface, other thermal phenomena should be present. The two temperature model could explain the behavior at very high frequencies. According to the model, the variations are related to heat exchange between electrons and phonons in the film, but was seen to vary as well, and in some cases not observed (inside the measured frequency range). Although the effect of the thermal boundary resistance is considered by the two temperature model, the model was unable to predict the response curves at low and moderate frequencies. In this range substrate diffusion was believed to play a role. However the simulation results showed this effect to be negligible. In order to explain the results additional research on the thermal transport phenomena involved seems to be required.

Lastly, the thermal time constants calculated from the dc measurements are overall an order of magnitude higher than the actual ones obtained from low frequency roll-offs from the RF measurements. This inconsistency remains currently unexplained but we suspect it to be related to unaccounted thermal behavior.

Based on our literature studies and the results obtained during the current work, there seems to be strong evidences showing that the thermal boundary resistance can not be altered by any considerable amount in order to achieve a significant improvement in current responsivity or speed in this type of bolometers.

Bibliography

[1] A. Rostami, H. Rasooli, and H. Baghban, *Terahertz Technology: Fundamentals and Applications.* Berlin Heidelberg, Germany: Springer-Verlag, 2011.

[2] K. B. Cooper, R. J. Dengler, N. Lombart, T. Bryllert, G. Chattopadhyay, E. Schlecht, J. Gill, C. Lee, A. Skalare, I. Mehdi, and P. H. Siegel, "Penetrating 3-d imaging at 4- and 25-m range using a submillimeter-wave radar," *IEEE transaction on microwave theory and techniques*, 2008.

[3] A. Arbor. Hidden art could be revealed by new terahertz device. [Online]. Available: $http://newswise.com/articles/view/537448/$

[4] D. T. Leisawitz, W. C. Danchi, M. J. DiPirro, L. D. Feinberg, D. Y. Gezari, M. Hagopian, W. D. Langer, J. C. Mather, S. H. Moseley, M. Shao, R. F. Silverberg, J. G. Staguhn, M. R. Swain, H. W. Yorke, and X. Zhang, "Scientific motivation and technology requirements for the spirit and specs far-infrared/submillimeter space interferometers," *SPIE Proceedings*, pp. 36–46, 2000.

[5] Swedish-Space-Corporation. Steamr, the stratosphere-troposphere exchange and climate monitor radiometer. [Online]. Available: $http://www.iapmw.unibe.ch/research/projects/STEAMR/$

[6] J. Federici and L. Moeller, "Review of terahertz and subterahertz wireless communications," *Journal of Applied Physics*, 2010.

[7] K. Ishigaki, M. Shiraishi, S. Suzuki, M. Asada, N. Nishiyama, and S. Arai, "Direct intensity modulation and wireless data transmission characteristics of terahertz-oscillating resonant tunnelling diodes," *Electronics Letters*, 2012.

[8] T. Kürner and S. Priebe, "Towards terahertz communications - status in research standardization and regulation," *Journal on Infrared and Millimeter Terahertz Waves*, 2013.

[9] T. Schneider, A. Wiatrek, S. Preussler, M. Grigat, and R.-P. Braun, “Link budget analysis for terahertz fixed wireless links,” *IEEE transaction on terahertz science and technology*, 2012.

[10] S. P. Langley, “The bolometer and radiant energy,” *Proceedings of the American Academy of Arts and Sciences*, pp. 42–358, 1881.

[11] NASA. Steamr, the stratosphere-troposphere exchange and climate monitor radiometer. [Online]. Available: $http://earthobservatory.nasa.gov/Features/Langley/langley_2.php$

[12] S. Bevilacqua, *Superconduction THz mixers based on MgB2 film.* Göteborg, Sweden: Chalmers University of Technology, 2013.

[13] H. Ekström, *Antenna Integrated Superconducting Mixers.* Göteborg, Sweden: Chalmers University of Technology, 1995.

[14] P. L. Richards, “Bolometers for infrared and millimeter waves,” *Applied Physics*, 1994.

[15] S. Verghese and P. Richards, “Fabrication of an infrared bolometer with a high tc superconducting thermometer,” *IEEE Transactions on magnetics*, p. 3077, 1991.

[16] M. Kroug, *NbN hot bolometer mixers for a quasi-optical THz Receiver*, Göteborg, Sweden, 2003.

[17] B. Karasik, W. McGrath, and M. Gaidis, “Analysis of a high-tc hot-electron superconducting mixer for terahertz applications,” *Journal of Applied Physics*, 1996.

[18] S. Cherednichenko, A. Hammar, S. Bevilacqua, V. Drakinskiy, J. Stake, and A. Kalabukhov, “A room temperature bolometer for terahertz coherent and incoherent detection,” *IEEE Transactions on Terahertz Tcience and Technology*, pp. 395–402, 2011.

[19] A. Scheuring, P. Thoma, J. Day, K. Il’in, J. Hanish, B. Holzapfel, and M. Siegel, “Thin prbacuo film antenna coupled thz bolometers for room temperature operation,” *IEEE transactions on Terathertz science and technology*, 2013.

[20] A. D. Semenov, H. Richter, H.-Z. Hubers, B. Gunther, A. Smirnov, K. S. Ilin, M. Siegel, and J. P. Karamarkovic, “Teraherzt performance of integrated lens antennas with a hot-electron bolometer,” 2007.

[21] M.Ikebe, H. Fujishiro, T. Naito, M. Matsukawa, and K. Noto, “Anisotropic thermal diffusivity and conductivity of ybco(123) and ybco(211) mixed crystals,” *Japanese of Journal of Applied Physics*, p. 6157, 1994.

[22] J. Loram, K. Mirza, J. Wade, J. Cooper, and W. Liang, “The electronic specific heat of ybco from 1.8 to 300k,” *Physical Review letters*, 1993.

[23] S. Hagen, Z. Wang, and N. Ong, "Anisotropy of the thermal conductivity of ybco," *Physical Review B*, 1989.

[24] J. Blakemore, *Solid State Physics (2nd ed).* Cambridge University Press, 1985.

[25] N. Kaareh, *Handbook of High Temperature superconductor electronics.* CRC Press, 2003.

[26] R. Shaviv, E. F. Westrum, R. J. C. Brown, M. Sayer, X. Yu, and R. D. Weir, "The heat capacity and derived thermophysical properties of the high tc superconductor yba2cu3o7 from 5.3 to 350 k," *Journal of Chemical Physics*, 1990.

[27] P.Langlois, D.Robbes, M. L. C. Sing, C. Gunther, D. Bloyet, J. Hamet, R. Desfeux, and H.Murray, "Superconducting fast microbolometers operating below their critical temperature," *Journal of applied physics*, 1994.

[28] N. Perrin and C. Vanneste, "Response of superconducting films to a periodic optical irradiation," *Physical review*, 1983.

[29] A. Adam, *Low and High Tc bolometer detectors for THz frequencies.* Göteborg, Sweden: Chalmers University of Technology, 2002.

[30] A. V. Sergeev, A. D. Semenov, P. Kouminov, V. Trifonov, I. G. Goghidze, B. S. Karasik, G. N. Goltsman, and E. M. Gershenzon, "Transparency of a yba2cu3o7-film/substrate interface for thermal phonons measured by means of voltage response to radiation," *Physical Review B*, 1994.

[31] Q. Hu and P. Richards, "Design and analysis of a high tc superconducting bolometer," *Applied Physics Letter*, p. 2444, 1989.

[32] F. Rönnung, *Heterodyne mixers based on YBCO thin films.* Göteborg, Sweden: Chalmers University of Technology, 2003.

[33] D. Rutledge, D. Neikirk, and D. Kasilingham, *Infrared and Millimeter Waves*, K. Button, Ed., New York, 1983.

[34] S. Preu, G. H. Döhler, S. Malzer, L. J. Wang, and A. C. Gossard, "Tunable, continuous-wave terahertz photomixer sources and application," *Journal Applied Physics*, 2011.

[35] A. K. Harman, S. Ninomiya, and S. Adachi, "Optical constants of sapphire al2o3 single crystals," 1994.

[36] D. Filipovic, S. Gearhart, and G. Rebeiz, "Double-slot antennas on extended hemispherical and elliptical silicon dielectric lenses," *IEEE transactions on microwave theory and techniques*, 1993.

[37] J. W.Lamb, “Miscellaneous data on materials for millimetre and submillimeter optics,” *IEEE Transactions on Microwave Theory and Techniques*, pp. 1729–1747, 1996.

[38] A. Gatesman, J. Waldman, M. Ji, C. Musante, and S. Yngvesson, “Miscellaneous data on materials for millimetre and submillimeter optics,” *11th Int. Sym. on Space Terahertz Technology*, 2000.

[39] A. Hammar, S. Cherednichenko, S., S.Bevilacqua, V.Drakinskiy, and J. Stake, “Terahertz direct detection in ybco microbolometers,” *IEEE transaction on terahertz science and technology*, 2011.

[40] D. Neikirk, W. W. Lam, and D. B. Rutledge, “Far-infrared microbolometer detectors,” *International Journal of Infrared and Millimeter Waves*, pp. 245–277, 1984.

[41] V. S. Jagtap, A. Scheuring, M. Longhin, A. J. Kreisler, and A. F. Degardin, “From superconducting to semiconducting ybco thin film bolometers: Sensitivity and crosstalk investigations for future thz imagers,” *IEEE transactions on applied superconductivity*, pp. 287–292, 2009.

[42] N. Chianh, H. Shin, K. Kim, Y. Han, and S. Moon, “Characterization of uncooled bolometer with vanadium tungsten oxide infrared active layer,” *Sensors and Actuators Physical A*, 2005.

[43] M. J. Burns, A. Kleinsasser, K. Delin, R. Vasquez, B. Karasik, W. McGrath, and M. Gaidis, “Fabrication of high tc hot-electron bolometric mixers for thz applications,” *IEEE transactions on applied superconductivity*, p. 3564, 1997.

[44] E. Machlin, *Materials Science in Microelectronics I*, 2nd ed. Elsevier Science, 2005.

[45] N. Masilamani, O. V. Shcherbakova, S. A. Fedoseev, A. V. Pan, and S. X. Dou, “Effect of substrate and buffer layer materials on properties of thin ybco films,” 2013.

[46] M. W. Denhoff and J. P. McCaffrey, “Epitaxial ybco thin films on ceo2 buffer layers on sapphire substrates,” *Journal of Applied Physics*, 1991.

[47] F. Wang and R. Wördenweber, “Large-area epitaxial ceo2 buffer layers on sapphire substrates for the growth of high quality ybco films,” *Thin Solid Films*, 1993.

[48] F. Ronnung, M. Danerud, M. Lindgren, and D. Winkler, “Epitaxial ybaco thin films on ce02 buffered sapphire for optical mixers,” 1997.

[49] D. C. Alsop, C. Inman, A. E. Lange, and T. Wilbanks, “Design and construction of highsensitivity infrared bolometers for operation at 300 mk,” *Applied Optics*, p. 6610–6615, 1992.

[50] Gentec, EO, and USA. Pyroelectric detectors. [Online]. Available: $http://www.gentec-eo.com$

[51] Microtech and I. inc. Golay cell detectors. [Online]. Available: $http://www.mtinstruments.com/$

[52] H. Itoa, F. Nakajima, T. Ohno, T. Furuta, T. Nagatsuma, and T. Ishibashi, "Inp-based planar antenna integrated schottky barrier diode for millimeter and submillimeterwave detection," *Japanese Journal of Applied Physics*, pp. 6256–6261, 2008.

[53] S. Bevilacqua and S. Cherednichenko, "Low noise nanometer scale room temperature ybco bolometers for thz direct detection," *IEEE Transactions on Terahertz Science and technology*, 2014.

[54] S. Nawaz, *Approaching the depairing critical current in superconducting YBCO nanowires.* Göteborg, Sweden: Chalmers University of Technology, 2013.

[55] M. Lindgren, V. Trifonov, M. Zorin, M. Danerud, D. Winkler, B. Karasik, G. Goltsman, and E. Gershenzon, "Transient resistive photoresponse of ybco films using low power 0.8 and 10.6 micrometer laser radiation," *Applied Physics Letter*, 1994.

[56] T.-L. Hwang, S. E. Schwarz, and D. B. Rutledge, "Microbolometers for infrared detection," *Applied Physics Letters*, 1979.

[57] M. Nahum, S. Verghese, and L. C. P.L. Richards, "Thermal boundary resistance for ybco films," *Applied Physics Letters*, 1991.

[58] C. D. Marshall, A. Tokmakoff, I. M. Fishman, C. B. Eom, J. M. Phillips, and M. D. Fayer, "Thermal boundary resistance and diffusivity measurements on thin yba2cu307 films with mgo and srti03 substrates using the transient grating method," *IEEE transaction on microwave theory and techniques*, pp. 850 – 857, 1993.

[59] C. G. Levey, S. Etemad, and A. Inam, "Optically detected transient thermal response of high tc epitaxial films," *Applied Physics Letters*, 1991.

[60] P. Toma, *Ultra-fast YBaCuO direct detectors for the THz frequency range.* Karlsruhe, Germany: Karlsruher Institut fur Technologie, 2013.

[61] M. Danerud, D. Winkler, M. Lindgren, M. Zorin, V. Trifonov, B. S. Karasik, G. N. Goltsman, and E. M. Gershenzon, "Nonequilibrium and bolometric photoresponse in patterned ybco thin films," *Journal of Applied Physics*, pp. 1902–1909, 1994.

[62] O. Harnack, B. Karasik, W. McGrath, A. Kleinsasser, and J. Barner, "Microwave mixing and if bandwidth in sub-micron long high -to hot- electronbololometers," *Tenth International Symposium on Space Terahertz Technology, Charlottesville*, pp. 169–179, 1999.

A

Appendix 1: derivation of bolometetric mixing with AM modulation on the RF source

$$\begin{multline} P = 1/R\Bigg(0.5\Big(E_{RF}(1+M\cos(\omega_{AM}t+\phi)\Big)^2 + 0.5E_{LO}^2 \\ + 0.5\Big(E_{RF}(1+M\cos(\omega_{AM}t+\phi)\Big)^2\cos(2*\omega_{RF}t)+ \\ 0.5E_{LO}^2\cos(2*\omega_{LO}t) + E_{LO}E_{RF}(1+M\cos(\omega_{AM}t+\phi)\cos((\omega_{RF}+\omega_{LO})t) \\ + E_{LO}E_{RF}(1+M\cos(\omega_{AM}t+\phi))\cos((\omega_{RF}-\omega_{LO})t)\Bigg) \tag{A.1} \end{multline}$$

Only the terms at frequency $\omega_{RF}-\omega_{LO}$ and ω_{AM} give rise to thermal oscillations, the others just contributing to a thermal offset, summarized as:

$$\begin{multline} P_{dissipated} = P_{LO} + P_{RF}\Big(1+M\cos(\omega_{AM}t+\phi)\Big)^2 + \\ 2\sqrt{P_{LO}P_{RF}}\cos(\omega_{IF}t)(1+M\cos(\omega_{AM}t+\phi) \tag{A.2} \end{multline}$$

This can be further simplified, leading to the final expression:

$$\begin{multline} P_{dissipated} = P_{LO} + P_{RF} + \mathbf{P_{RF}M}\cos(\omega_{\mathbf{AM}}\mathbf{t}+\phi) + M^2\cos(2*(\omega_{AM}t+\phi)) \\ + 2\sqrt{P_{LO}P_{RF}}\cos(\omega_{IF}t) \\ + 1\sqrt{P_{LO}P_{RF}}\cos(\omega_{IF}+\omega_{AM}t+\phi)) + 1\sqrt{P_{LO}P_{RF}}\cos(\omega_{IF}-\omega_{AM}t-\phi)) \tag{A.3} \end{multline}$$